# Important Notice

This copy may be used only for the purposes of research and private study, and any use of the copy for a purpose other than research or private study may require the authorization of the copyright owner of the work in question.  Responsibility regarding questions of copyright that may arise in the use of this copy is assumed by the recipient.

UNIVERSITY OF CALGARY

Seismic Depth Imaging in Anisotropic Media

East Coast of Canada Case Study

by

Li Lu

A THESIS

SUBMITTED TO THE FACULTY OF GRADUATE STUDIES

IN PARTIAL FULFILLMENT OF THE REQUIREMENTS FOR THE

DEGREE OF MASTER OF SCIENCE

DEPARTMENT OF GEOSCIENCE

CALGARY, ALBERTA

MARCH, 2014

# UNIVERSITY OF CALGARY

# FACULTY OF GRADUATE STUDIES

The undersigned certify that they have read, and recommend to the Faculty of Graduate Studies for acceptance, a thesis entitled "Seismic Depth Imaging in Anisotropic Media" submitted by Li Lu in partial fulfillment of the requirements for the degree of MASTER OF SCIENCE.

_____

Supervisor, Dr. Gary F. Margrave
Department of Geoscience

_____

Dr. Donald C. Lawton
Department of Geoscience

_____

Dr. Kristopher A. H. Innanen
Department of Geoscience

_____

External Examiner, Dr. Ian D. Gates
Department of Chemical and Petroleum Engineering

_____

Date

# Abstract

Our ultimate goal of seismic data processing is to produce seismic images with correct lateral and vertical positions, and with amplitude proportional to the reflection coefficients in the subsurface. A good migrated image depends strongly on the accuracy of the velocity model.

Prestack depth migration (PSDM) is a powerful tool not only for imaging but also for velocity model building. The main techniques used for migration velocity analysis include vertical updating and tomography analysis , including anisotropy parameters estimation.

To achieve the goal of accurately positioning the seismic events in subsurface, the velocity anisotropy should be accounted for. If the presence of velocity anisotropy is important, then ignoring it will significantly degrade the final image accuracy.

This thesis examines a frontier exploration survey acquired off the East Coast of Canada by Statoil Canada Ltd. and processed by CGG. Kirchhoff isotropic PSDM and tilted transverse isotropy (TTI) PSDM were conducted with the goals of good imaging and good velocity estimation. Structural interpretation and Amplitude Versus Offset (AVO) analysis for this survey demonstrate the benefits of TTI PSDM, whose subsurface images significantly reduced the exploration risk compared with isotropic PSDM.

Estimation of reliable anisotropy parameters is challenging, especially for the survey studied in this thesis where no well information is available. This thesis presents a practical production method for building five parameter fields needed for TTI PSDM: p-wave velocity, Thomsen's anisotropy parameters and the angles describing the symmetry axis of the anisotropy. This method includes 1D joint inversion (Huang, 2007) to estimate anisotropy parameter and high resolution tomography (Hu, 2011) to obtain accurate velocity models.

# Acknowledgments

I am very grateful to have Gary Margrave to be my supervisor. During this journey toward my MSc. degree, Gary's attention to scientific details (geophysics, math, etc.) greatly influenced me. Without his guidance and support, this thesis would not have been possible.

I own an immense thanks to Sam Gray. He is the first reader of my thesis, gave me a lot of advice and correct my English wordings.

I would like to extend my gratitude to Statoil and Repsol for granting me the data show rights.

I would like to thank CGG for the permission to use their computer system for my research. Thanks to my boss, JJ Wu for his support and help on my work.

Another great acknowledgment goes to my colleague, Wentao, Sun. His support on my latex usage makes my thesis writing much easier.

I would also like to thank my friends and colleagues who gave me help and encouragement which enable me to start, move forward and complete this hard but very rewarding journey. It is difficult to name all the them, but what they did is unforgettable.

Finally, I would like to thank my husband, Xianjin, my sons, Richard and Collin. I have been blessed with a loving family. As a student, a full time professional and a mom, this work would not have been possible without their support, I am indebted to their continuous support and their sacrifice of time and love.

# Dedication

To my parents.

# Table of Contents

# List of Tables

# List of Figures

# List of Symbols

$\delta$ — Thomsen anisotropy parameter

$\omega$ — Angular frequency

$\phi$ — the azimuthal angle of symmetry axis

$\phi_{ray}$ — Group angle

$\psi$ — Pressure wavefield

$\rho$ — Density

$\theta$ — the dipping angle of symmetry axis

$\theta_{wavefront}$ — Phase angle

$\varepsilon$ — Thomsen anisotropy parameter

$\boldsymbol{C}$ — Stiffness tensor

$\boldsymbol{\varepsilon}$ — strain tensor

$\boldsymbol{\sigma}$ — Stress tensor

$k_x, k_z$ — Horizontal and vertical wavenumber

$p$ — Ray parameter

$V_p$ — P-wave phase velocity

AGC — Automatic gain control

AVO — Amplitude versus offset

CIGs — Common image gathers

CMP — Common midpoint

FWI — Full waveform inversion

NMO — Normal-move-out

PBR — Primary-to-bubble ratio

PSDM — Prestack depth migration

RMS — Root-mean-square

RTM — Reverse time migration

SRME    Surface-related multiple elimination

TTI     Transverse isotropy with a tilted axis of symmetry

VTI     Transverse isotropy with a vertical axis of symmetry

# Chapter 1

# Introduction

Seismic methods are among the geophysical methods to find hydrocarbons in the subsurface of the Earth. A great deal of literature exists on the seismic method (Sheriff and Geldart, 1995; Yilmaz, 2002). Figure 1.1 describes the basic schematic method of seismology in a marine environment.
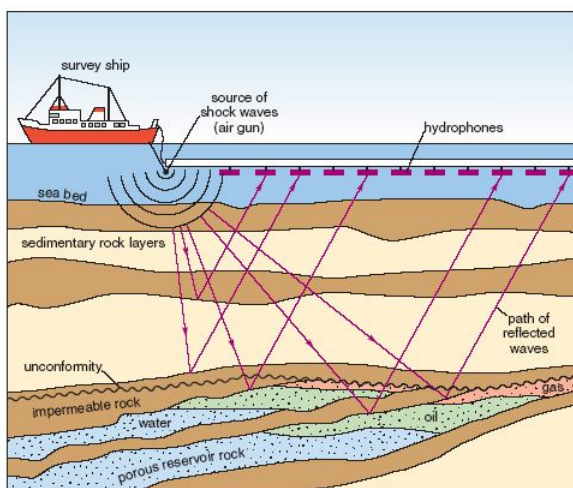


Figure 1.1: Marine seismic acquisition. The basic application of seismic data acquisition in a marine setting (The Open University website).

The air gun source generates a pressure wavefield which passes through the water and penetrates the sea bed. Seismic waves propagate through the subsurface and are reflected back at boundaries between sediment/rock layers where there is an impedance contrast. Reflected energy is detected and recorded by hydrophones which are towed at some streamer depth. Returning signals from each shot are displayed against time with time zero being the shot initiation time. Successive shots (Figure 1.2) are displayed, building up a profile as the survey vessel moves through the water.
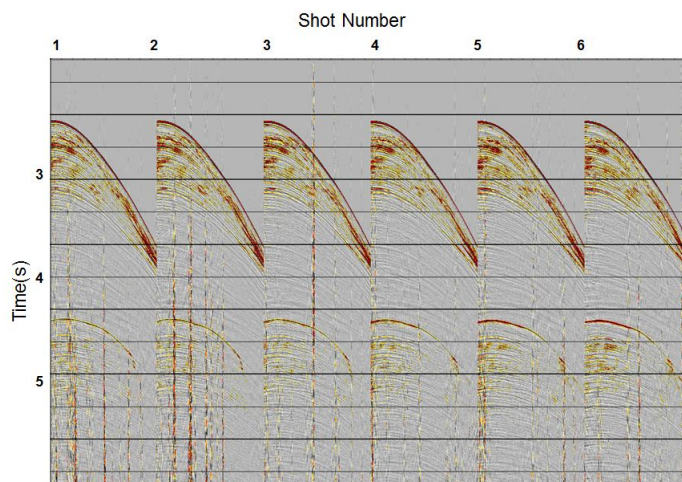
Figure 1.2: Raw shots acquired in the field

As shown in Figure 1.2, the recorded seismic shots can not be used directly for interpretation. In Figure 1.2, black color means an increase in acoustic pressure at the geophones while red means a decrease. Comparing Figure 1.2 with Figure 1.3, we can see a clear contrast between these two sections. The raw shots shown in Figure 1.2 are full of noise and multiples and they give few clues about the subsurface structures. In contrast, the final images shown in Figure 1.3 give us the clear clue how the subsurface structure looks like, which include the water bottom with the varying depth from 2.8s to 3.2s, unconformity at 4s and nice dipping faults. Here the amplitudes do represent the reflectivity. It takes a great many shot records in Figure 1.2 to produce the final images in Figure 1.3. Different types of processing need to be performed on the raw seismic shots in order to produce the final images for further interpretation to detect potential hydrocarbons.

Seismic data processing seeks to relate the pressure variations recorded by the hydrophones to geologic properties of the subsurface, primarily reflection coefficients. To achieve this, a number of procedures need to be performed in the processing, such as, spherical spreading correction (Yilmaz, 2002), a time dependent amplitude scaling (Yil-
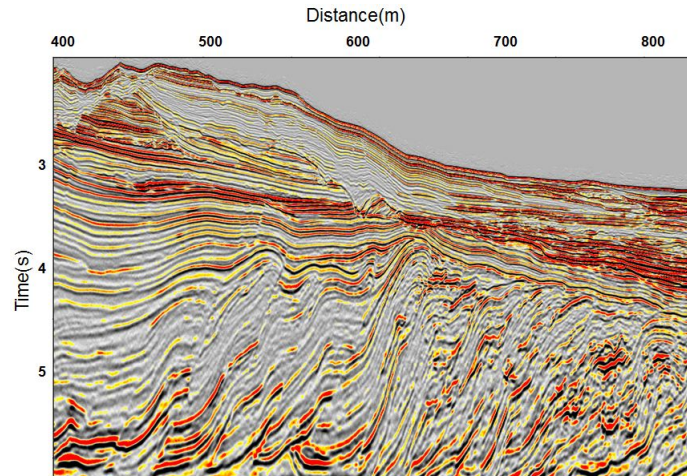
Figure 1.3: Final subsurface image shows the great feature of subsurface including the water bottom with the varying depth from 2.8s to 3.2s, unconformity at 4s and nice dipping fault. Here the amplitudes do represent the reflectivity.

maz, 2002), which approximately corrects for amplitude loss due to spherical divergence. Deterministic and statistical deconvolution (Yilmaz, 2002) are performed to recover a spike wavelet. Noise attenuation and multiple removal attenuate different kinds of noise and multiples. Furthermore, the original acquired data were gathered in source and receiver coordinates; these data will be sorted to different coordinates as different processes require different processing domains, such as CMP (common midpoint - the reflection point is midway between the source position and the receiving-phone position) or common offset (distance between source and receiver ) domains (Yilmaz, 2002). Last, migration will be performed to spatially re-position events and improve focusing. Migration also works as an inversion to recover the reflection coefficients in principle (Bleinstein et al., 1998); in practice this can be very difficult to achieve in structurally complex areas. Especially for depth migration, the construction of the velocity model is critical though difficult in achieving a successful migration result (Margrave, 2012).

While the major work presented in this thesis describes how to derive a good tilted

transversely anisotropic (TTI) velocity model to produce the best possible subsurface images of the Earth, a lot of preprocessing must be done to prepare input data for velocity model building and migration. In this introductory chapter, I will briefly describe the history of seismic imaging, how the data used in this thesis were acquired and preprocessed, and the major seismic migration method used in this thesis. Later, the main body of the thesis will concentrate on velocity model building, the term "velocity model building" in this thesis is used in a generalized sense to refer to the construction of a model of all anisotropic velocity parameters.

## 1.1  History of seismic imaging

In exploration seismology, seismic imaging is a process that uses man-made seismic waves to produce subsurface images of the Earth. The study of vibrations in the Earth, known as seismology, began with the study of naturally occurring earthquakes. Seismic waves produced by an earthquake contained valuable information about the large-scale structure of the Earth's interior. The earliest known instrument to detect the Earth quake was invented by ancient Chinese (Reddy, 2012). This instrument helped identify the direction and magnitude of an earthquake.

Nineteenth century researchers found that artificial seismic waves generated by high explosives resembled seismic waves generated by earthquakes. They built instruments to pick up the tremors, and to record and time them. The acquisition technique has evolved for more than a century, and man-made seismic waves have been utilized to help locate its mineral, water , and hydrocarbon resources by probing the very shallow structure of the Earth (Reddy, 2012).

After the sound wave's reflections from within the Earth are recorded by geophones on land or hydrophones in water, seismic data are processed by computers into images

that reveal subsurface geology and structure. Then oil-company scientists use the images to locate potential hydrocarbons traps. Among computer processes, the seismic imaging technique plays an important role in creating good quality images of the subsurface from field acquired seismic data.

Imaging is normally described as the process of producing a visual representation of an object, using different tools and techniques. The different types of geophysical imaging include 1) electrical resistivity tomography, 2) ground penetrating radar, 3) induced polarization and 4) seismic tomography and reflection seismology. Seismic imaging is one of the geophysical imaging techniques, using data from sound waves bounced off underground rock structures to reveal the possible tectonic structures.

From 1923 to 1935, the oil and gas industry began to appreciate the value of reflection from subsurface structure (Bednar, 2005). In the mid's 1930, numerous large oil companies were rapidly adopting the " new" reflection seismic method and doing everything possible to use it commercially. But many areas had very "poor" records. Rieber (1936) was one of the first to recognize the cause for this. Rieber published two papers that contain truncated bed models and faulted bed images. To obtain these images, he used slant stack (the procedure of applying linear moveout and summing amplitudes over the offset axis on a wavefield such as a common-shot gather) of field records ( the first to do so).

J. G. Hagedoorn's (Hagedoorn, 1954) explanation of "A process for seismic interpretation" became one of the fundamental papers on seismic imaging. In this paper, Hagedoorn introduces a "string" or " ruler and compass" method for finding reflections as an envelope of equal travel-time curves. This method clearly invokes the principle of Christan Huygens, and gave birth to the Kirchhoff "diffraction stack" method several years later (Bleistein and Gray, 2001). In recent years, the Kirchhoff method in all its various forms has proved to be one of the most flexible and robust approaches to seismic

imaging. This method will be further discussed in this thesis (Section 1.4.2).

From the beginning of the 1970s to end of the 1980s, different migration algorithms developed rapidly. Seismic migration could then be done in the space-time (x-t), frequency-space (f,x), wavenumber-space (k,x), or almost any combination of these domains. In 1970 and 1971, two papers by Jon Claerbout focused on the use of second order hyperbolic partial differential equations to perform the imaging. These papers presented an essential theory; upward and downward going waves governed by a one way wave equation are coupled together with an imaging condition that produces the image. In essence, one uses a computer to model the source waveform and to downward continue the recorded traces. At each depth or time step the two wavefields are cross-correlated to produce the image at that fixed step. The theory was then in place, and was widely applied, for many years. Claerbout's work exemplified how growing computer power can be used to implement theory. For the most part, his approach was numerically based on finite differences. The derivatives in the hyperbolic equation were replaced with numerical finite-difference approximations, and up-going and down-going waves were propagated sequentially.

The advent of 3-D seismic acquisition in the mid- to late 1980s helped to advance the development of computer workstations because the massive amount of the data collected in a 3-D survey needed ever greater computer power to supersede old paper-based techniques. The relentless progression toward, first larger, then smaller, but always more powerful computers made possible the routine implementation of pre-stack migration. In addition, the introduction of cluster computers provided a processing environment in which 3D pre-stack depth migration could be made to work both efficiently and cost effectively.

It is well known that sedimentary rocks possess velocity anisotropy to different degrees. Seismic data will demonstrate velocity anisotropy by showing increased magnitude non-hyperbolic move-out on far offsets, known as "hockey-sticks". If seismic data from

an area of anisotropy are processed using only isotropic velocity fields, images will be mispositioned in both depth and lateral location, leading to serious consequences for well placements (Byun, 1982; Uren et al., 1991; Isaac and Lawton, 1999; Vestrum et al., 1999; Lawton et al., 2001).The velocity model used to represent anisotropic subsurface media could be VTI (Vertical Transverse Isotropy), TTI (Tilted Transverse Isotropy), orthorhombic, triclinic anisotropy. Among them TTI velocity model building tools and migration techniques have gained industry acceptance during recent years.

Seismic acquisition technology and related imaging techniques are evolving each year. With the latest acquisition technology in marine environment, full azimuth, long offset and broadband data are acquired. The orthorhombic RTM (reverse time migration) has been put into production, which provides higher resolution and better illumination of subsurface structures. The long offset data make FWI (full waveform inversion) feasible to produce good velocity updates at least in the shallow section now.

## 1.2   How the data in this thesis were acquired

As illustrated in Figure 1.4, the data used in this thesis are from a narrow azimuth acquisition from the East Coast of Canada, using 2 sources and 10 cables. The record length is 9 seconds. The source and receiver depths are 8m and 10m respectively. The inline spacing is 25m and crossline spacing is 12.5m. The shooting direction is strike to the dominant geologic structure. The survey targets both structural and stratigraphic play.

The data used in this thesis are from a marine environment. Unlike land acquisition, which uses geophones to detect the velocity of displacement of the Earth, marine acquisitions usually use streamers (long cables towed behind source vessels) of hydrophones to record the pressure changes caused by compressional waves. Marine acquisition uses hy-

drophones because only a compressional wave can be transmitted through water. In the following paragraph, I discuss several aspects of which good understanding will benefit the seismic data processing: 1) survey design, 2) source signature, 3) source and receiver ghosts and 4) typical noise in a marine environment.
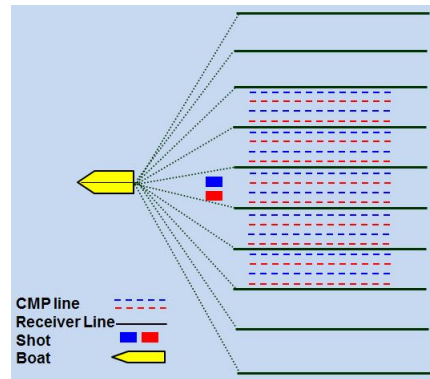


Figure 1.4: Marine acquisition top view. The ship in yellow towed 10 cables (black lines) and two sources in red and blue. The dotted lines represent the CMP lines generated in subsurface, they are half way between source and receiver line.

### 1.2.1 Survey design

3D survey design is the first step of 3D acquisition. Survey design has the ultimate goal of producing an interpretable image of the exploration target by carefully designing field acquisition parameters. At the same time, good survey design aims to minimize the acquisition and processing costs of the survey (Evans, 1997).

3D survey design begins with considering depth, areal extent and the largest dip among events that will contribute to the final image. The maximum dip is an important geophysical parameter for two reasons. First, the chosen spatial sampling parameter needs to be such that spatial aliasing is not a problem in imaging the steep-dip events. Second, the physical size of a survey needs to be big enough to capture the reflection energy, generated by steep dip events, in regions beyond the target edges. A major step

in 3-D survey design is in deciding the extent of surface coverage needed to obtain a desirable subsurface image. Two important issues are needed to consider in planning a survey to generate a seismic volume. First, there must be additional coverage at the edges of the 3D volume to ensure that target image has full-fold coverage across the area intended to be mapped. Second, there must be additional coverage because of the behavior of migration, which requires an extra length of migration aperture at both inline and crossline ends of the of survey.

To get clear subsurface images, both vertical and lateral resolution need to be considered. Higher vertical resolution requires higher temporal sampling of the data. Vertical resolution is determined by the frequency bandwidth of the recorded data. The greater the bandwidth and the higher the frequencies recorded, the greater the resolution of the final stacked profile and the greater the definition and imaging of geologic horizons. High lateral resolution demands small shot and receiver spacing (i.e., spatial sampling). To avoid spatial aliasing, an adequate spatial sampling is necessary for the dips and frequencies expected. Both receiver interval and streamer separation distance could be determined by the following formula: $\Delta x = \frac{v}{4f \sin(\theta)}$ , where $\Delta x$ is inline or crossline separation, v is surface velocity, f is frequency, and $\theta$ is emergence angle of reflection events (Evans, 1997). Processing bin sizes are generally determined by signal to noise ratio and common midpoint (CMP) spacing. Since the inline and crossline processing spacings are decided by knowledge of the dip, frequency, and velocity values, reflection signal-to-noise ratio and resolution (both horizontal and vertical ) become the most important factors in determining bin size. Each bin ideally should exceed a minimum fold (the number of traces in each CMP gather) amount, have a broad range of offsets and a broad range of azimuths. For marine surveys, signal to noise ratio and minimum fold coverage are not issues. Wide azimuth surveys are the usually most difficult to bin successfully, because the wide azimuth marine acquisition developed in recent years often provides poor or

nonuniform fold within each natural bin.

### 1.2.2   Marine energy sources

Marine acquisition uses air guns to generate a pressure wavefield. The shape in time of the pressure signal created by a marine source is called its signature. Figure 1.5 shows a generic signature for an explosive marine source. The initial positive peak is the explosive pulse; this is followed by a trough that is the reflection of the initial pulse from the sea surface (the "source ghost"). Following this is the bubble-generated noise train. The signature is characterized by two parameters: the primary pulse peak-to-peak (P-P) amplitude, or "strength"' the useful part of the signal, and its bubble period. Two important parameters of an air-gun array signature are its peak-to-peak (P-P) strength and primary- to-bubble ratio (PBR). The PBR should be as high as possible so that the air-gun array signature is close to an ideal pulse. The P-P strength (related to this nominal source level) is defined as the difference in absolute amplitude between the peaks of the primary and ghost arrivals. There are several reasons for deploying air-guns in arrays. The first is to increase the power of the source. The basic idea is that a source array of n single sources produces n times the power of the single source. The second is to minimize the PBR by tuning the array: Guns with different volumes will have different bubble periods, leading to a constructive summation of the first (primary) peak and destructive summation of the bubble amplitudes. Figure 1.6 shows the signature for individual air guns and the tuned signature when six air guns were fired simultaneously. In marine source array design, the main goal is to optimize the array's primary-to-bubble ratio.
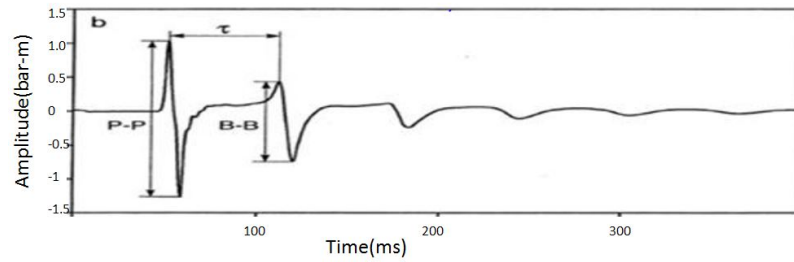
Figure 1.5: Far field source signature. P-P is peak to peak strength. B-B is bubble to bubble strength. $\tau$ is the bubble period.
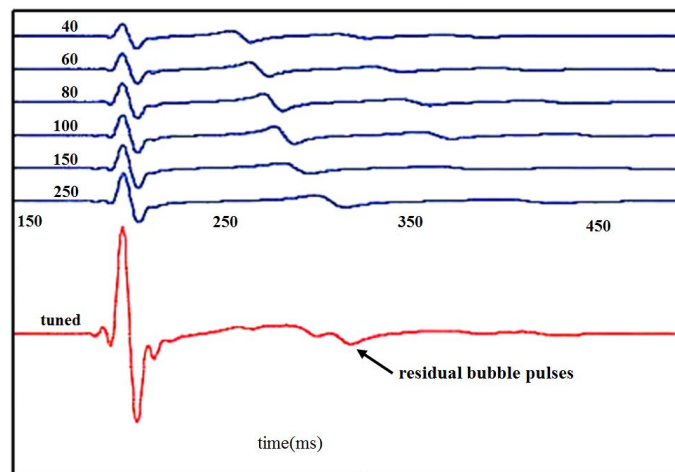


Figure 1.6: Air gun array

Far-field pressure signatures of individual air-guns vary with gun volume.

The tuned pressure signature is obtained when the six guns are fired simultaneously;

Guns with different volumes will have different bubble periods, leading to a

constructive summation of the first (primary) peak and destructive summation of the

bubble amplitudes.

### 1.2.3  Source and receiver ghost

Another important phenomenon in marine acquisition is source/receiver ghost effects. The source ghost was described briefly in the preceding section.

In marine acquisition, source and receiver are normally several meters below the sea surface. As illustrated in Figure 1.7, the wave emitted from source will be reflected from the sea surface, and this reflected wave will have a destructive effect with the primary source wave. The same thing happens on the receiver side. The resulting source and receiver ghosts will cause notches in the frequency spectrum of the recorded data, as follows.

The physics of sinusoidal wave propagation states that when two waves have the same wavelength, destructive interference (cancellation) occurs when they arrive exactly 180 out of phase. Because the reflection coefficient at the sea surface is negative, the down-going reflected wave experiences a 180 degree phase shift relative to the direct wave. However, the reflected wave experiences a further phase shift because of the additional distance, 2d, that it traveled relative to the direct wave. Destructive interference occurs when $2d = n\lambda$, where $n = 0, 1, 2, \cdots$. Since $\lambda = v/f$, the notch frequencies where destructive interference is experienced are given by $f = \frac{nv}{2d}, n = 0, 1, 2, \cdots$.

The calculation of notch frequency for receiver ghost is the same as source ghost.

Figure 1.8 shows idealized amplitude spectra, with notch frequency from source ghost clearly visible.

Novel ghost elimination ("deghost") (Wang, 2012) techniques have been developed recently. These have the effect of broadening the bandwidth at both low and high ends of the spectrum (Wang, 2012), and they can enhance the data texture, or appearance, due to the boosted low frequency. By broadening the bandwidth, they can also sharpen the wavelet. Finally, they can also improve the signal to noise ratio by removing much of the ghost field, which is truly noise.
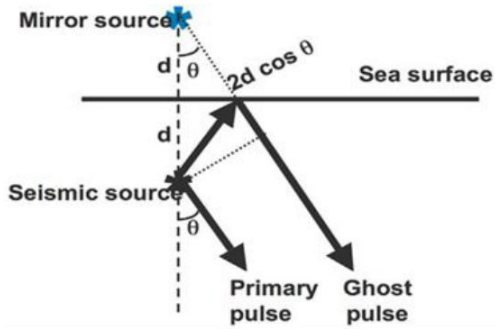
Figure 1.7: Source ghost generation scheme. The source is several meters below the sea surface. The wave emitted from the source is reflected back from the sea surface which has reflection coefficient close to -1, so this reflected wave will have a destructive effect with the primary source wave.
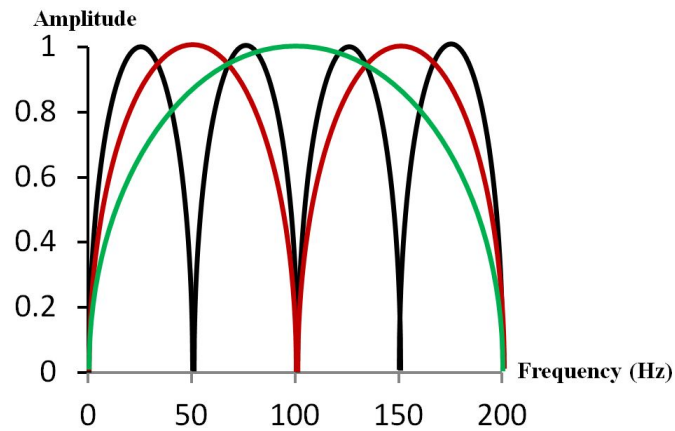


Figure 1.8: Amplitude spectrum for the shots at different depth. The curve in black indicates a deeper source, which has lower notch frequency, while the red and green curves indicate shallower sources which have higher notch frequency.

### 1.2.4  Typical noise in marine seismic data

Good design of acceleration-canceling hydrophones (Evans, 1997) has limited much of the noise, to the extent that in a calm-sea state, signal-to-noise ratio is usually better in marine data than in land data. Noise is also generated by vessel mechanical vibration, cable strumming, and the vortex action of water around the cable. These and other actions result in forces that cause unwanted noise such as swell noise, ship propeller linear noise and poor-blast noise (a sudden sharp noise).

Sea swell causes up-welling and down-drafting of volumes of sea water; this turbulence often generates a short-wave-length vertical pressure wavefieldcausing individual live sections of the cable to raise up or drop down depending on the direction of the surface swell. When individual live sections are moved relative to adjacent live sections, high-amplitude noise bursts are observed.

## 1.3  How the data were processed

After seismic data are acquired in field, they are sent to the processing center. The final goal of processing is to provide the interpreters with a final high resolution broad-band subsurface image, so that they can identify potential hydrocarbon traps and pursue further AVO and seismic attribute analysis. A good model for fully processed seismic data is band-limited reflectivity with real amplitude preserved and noise free. Our raw seismic data are usually subject to a decay in amplitude because of wave-front spreading and frequency-dependent absorption from the intrinsic attenuation of rocks. They also lack low frequency content because the sources is not able to excite low frequency and there is always a ghost notch at 0 HZ. Furthermore, amplitude in seismic data is also uncontrolled because of variable ground conditions and modulate source and receiver. Amplitude preserving processing is critical for the later AVO attribute analysis.

The effect of attenuation must be removed by modifying the amplitude and phase spectrum of the signal, thereby making it broader. Deconvolution is one process that is used to achieve this goal (Yilmaz, 2002). Alternative methods to compensate for frequency attenuation are time-variant spectral whitening and inverse-Q filtering (Yilmaz, 2002). For AVO friendly processing, we won't use AGC (automatic gain control) or trace balancing except for extreme noisy data; normally we will apply wavefront divergence compensation either as a function of velocity or time; but for true amplitude migration, this divergence compensation will be removed , because the migration will handle properly the amplitude loss caused by wavefront spreading.

To obtain a correct subsurface image, we need to derive a reliable velocity field, including anisotropy parameters. Before velocity model building, the fundamental pre-processing steps have been carefully performed in order to feed velocity analysis with input data free of the noise described above and other noise (e.g., multiples, described below), and with a broadband wavelet. These steps are important: if the data are contaminated with noise, multiples, the preprocessing and PSDM will lead to false velocity interpretation. This thesis concentrates mainly on velocity model building. However, leading up to that, the following several paragraphs briefly discuss some major pre-processing steps including noise attenuation, wavelet processing, and multiple removal.

## 1.3.1   Swell noise attenuation

Swell noise is often apparent on marine data, appearing as low frequency high amplitude noise. FX projection filtering (Soubaras, 1994) is used to attenuate this type of noise. First, anomalous high-amplitude spikes are detected by specifying a threshold for the ratio of center point RMS (root mean square) amplitude to the surrounding background RMS amplitude level. These spikes are removed and replaced by interpolated values from adjacent good traces.

Figure 1.9 shows the data comparison before (a) and after (b)swell noise attenuation. Swell noise, which appear as low frequency and high amplitude noise, were removed.

## 1.3.2 Source designature

As described earlier in the acquisition section, interpreters prefer high resolution data. They also prefer "zero-phase wavelets" (which are symmetric around time zero, so that energy begins before time zero), so that the horizon of interpreter's interest appears at the peak or trough of seismic events, which will give best resolution. In marine processing, we perform deterministic deconvolution to achieve this. Because a far field signature for the source wavelet is available for marine data, deterministic deconvolution can be performed in marine processing. The final goal for the source designature is to convert the wavelet to a desirable zero-phase wavelet with the bubble attenuated as well. Figure 1.10 illustrates the wavelet before and after source designature, 1.10(a) is the input minimum phase wavelet before source designature with bubble at around 112ms and 1.10(b) is the final zero-phase wavelet with bubble removed.

## 1.3.3 3D surface related multiple elimination

Marine data are usually heavily contaminated by multiples, and one major processing task is to effectively remove these multiples. Strong contamination from surface multiples is one of the major problems. The air-water sea surface is a strong reflector with reflection coefficients close to -1. The dominant multiples presented in seismic data is water layer related multiples. Water layer related multiples include purely water bottom multiples and peg-leg multiples. Different orders (number of bounces) of water bottom multiples will be generated by seismic waves bouncing back and forth between water bottom and air-water surface. "Peg-leg" multiples refer to those that reflect at least once from both water bottom and subsurface horizons.
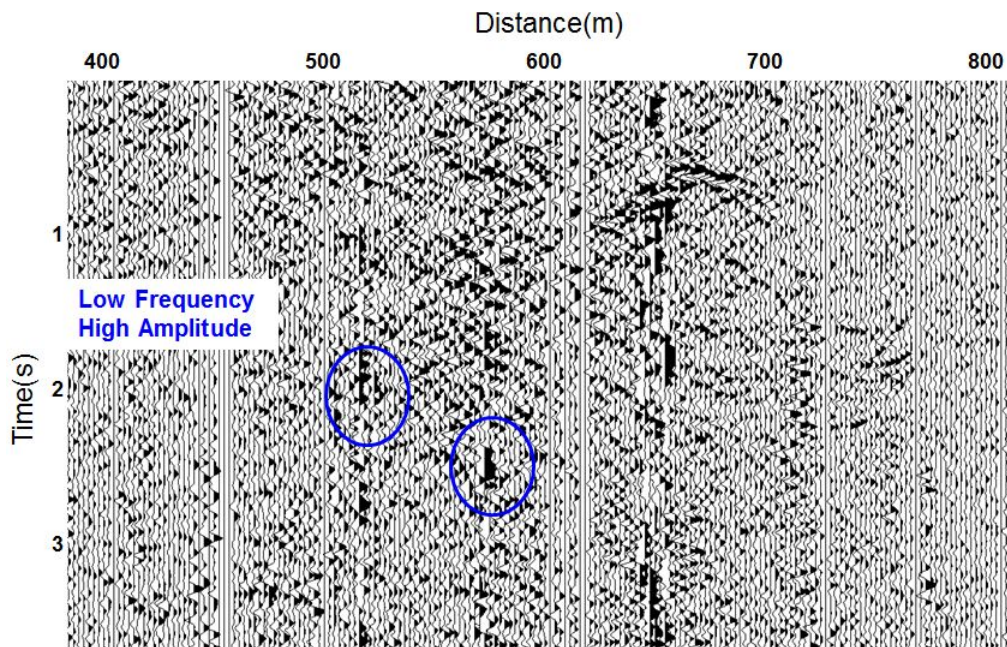
(a) Before swell noise attenuation
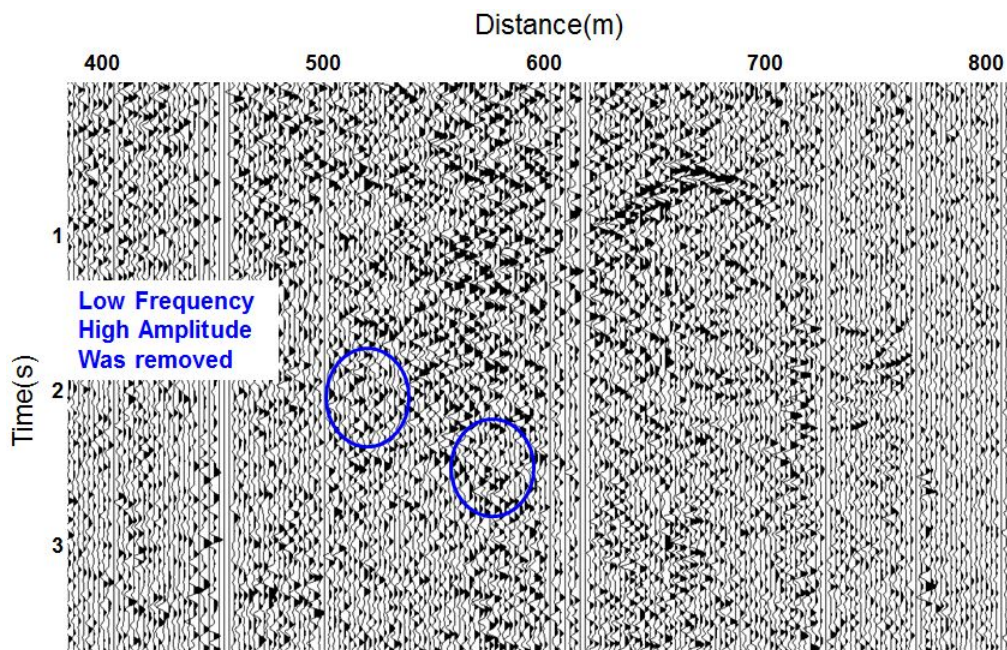


(b) After swell noise attenuation

Figure 1.9: Swell noise attenuation. Swell noise appeared as low frequency and high amplitude noise, they were removed
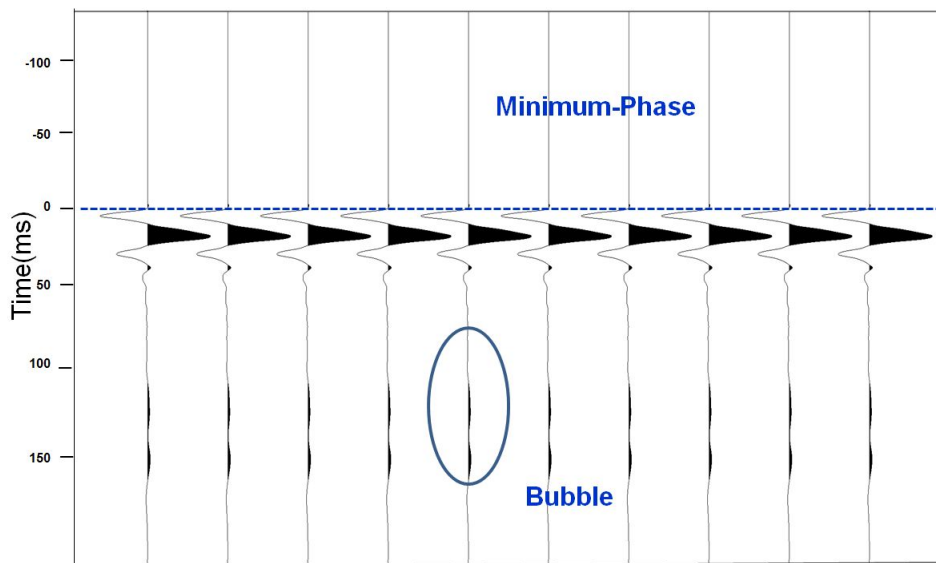
(a) Input wavelet
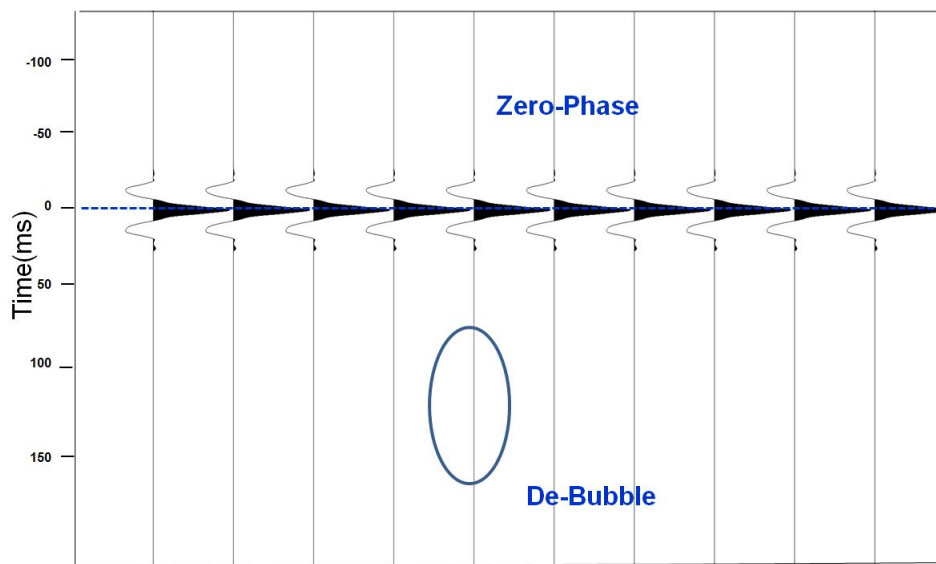


(b) Desired zero-phase de-bubbled wavelet

Figure 1.10: The wavelet before and after source designature. The top (a) shows the input minimum phase wavelet before source designature with bubble at around 112ms, the bottom (b) shows the final zero-phase wavelet with bubble removed.

3D Surface-related multiple elimination (SRME) (Biersteker, 2001; Lin et al., 2004) is a robust method to suppress the surface related multiples. Before 3D SRME was developed, techniques based on high-resolution radon transforms (Kabir, et al; Hargreaves et al, 2001) were used to get rid of multiples, and these had several drawbacks. First, they require the ability to distinguish velocity or move-out difference between primary and multiple events; second, they produce artifacts at near offsets, third, they can only handle the multiples whose move-out is hyperbolic. By contrast, 3D SRME is purely data driven, needs no velocity information, and can handle complex multiples with non-hyperbolic or non-parabolic shapes.

3D SRME is a summation process as illustrated in Figure 1.11. On the sea surface the aperture defines the range of potential secondary source locations, $\boldsymbol{R'}/\boldsymbol{S'}$. These are decomposed into subsurface locations defined by CMP locations, traces from source side $\boldsymbol{S}_c$ and traces from receiver side $\boldsymbol{R}_c$. 3D SRME can predict multiples in third traces by convolving two primary traces , then sums up all convolved pairs within a specified aperture.

3D SRME is a computationally intensive process, requiring large CPU time and disk space. Before multiple model prediction begins, the input data need to be careful preconditioned including zero-dephasing, noise removal. 3D SRME needs traces at every source and receiver location, so trace interpolation is performed to ensure there are all "recorded" traces needed for predicting the multiples.

After the multiple model is predicted, an adaptive subtraction is conducted to subtract the multiple model from the input. Figure 1.12 shows common channel data comparison before and after 3D SRME. The diffracted multiples pointed by blue arrows is the most difficult area for normal radon demultiple to work, because the ray paths for multiples are complex, and events will appear as non-hyperbolic in CMP gathers. Figure 1.12 (b) shows the subsurface structure was brought out after the multiples on top of the structure

$$M(S,R) = \int Sc'^*Rc'$$
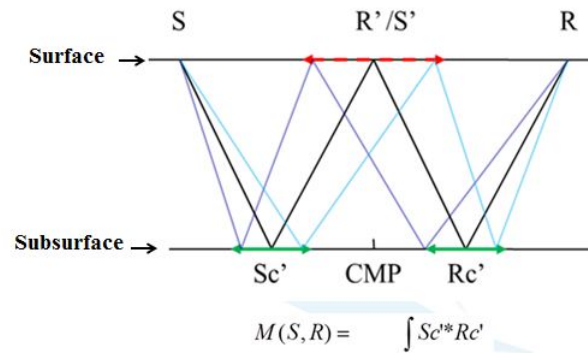
Figure 1.11: Basic principle for 3D SRME. The red dotted line represents the surface aperture which defines the range of potential secondary source locations, $\boldsymbol{R'}/\boldsymbol{S'}$. Green lines indicate the subsurface CMP locations for the primary traces from source side $\boldsymbol{S}_c$ and primary traces from receiver side $\boldsymbol{R}_c$. 3D SRME convolves these two primary traces to predict multiples in the third traces (combining the raypath from S to $R'$ and $S'$ to R). The multiple M(S,R) is expressed as the sum of all convolved pairs within a specified aperture (CGGVeritas, 2009).
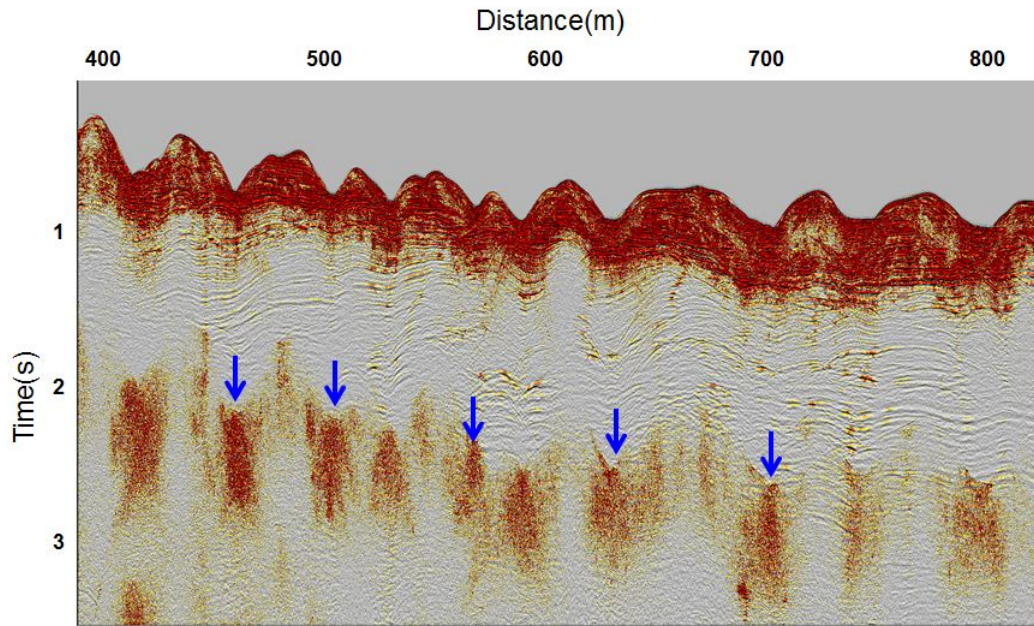
(a) Common channel before 3D SRME
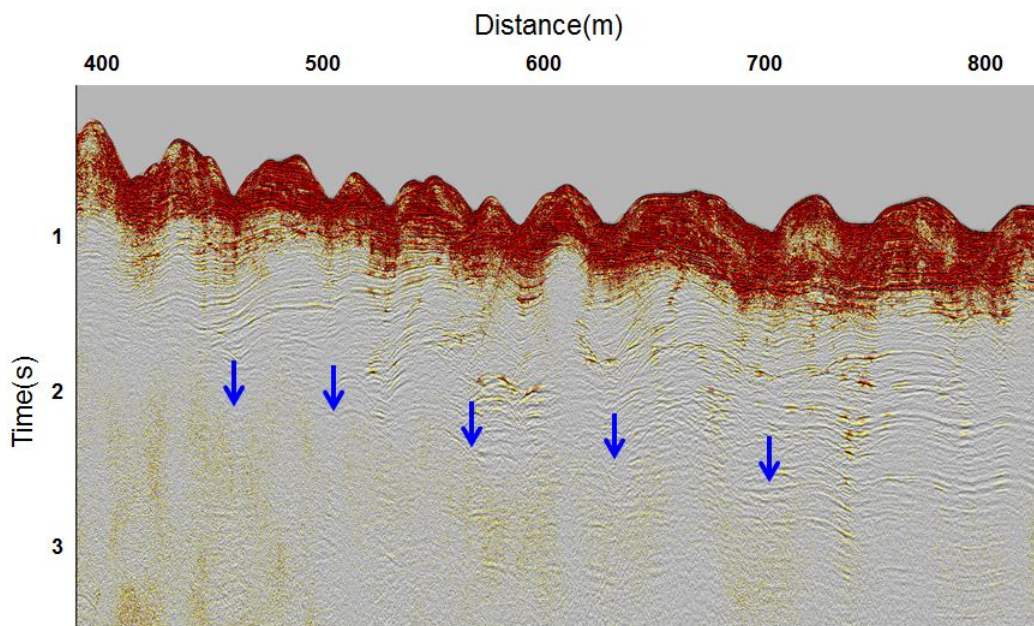


(b) Common channel after 3D SRME

Figure 1.12: Seismic section before and after 3D SRME. The multiples pointed by blue arrow in Figure (a) was removed by 3D SRME as shown in Figure (b), the primary buried underneath the multiples was brought out after the multiples on top it were removed (CGGVeritas, 2009).

were removed.

## 1.4 Migration algorithm

As mentioned in the very beginning, after all wavelet processing, noise and multiples removal, migration will be the last step of processing to spatially re-position events and improve focusing. Figure 1.13 shows a seismic section in the form of a common-offset record before migration. This section provides a remarkably coherent picture of subsurface structure, but it is not correct, suffering from several distorting effects, most notably those of diffraction from geologic bed truncations and lateral movement of the energy between the reflection points on dipping beds and the surface location (Gray, 2001). Migration was one of the earliest seismic imaging tools to collapse the diffraction energy and move the subsurface reflectors to their correct positions as shown in Figure 1.14.
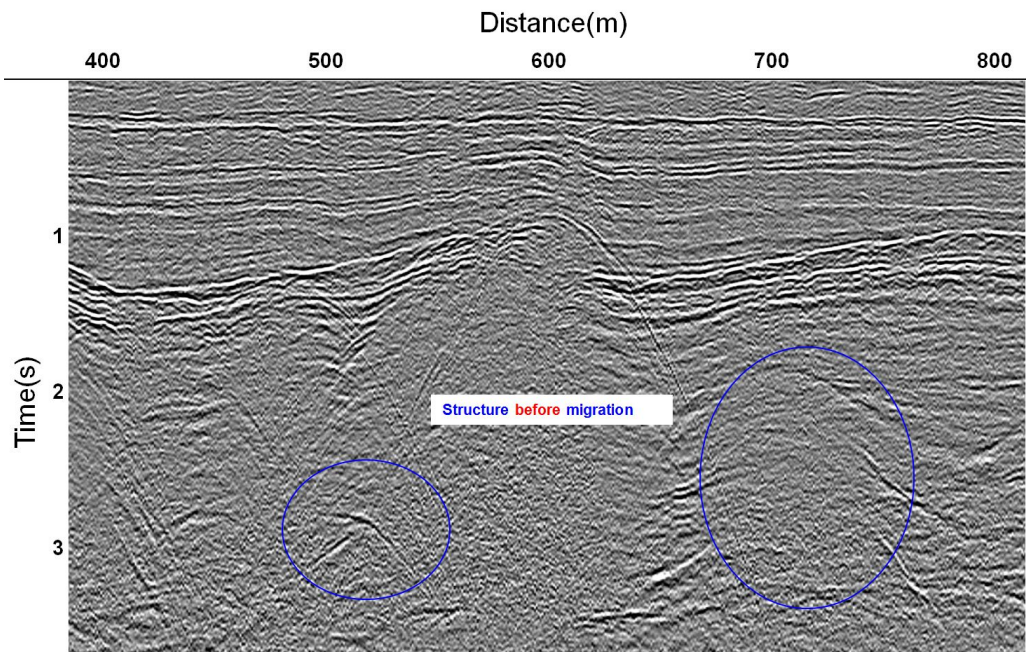


Figure 1.13: Subsurface images before migration (CGGVeritas, 2009)

The final goal of a migration is to transform the seismic data into band-limited reflec-
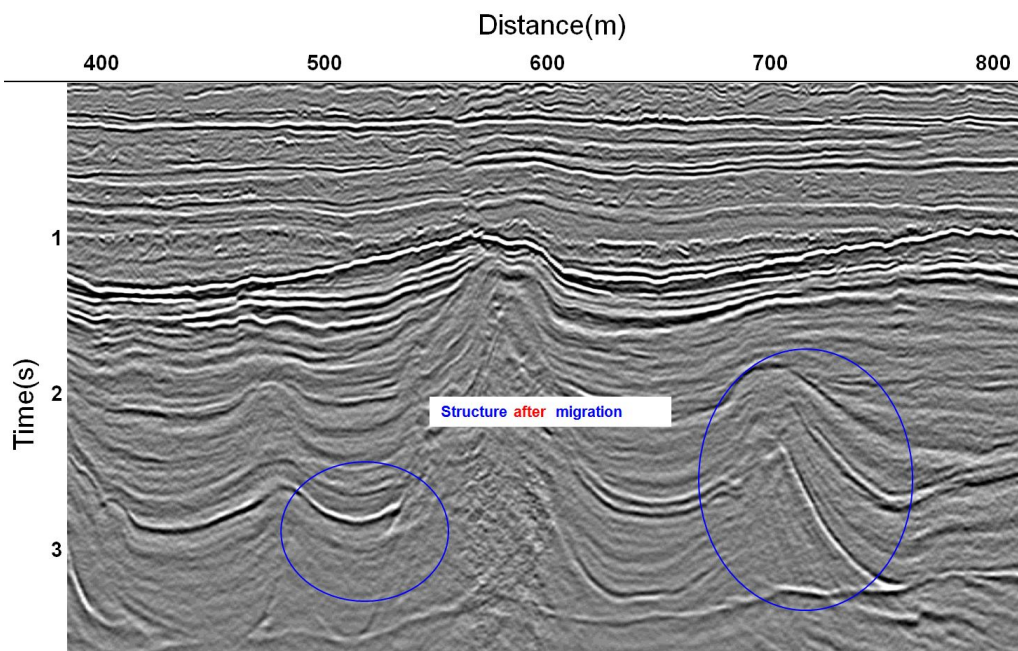
Figure 1.14: Subsurface images after migration (CGGVeritas, 2009)
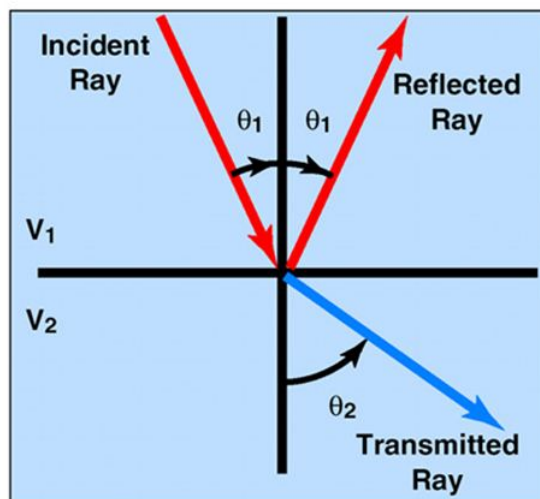


Figure 1.15: Reflection coefficients

tivity (Margrave, 2012). Figure 1.15 presents a simple two-layer medium. with velocities $v_1$ and $v_2$ and densities $\rho_1$ and $\rho_2$ for each layer. For the simplest one dimensional layered medium, the normal-incidence reflection coefficient for P-waves is given by

$$R_0 = \frac{\rho_2 v_2 - \rho_1 v_1}{\rho_2 v_2 + \rho_1 v_1}. \tag{1.1}$$

In the case of nonnormal incidence in acoustic media (S-wave velocity equal to 0) the corresponding reflection coefficient R can be written in a similar form (Santos et al, 2004)

$$R = \frac{\rho_2 v_2 \sec \theta_2 - \rho_1 v_1 \sec \theta_1}{\rho_2 v_2 \sec \theta_2 + \rho_1 v_1 \sec \theta_1}. \tag{1.2}$$

Explorationists should require the amplitudes in their seismic images to be directly related to the properties of the interfaces causing the reflections. The amplitudes of prestack migrated traces should thus be related to angle-dependent reflection coefficients. If the migration algorithm gives amplitudes that can be directly related to reflection coefficients, then the process can also be considered to be an inversion algorithm (Bleistein, 1999; Thierry et al, 1999).

True amplitude Kirchhoff pre-stack depth migration was performed on the seismic data in this thesis. In the following several paragraphs, the Kirchhoff migration method used in this thesis will be described in detail.

### 1.4.1  Acoustic wave equation

The seismic data processed in this thesis are from P wave, sub-critical reflection seismic energy from the subsurface of the Earth. It is well known that waves generated by earthquakes will travel in horizontal as well as vertical directions. The P wave (primary wave) is defined as the wave motion in which particles move in the same direction as the wave propagation. The S wave (secondary wave) is defined as the wave motion in which particles move perpendicular to the direction of wave propagation. Seismic images can be produced from either reflected or refracted seismic waves. The reflection method is

dominant in exploration geophysics. It is known that the reflection coefficient of the reflected waves increases sharply beyond the critical angle. The reflected events from the Earth's crust can be divided into two groups a) sub-critical or near vertical reflections, and b) post critical or wide angle reflections. The data processed in this thesis is reflection energy within sub-critical group.

The migration algorithm described in this thesis assumes acoustic wave propagation, and this approximation is usually adequate if our goal is to image P-waves in sedimentary basins. Mathematically, the acoustic wave equation describes the propagation of compressional waves (P-waves) in fluids (e.g., sound waves in air or water). The commonly used scalar wave equation for a pressure wavefield $\psi$ in an inhomogeneous fluid is

$$\frac{\partial^2 \psi}{\partial x^2} + \frac{\partial^2 \psi}{\partial y^2} + \frac{\partial^2 \psi}{\partial z^2} = \frac{1}{v^2} \frac{\partial^2 \psi}{\partial t^2}. \tag{1.3}$$

### 1.4.2  Kirchhoff migration

As stated earlier, the final goal of migration is to get the best focused image at the correct lateral and vertical position with true amplitude. The following paragraphs will describe how Kirchhoff migration gets correct structural images kinematically and true amplitude dynamically.

Kirchhoff migration (Schneider, 1978) is one of the oldest migration schemes, and it is still in prominent use because of its versatility and robustness. Since Kirchhoff migration is accurate, and is one of the cheapest migration methods, it has been the workhorse of the processing industry (Gray, 2001). Kirchhoff migration, whether implemented pre- or post-stack, or as a time or depth migration, works in the same basic manner.

For a given sample location ($x$,$y$,$t$ or $z$) on what will be the migrated data (i.e. the output section), a diffraction curve is defined that is mapped onto the input (unmigrated) data. The shape of the diffraction curve is defined by different methods for time and depth Kirchhoff migration, but it is fundamentally controlled by the migration ve-

locity model and the migration aperture. The energy on the unmigrated data at the specific positions and travel-times matching that of the calculated diffraction shape are interpolated, filtered to prevent aliasing, and weighted as a function of distance from the diffraction apex. Then the weighted amplitude values intersected by the diffraction hyperbola are summed and placed at the output sample on the migrated section as amplitude value. A wave-shaping filter is then applied as a phase correction. At this point, the output sample is considered migrated. Migration of the entire data set is completed by repeating this process for all samples on the output section (Bancroft, 1996). The kinematics of Kirchhoff migration are illustrated in Figure 1.16.
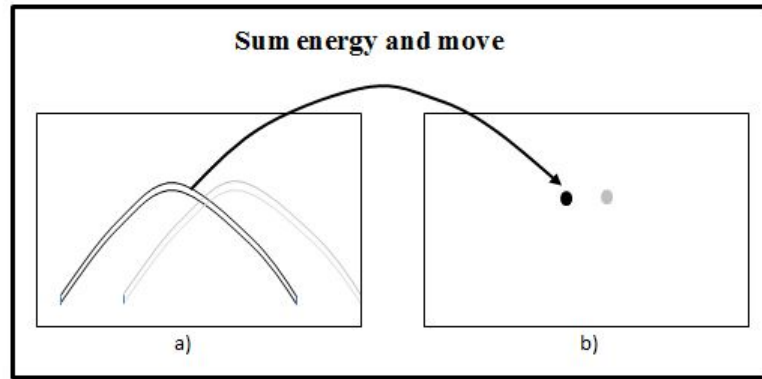


Figure 1.16: Illustration of Kirchhoff migration. (a) A diffraction for an output sample point in (b) is mapped onto (a). (b) Energy on the diffraction curve in (a) is summed and placed at the scatter point location in the migrated section (b) (from Bancroft, 2001a).

The diffraction curves for Kirchhoff depth migration are defined by traveltime. A direct method to compute travel-times is ray tracing through the specified velocity-depth model, as illustrated in Figure 1.17. Given a source and receiver point on the recording surface and a subsurface location, a ray emerging from the source, propagates into the subsurface which is identified by layer boundaries with velocity contrasts. The traveltime from the source location at the surface to a reflection point at the subsurface is then

calculated by integrating the elements of distance along the ray-path divided by the velocities associated with those elements. By applying reciprocity, the travel-time from a receiver location at the surface to a reflection point in the subsurface can be computed in the same manner. Finally, for a given source-receiver pair at the surface and a reflector in the subsurface, the total traveltime is computed by adding the travel-time from the source to the reflector to the travel-time from the reflector to the receiver.

Migration operators either collapse diffraction hyperbolas into a diffractors as just described, or swing input samples into output semicircles ("smile"). When we perform Kirchhoff migration, we first form a "smile" operator for all the input samples, and then we sum all the smiles. Through the constructive and destructive interference of these smiles implicit in the wave equation 1.3, the imaged reflectors align along the envelopes of the family of smile curve.
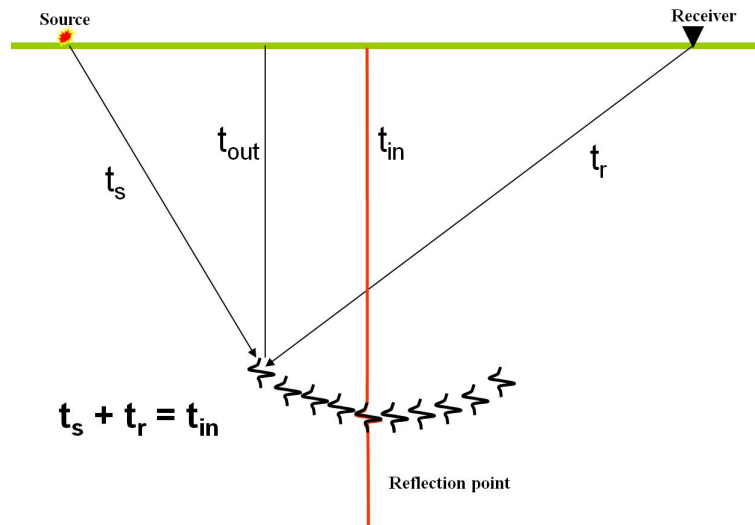


Figure 1.17: Illustration of travel time. $t_s$ is the traveltime from the source location at the surface to a reflection point at the subsurface. $t_r$ is the traveltime from the receiver location at the surface to a reflection point at the subsurface. The total traveltime for a given source-receiver pair is $t_s + t_r$.

Although the kinematics of Kirchhoff migration is easy to comprehend, there are

many factors to consider in order to obtain "true amplitude" from a prestack migration. Prestack Kirchhoff imaging can, and sometimes does, just "smile" the input traces without any consideration of the amplitudes of the migration operator. This can give an accurate migrated image, but the migrated amplitudes will generally be unreliable (see Dellinger et al., 1999, for an example). It is important for the explorationist to be aware that there are many ways to approximate the amplitude weights for Kirchhoff migration (see Hanitzsch, 1997; Dellinger et al., 1999; Zhang et al, 2000). The amplitudes of these varying approximations will all be slightly different, with varying levels of accuracy in varying situations.

Drawing on work by Bleistein et al. (1998) and others, Zhang et al (2000) presented formulas for 3-D Kirchhoff migration weights in a depth-varying (v(z)) medium. The Kirchhoff algorithm used in this thesis mostly complies with what Zhang et al described. The following paragraph extracts the main conclusions from Zhang et al's paper.

Bleistein et al. (1998) present a general formula for 3-D prestack Kirchhoff migration:

$$\beta(x) = \frac{1}{8\pi^3} \int_v w(x,\xi) e^{i\omega(\tau_s+\tau_r)} u_s(x_r, x_s, \omega) i\omega d\omega d^2\xi, \tag{1.4}$$

where

$$w(x,\xi) = \frac{|h(x,\xi)|}{A(x,x_s)A(x_r,x)|\nabla(\tau_s+\tau_r)|^2}. \tag{1.5}$$

is the migration weight. In (1.4), x, y, $x_s$, $x_r$ are all 3D position vectors. $\beta(x)$ is the reflection coefficient, $u_s(x_r, x_s, \omega)$ is the scatter wavefield at frequency $\omega$ for source at $x_s$ and receiver at $x_r$ ( this is our seismic data). In (1.5), A(x,y) is the amplitude of Green's function with source at y and observation point at x, $\tau_s(\tau_r)$ is travel-time between source (receiver) and image point, $x_s(\xi)$ and $x_r(\xi)$ are source and receiver points, respectively, $\xi = (\xi_1, \xi_2)$ is the parameter labeling source and receiver points, and

$$h(x, \xi) = \det \begin{vmatrix} \nabla(\tau_s + \tau_r) \\ \frac{\partial}{\partial \xi_1} \nabla(\tau_s + \tau_r) \\ \frac{\partial}{\partial \xi_2} \nabla(\tau_s + \tau_r) \end{vmatrix}$$

is the Beylkin determinant, the Jacobian of the transformation from subsurface coordinates (where the imaging takes place ) to surface coordinates (where the integration is performed). For a given image point the Beylkin determinant serves to normalize by directional fold, where "directional fold" means the total number of contributions from all the input traces arriving at the image point from a particular direction, namely the average of the ray directions from the source and receiver locations. Also in (1.4) $w(x, \xi)$ is the weight for true amplitude migration. Zhang et al derive an accurate migration weight function for v(z) media as

$$w = \frac{z}{v^2} \left( \frac{t_s}{t_r} + \frac{t_r}{t_s} \right) \left( \frac{1}{t_r} + \frac{1}{t_s} \right), \tag{1.6}$$

and they presented an approximation to the 3-D weight that provides accurate migrated amplitudes with a significant reduction of migration computation.

$$w = \frac{z}{v_0} \left( \frac{1}{t_s t_r} + \frac{1}{t_r t_r} \right) t. \tag{1.7}$$

To get true amplitude migration, in practice an anti-aliasing filter must be applied during migration. When doing summation along the diffraction curve, migration assumes reflectors and seismic data exist at all points in space. In reality, our seismic data are sampled at discrete spatial locations. As a result, not all the unwanted energy cancels, and seismic sections will be left with some noise. To overcome this problem, an anti-aliasing filter can be applied, which depends on input trace spacing, frequency and dip (Lumley et al., 1994, Abma et al., 1999, Zhang et al., 2001). This filter attenuates the higher frequencies of the more steeply dipping flanks of the migration smiles.

The central feature of Kirchhoff depth migration is to image any subsurface point from calculation of integral (1.4) through surface data using ray tracing. This method has a lot of flexibility and can be run very efficiently with minimal memory requirement. Because most production Kirchhoff migration programs use single arrivals - often the earliest arrival or the most energetic arrival- it limits its ability to image complex areas.

Kirchhoff migration is conceptually simple, and it is very versatile. These properties alone do not guarantee that Kirchhoff migration will be accurate; however, it has proved to be remarkably accurate in a wide variety of imaging applications.

## 1.5   Summary

This chapter gave an overview of seismic imaging including the history of seismic imaging, seismic acquisition, seismic processing and migration algorithms.

Starting from the nineteenth century, man-made seismic waves have been utilized to help locate its mineral, water, and hydrocarbon resources (Reddy, 2012). Seismic acquisition techniques, and related imaging techniques, have been developed over more than a century. In the 1920s, the reflection method was started; in the 1950s, "Kirchhoff diffraction stack" method was given birth; in the 1970s, explosive development of migration algorithms took place. The advent of 3-D seismic in the 1980s helped to advance the development of computer power; ever growing computer power allows 3D prestack depth migration to work both efficiently and cost effectively. Today, with the growing understanding of anisotropy and anisotropic imaging, better resolution and illumination from RTM and advanced velocity updates from FWI, seismic imaging techniques continue to evolve.

This chapter also described several aspects of seismic acquisition, including survey design, source signature, and source and receiver ghosts effects. With the ultimate goal

of producing an interpretable image and, at the same time, minimizing the acquisition and processing costs of the survey, 3D survey design begins with considering depth, areal extent and the largest dip, and follows by careful consideration of both vertical and lateral resolution in order to get clear subsurface images. Marine acquisition uses air guns to generate a pressure wave-field. In marine source array design, the main goal is to optimize the array's primary-to-bubble ratio. For marine acquisition, the source and receivers are placed several meters beneath the sea surface; the waves propagating to and reflecting back from the sea surface will interfere with the direct downgoing waves from the source, with the opposite polarity, causing a notch in frequency spectrum. This is so-called "source and receiver" ghost effects.

After seismic data have been acquired in the field, seismic processing aims to produce subsurface images with correct lateral and vertical position and with the amplitude proportional to the refection coefficients in the subsurface. Seismic processing involves several stages: the preprocessing to do wavelet processing, noise and multiples removal; velocity model building to derive a reliable velocity field for the final migration, and finally migration to spatially re-position events and improve focusing. Kirchhoff migration, the algorithm used in this thesis, was described in detail. True amplitude Kirchhoff pre-stack depth migration was performed on the seismic data in this thesis. This chapter described how Kirchhoff migration gets correct structural images kinematically and true amplitude dynamically, and presented the central feature of Kirchhoff depth migration, which is to image any subsurface point from calculation of an integral (equation 1.4) of surface data, using ray tracing.

A good velocity model is the key to success for pre-stack depth migration. This thesis will concentrate on how the velocity model has been built for a particular survey. In the following chapters, velocity model building will be discussed in detail. With the best input and the best velocity model possible, migration will move the subsurface events to

their correct vertical and lateral positions. Clients will be provided with seismic images for structural and stratigraphic interpretation.

# Chapter 2

# Migration velocity analysis

This chapter will present a literature review of migration velocity analysis in seismic data processing. First, the basic theory for migration velocity analysis is reviewed. Second, the general velocity model building flow is presented, the main techniques used by this thesis are described including vertical update, tomography analysis and anisotropy parameter estimation. Last, the basic concept of weak polar anisotropy is introduced. The objective of this literature review is to provide the insights and basic understanding of routine industry-scale velocity analysis. Although a rich experience is important for a seismic processor to derive a good velocity model, a solid understanding of the theory behind different methods of velocity analysis will help processors make good judgments and avoid pitfalls.

## 2.1 Theory

### 2.1.1 Velocity category

There are many velocity names in exploration seismology. There are interval velocity, instantaneous velocity, apparent velocity, root mean square (RMS) velocity, average velocity, mean velocity, stacking velocity, horizontal velocity, vertical velocity, phase velocity, group velocity, P-wave velocity, S-wave velocity, migration velocity, weathering velocity, and almost certainly others (Margrave, 2012). There is a fundamental distinction between physical velocities and velocity measurements. The former refers to velocities that are actually the speed at which some physical wave propagates. Examples are instantaneous velocity, P- and S- wave velocities, phase and group velocity (Margrave,

2012). On the other hand, velocity measures are typically quantities derived from data analysis that have the physical dimensions of velocity but are related to physical velocities in some indirect fashion. Examples of velocity measures include average, mean, and root mean square (RMS) velocities, interval velocity, stacking velocity, apparent velocity, and migration velocity (Margrave, 2012).

A sonic log represents direct measurement of the velocity with which seismic waves travel in the earth as a function of depth. Seismic data, on the other hand, provide an indirect measurement of velocity. This thesis mainly concentrates on migration velocity analysis using seismic data.

Velocity plays a dual role in seismic imaging: (1) it affects focusing of the data and (2) it determines positioning of the imaged reflectors (Biondi, 2007). The RMS (root mean square) velocity, $v_{rms}$, is a well-known example of a focusing-velocity function. The interval velocity used to convert pre-stack time migrated sections to depth sections is an example of a mapping-velocity function. In depth migration, the interval velocity function determines both the focusing and the mapping of the data.

Most velocity estimation methods are based on measurements of the kinematics of the reflections. An important differentiation among velocity estimation methods is whether kinematics are measured directly from the data in the time domain prior to migrating the seismic data or are measured from the results of migration in the image domain. When geologic structures are simple and lateral velocity variations are smooth, the data-domain methods usually provide robust and accurate estimates of both the focusing and mapping velocities. However, when geologic structures and/or the velocity functions are complex, data-domain methods often fail. Because of this, we need to leverage the power of migration to focus and simplify the data. This will enable us to reliably measure the kinematics of the reflections and converge toward accurate velocity estimates (Biondi, 2007).

The NMO velocity, stacking velocity and RMS velocity are obtained from the data in the time domain, while migration velocity for pre-stack depth migration is estimated from the data in the image domain; pre-stack time migration can be a combination of both.

### 2.1.2  Factors affecting the velocity

It is important for both interpreters and seismic data processors to know some relationships among the intrinsic rock properties and the measured velocities. Lithology, pressure, and fluids all affect velocity. Seismic velocities within crustal rocks vary widely: typically shale has a low velocity, carbonates have a velocity of approximately 6000m/s and salt velocity is around 4480 m/s. Seismic surveys yield maps of the distribution of seismic velocities, interfaces between rock units and, ideally, of reflection coefficients at these interfaces.

Generally, the velocity is dependent on the elastic moduli and density via:

$$V_p = \sqrt{\frac{k + \frac{3}{4}\mu}{\rho}}. \tag{2.1}$$

where k is bulk modulus, $\rho$ is density and $\mu$ is modulus of rigidity

1) Porosity. The porosity of a rock also affects its velocity. A very rough rule due to Wyllie (1958) is the so called time average relationship (where $\phi$ is porosity):

$$\frac{1}{v_{bulk}} = \frac{\phi}{v_{fluid}} + \frac{1 - \phi}{v_{matrix}}. \tag{2.2}$$

Pore shapes, pore pressure and pore fluid saturation all influence interval velocity within a rock (Gassman, 1951).

2) Lithification.

Also known as cementation. The degree to which grains in a sedimentary rock are cemented together by post depositional, usually chemical processes, has a strong effect

on the moduli. By filling pore space with minerals of higher density than the fluid it replaces the bulk density is also increased. The combination of porosity reduction and lithification causes the observed increase of velocity with depth of burial and age (Sheriff and Geldart, 1995).

3) Pressure

Compressional wave velocity is strongly dependent on effective stress. In general velocity rises with increasing confining pressure and then levels off to a "terminal velocity" when the effective pressure is high. The effect is probably due to crack closure. At low effective pressure cracks are open and easily closed with an increase in stress. As the effective pressure increased the cracks are all closed, k goes up and the velocity increases.

It is observed from seismic surveys that velocities usually increase with depth. Densities also increase with depth so it must be that the bulk and shear moduli increase faster than the density. In seismic exploration there are many empirical relationships between velocity and depth of burial and geologic age.

## 2.1.3   Stacking velocity

Velocity estimation requires the data recorded at nonzero offsets provided by common-midpoint (CMP) recording. With estimated velocities, we can correct reflection travel-times for nonzero offsets and stack all the traces from different offsets into one trace for a certain CMP. The reliable velocity would be the one which yields the best stack.

For a single constant-velocity horizontal layer, the reflection traveltimes curve as a function of offset is a hyperbola. The time difference between traveltimes at a given offset and at zero offset is called normal move out (NMO) (Yilmaz, 2002). The velocity required to correct for normal move out is called normal move out velocity. For short offsets, the NMO velocity for a horizontally layered earth model approximates the RMS velocity down to the layer boundary under consideration (Dix, 1955). There is a difference between the

NMO and stacking velocities. The NMO velocity is based on the small-spread hyperbolic traveltime, while stacking velocity is based on the hyperbola that best fits data over the entire spread length (Yilmaz, 2002). Nevertheless, stacking velocity and NMO correction velocity generally are considered equivalent.

It is worth mentioning that velocities required by stacking and migration are not necessarily the same. For a single dip reflector, stacking velocity is the velocity of the medium above the reflector divided by the cosine of the dip angle, while migration velocity is the velocity of the medium itself (Yilmaz, 2002). The migration velocity analysis will be discussed in the following sections.

### 2.1.3.1 Taylor expansion NMO equation

Consider a reflection event on a CMP gather. The difference between the two-way time at a given offset and the two-way zero-offset time is called normal moveout (NMO) (Yilmaz, 2002). Reflection traveltimes must be corrected for NMO prior to summing the traces in the CMP gather along the offset axis. We now consider a medium composed of horizontal iso-velocity layers. Considering the raypath from source S to depth point D, back to receiver R, associated with offset x at midpoint location. Taner and Koehler (1969) derived the traveltime equation for this path:

$$t^2 = c_0 + c_1 x^2 + c_2 x^4 + c_3 x^6 + \dots \tag{2.3}$$

where $c_0 = t_0^2, c_1 = \frac{1}{v_{rms}^2}$, and $c_2, c_3, c_4 \dots$ are complicated functions that depend on layer thickness and interval velocity. The RMS velocity $v_{rms}$ down to the reflector on which depth point D is situated is defined as

$$v_{rms}^2 = \frac{1}{t_0} \sum_{i=1}^{N} v_i^2 \Delta \tau_i, \tag{2.4}$$

where $\Delta\tau_i$ is the vertical two-way time through the ith layer and $t_0 = \sum\limits_{i=1}^{N} \Delta\tau_i$. By making the small-spread approximation (offset small compared to depth), the series in equation (2.3) can be truncated to obtain the familiar hyperbolic form

$$t^2 = t_0^2 + \frac{x^2}{v_{rms}^2}. \tag{2.5}$$

### 2.1.3.2 Fourth order

To obtain the fourth-order moveout equation, drop higher-order terms in equation (2.3)

$$t^2 = c_0 + c_1 x^2 + c_2 x^4, \tag{2.6}$$

where $c_2 = \frac{1}{4}\frac{\mu_2^2 - \mu_4}{t_0^2 \mu_2^4}$, with the additional definitions of the terms (Castle, 1994)

$$\mu_j = \frac{1}{t_0} \sum\limits_{i=1}^{N} v_i^j \Delta\tau_i. \tag{2.7}$$

### 2.1.4 Pre-stack time migration (PSTM) velocity model building

Time imaging is based on estimated RMS (x, y, t) velocity where small source/receiver offset and lateral homogeneity local to image point (x, y, t) are assumed.

This velocity field is free to change from point to point. So time migration, in essence, performs a constant-velocity migration at each image point, where the constant changes from point to point (Gray, 2009). An event on a pre-stack time-migrated gather, indexed by offset, can be corrected for residual NMO exactly as in stacking velocity analysis. The locally constant velocity assumption allows this simple analysis. There are several ways to do pre-stack time migration velocity analysis. One way is to estimate imaging velocities using unmigrated CMP gathers (Gardner et al., 1974). Depending on the spatial resolution requirements, velocities are usually picked on a 500m x 500m subset of the imaging grid (migration output at a regular spacing). Imaging velocities are chosen to

make the gathers flat, and the imaging velocity field, considered to be the RMS velocity field, is converted to interval velocity, which is the average velocity in an interval between two reflectors, by using the Dix (1955) formula:

$$v^2(\tau_N) = \frac{\tau_i v_{rms}^2(\tau_i) - \tau_{i-1} v_{rms}^2(\tau_{i-1})}{\Delta \tau_i}. \tag{2.8}$$

In areas of structural complexity, Dix inversion can produce completely unrealistic interval velocity values.

PSTM velocity analysis can also be conducted in the image domain using pre-stack time migration data on a regular grid (Biondi, 2007). It is standard practice to sort data for Kirchhoff migration to common offsets and migrate each sorted data volume separately. This way, the data can be gathered after each migration and sorted by their original surface offsets. Velocity analysis in the image domain is more accurate than analysis in the unmigrated data domain, because migration can move the events to their correct location and simplify the data by eliminating crossing events and unmigrated diffraction signatures.

Pre-stack time migration is efficient and the result is relatively good (compared with post-stack migration), but in the presence of lateral velocity variations, the assumptions of NMO velocity analysis are inaccurate, and a more robust and accurate velocity analysis method is needed.

### 2.1.5 Pre-stack depth migration (PSDM) velocity model building

Based on an accurate model of wave propagation in reflection seismology, pre-stack depth migration (PSDM) can produce correct subsurface images. Meanwhile, PSDM requires a highly accurate velocity field. A good velocity determination strategy therefore becomes very important. It has been recognized that pre-stack depth migration by itself is the most powerful velocity determination tool (Al Yahya, 1987, Faye and Jean-

not, 1986). The basic assumption underlying velocity determination methods based on pre-stack migration is that when the velocity is correct, all migrations with data from different domains (e.g. different offsets, different shots, different angles etc.) must yield a consistent subsurface image. Conversely, when the velocity is not correct, the difference between the images can be used to improve the existing subsurface model.

### 2.1.5.1    Model building approaches

With best input data processed as described in first chapter, pre-stack depth migration is performed to generate common image gathers (CIG). Observation of moveout, the change in arrival time with offset in CIGs, are the basis for estimating velocities from seismic data. Moveout is a consequence of subsurface structure and velocity (Fagin, 1999).

There are different common image gathers such as common offset image gathers, angle domain common image gathers, and shot profile migrated common image gathers. If common offset Kirchhoff prestack depth migration was performed to generate these CIGs, we called it common offset image gathers; these CIGs have same subsurface reflection point and indexed by surface offset between source and receiver. However, if shot-records are migrated independently, then common offset (s-r) labels are not possible. Instead the traces must be labeled by the distance from the shot location of a migrated shot to the image point, this is shot profile migrated common image gathers. CIGs in this thesis all refer to common offset CIGs.

Seismic velocity estimation techniques can be categorized on the basis of three characteristics (Fagin, 1999). First is parametrization of the velocity model, i.e, how geologic structure will be represented, (layers vs grid); Second is the data used for velocity analysis, i.e, whether it is (unmigrated) time gathers or (migrated) depth gathers; Third are changes of velocity, i.e, whether it is one-dimensional or multidimensional.

1. Velocity model representations which utilize a structural framework vs. those that do not

   - Layered model building approach: this method estimates velocities by utilizing a structural framework of geologic horizons.

   - Grid based model building approach: these methods make no use of a structural framework. In this case velocities are interpolated between the velocity functions, or along time or depth slices. Sometimes, layers and grids are combined.

   If velocity variation is most influenced by geology age, lithology or pressure, layered model building approaches are preferred. If velocity is most influenced by depth, it is desirable to use the grid based model building approach.

2. Time gather methods vs. depth gather methods

   Time gather methods estimate velocity based on moveout observations in the unmigrated CMP time gathers. traveltime tomography measures the difference between ray-modeled traveltimes and observed traveltimes, as picked on unmigrated CMP gathers, and tries to build a model that minimize the traveltime differences. Depth gather methods estimate velocity using CIGs obtained from prestack depth migration. Depth gather tomography falls into this category. Depth gather tomography and traveltime tomography have a crucial difference. In depth gather tomography, traveltime errors are measured and used indirectly from the migrated images; the direct goal is to build a velocity model that minimizes the residual depth moveout measured from migrated common image gathers (CIGs).

3. One-dimensional vs. multi-dimensional methods

Similar to stacking velocity analysis, one-dimensional methods derive velocities by assuming a flat, unstructured surface; the velocity update is only local to each gather location without consideration of neighboring gathers. Multi-dimensional methods use ray tracing to model the effect of structure and velocity on moveout. The velocity update is conducted in 3D. In the presence of complex structure, multi-dimensional methods are essential to derive accurate velocities.

### 2.1.6 Frowns and smiles in velocity analysis

As mentioned above, accurate depth migration of seismic reflectors requires accurate velocity estimations. Inaccurate velocity estimates will cause systematic moveout artifacts such as so-called "smiles and frowns" to appear on depth-migrated CIGs. The elimination of these moveout features by adjusting seismic velocities is the goal of migration velocity analysis; in turn, it allows depth migration to be used as a powerful velocity analysis tool. It can be argued on the basis of model studies (Lines et al., 1998) and with real data examples (Whitmore and Garing, 1993) that iterative pre-stack depth migration provides a very general velocity analysis method for structurally complex media. Smiles and frowns in migration/velocity analysis provide the basis for depth migration velocity analysis. In understanding the case of post-stack migration, consider an example with two point diffractors in the middle of a uniform medium with velocity v = 4000 m/s. The depths of the diffractors are 600 and 800 m, respectively. We now examine the migration of a point diffraction seismogram from this model recorded by coincident source-receiver positions. The zero-offset section is shown in Figure 2.1. The images obtained by migrating the input diffraction hyperbola in Figure 2.2 are compared for the cases where the velocity is too low (Figure 2.2a), exactly correct (Figure 2.2b), and too high (Figure 2.2c). If the velocity is too low, the post-stack migration images are shallow frowns. If the velocity is correct, the images are concentrated blobs at the proper depth.

If the migration velocity is high, the images are deep smiles. These are described by data examples in Yilmaz (2002). The shallow frowns are described as under-migration, while the deeper smiles are described as over-migration.
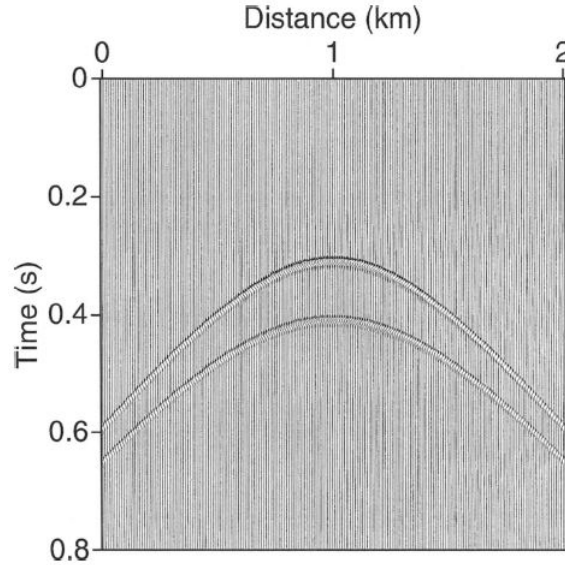


Figure 2.1: Synthetic zero-offset seismograms of two point diffractors. The diffractors are at depths of 600 and 800 m, respectively, in the middle of the model(Lines et al., 1998)

Let us examine the effect of different velocity on pre-stack common image gathers (CIGs). Given a diffractor P on the vertical axis of a Cartesian system, now assume there is a source at S and a receiver at R on the earth's surface, with x-coordinates of $x_s$ and $x_r$ , respectively (see Figure 2.3). If the medium velocity is v, the total traveltime from the source S to the diffractor P and back up to the receiver R can thus be given by the so-called double square root relationship (Claerbout, 1985),

$$t = \frac{1}{v}(\sqrt{x_s^2 + z^2} + \sqrt{x_r^2 + z^2}).$$ (2.9)

In contrast with post-stack migration, for the common image gathers (CIGs) produced in the pre-stack depth migration, as shown in Figure 2.4, a low velocity produced shallow
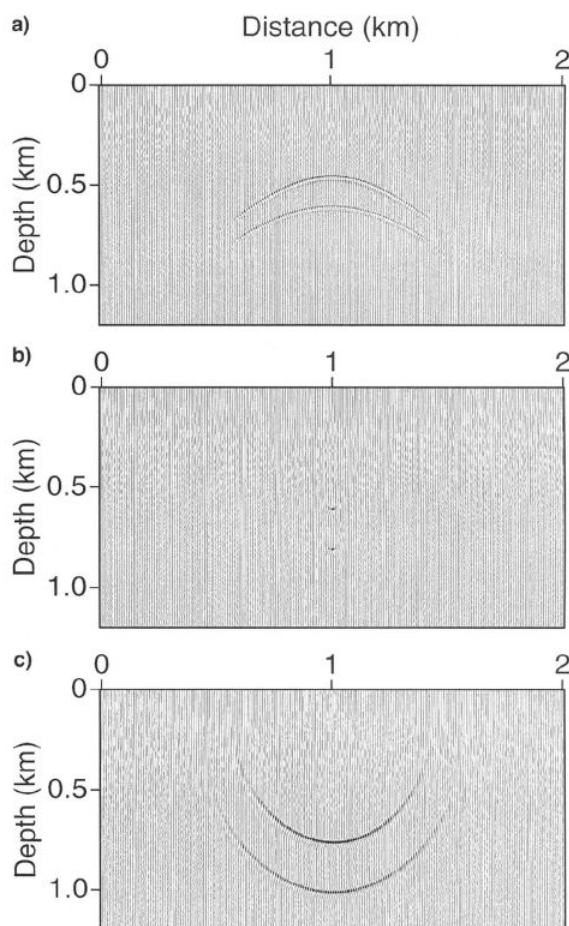
Figure 2.2: post-stack migration of a model with two point diffractors. (a) A smaller migration velocity produces shallow frowns. (b) The true velocity collapses the hyperbola to concentrated blobs. (c) A larger migration velocity results in deep smiles(Lines et al., 1998).
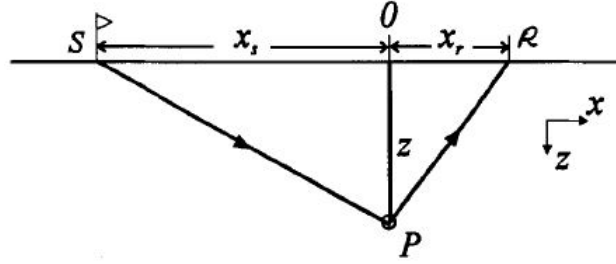
Figure 2.3: The non-zero-offset (pre-stack) geometry for a point diffractor at P (Lines et al., 1998)

smiles, while a higher velocity results in deeper frowns. When the migration velocity is correct, the CIGs produce horizontal segments at the exact diffractor depths, and well focused images on the stack section. Typically, the curvatures of the shallow smiles/frowns are larger than the deep ones. This indicates that velocity errors are more pronounced on shallow reflections and thus are easier to correct. This also agrees with the general observation that sufficient offset/depth ratio is needed to analyze velocity errors (Lines et al.,1998).

## 2.1.7   Velocity depth ambiguity

Lines (1993) gave a simple and vivid description of this well-known velocity / depth ambiguity, which has a limiting effect on all velocity estimation methods. Factors that control the occurrence of velocity-depth ambiguities include the effective width of a potential velocity anomaly; i.e., its spatial wavelength, its height above a reflector, and its thickness. A factor that does not affect velocity-depth ambiguities is the magnitude of the anomaly (the difference in velocity between it and the background). Velocity analysis generally involves analysis of traveltime moveout of seismic events. Lines (1993) showed that the velocity- depth ambiguity is dependent on offset / depth ratio and on the accuracy of traveltime picks. To analyze the velocity-depth ambiguity problem in reflection
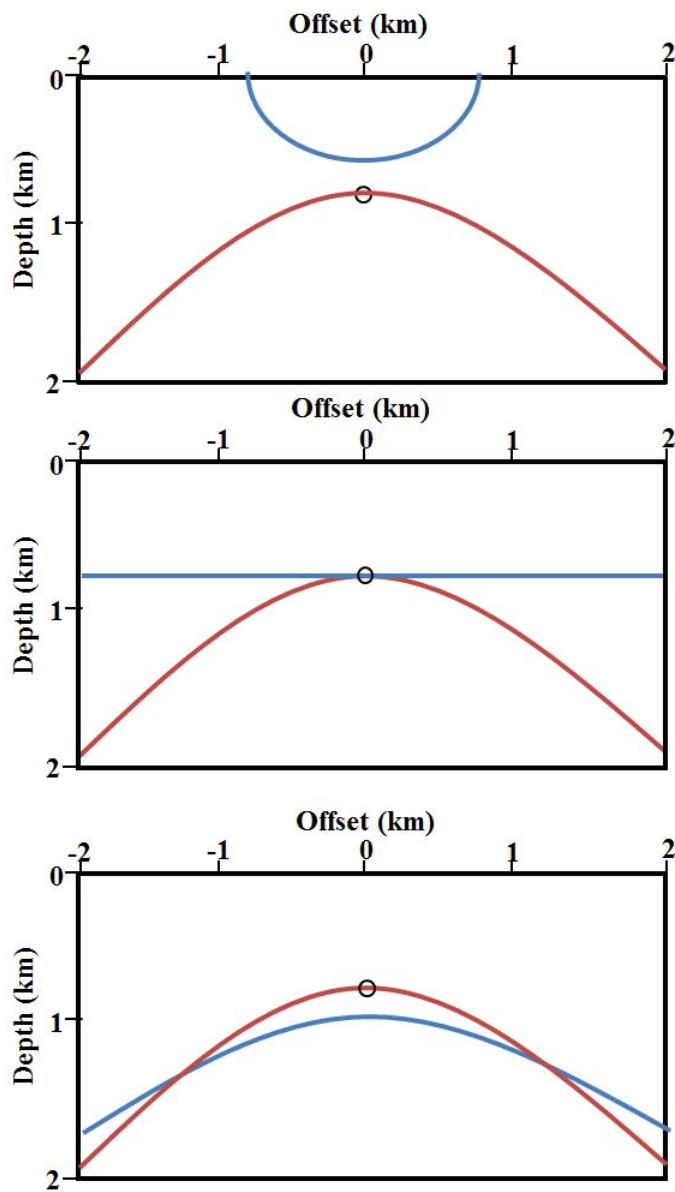
Figure 2.4: CIGs when different migration velocities are used. Migration velocity is smaller(a), equal(b), and larger(c) than the correct velocity, respectively. The offset is the distance between source and receiver (s-r).The circle in cyan represents the diffractor position. The red is the diffraction response before migration and the blue is after migration (Lines et al., 1998).

tomography, we consider a reflection layer with thickness z and velocity v as shown in Figure 2.5. The reflection traveltime equation for a source - receiver distance x is given by
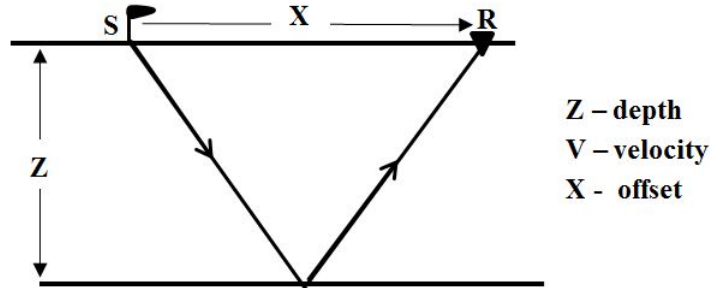


Figure 2.5: A geometry for a single reflector, where z = depth, v = velocity and x = offset (Lines, 1993).

$$t = \sqrt{\frac{(2z)^2 + x^2}{v}}. \tag{2.10}$$

When x is zero, there is no traveltime change if the fractional depth change is equal to the fractional velocity change; that means the model is completely ambiguous. Consider two models that are equivalent for the zero offset case. That is, let the vertical traveltime be t0 and consider two models whose depths and velocities are given by $(z, v)$, $(z + \Delta z, v + \Delta v)$ such that

$$\frac{2z}{v} = \frac{2(z + \Delta z)}{v + \Delta v} = t_0. \tag{2.11}$$

These two models are indistinguishable for velocity analysis at zero offset and remain indistinguishable at an offset x if their time difference is less than an expected picking error $t_\epsilon$. This is an ambiguity condition:

$$\sqrt{1 + \frac{x^2}{v^2 t_0^2}} - \sqrt{1 + \frac{x^2}{(v + \delta v)^2 t_0^2}} < \frac{t_\epsilon}{t_0}. \tag{2.12}$$

If we use the binomial expansion, recombine terms, and ignore higher order terms, we can rewrite the previous ambiguity condition in equation (2.12) as:

$$\frac{x^2}{v^2 t_0^2} \frac{|\delta v|}{v} < \frac{t_\epsilon}{t_0}. \tag{2.13}$$

This result states that our problem is ambiguous for fractional velocity variations such that:

$$\frac{|\delta v|}{v} = \frac{v^2 t_0^2}{x^2} \frac{t_\epsilon}{t_0}. \tag{2.14}$$

Hence, ambiguity in velocity is dependent on the product of two factors: 1) The fractional error in traveltime picking given by $\frac{t_\epsilon}{t_0}$. 2) The square of the ratio of 2* depth/offset. Therefore, to reduce the ambiguity for a given reflector at depth z, we need to increase the offset of the recording spread and reduce picking errors (Lines, 1993). In practice, the data were already acquired with a fixed maximum offset. So, when depth-offset ratio is too large, the residual moveout is not sensitive to the velocity any more. This is true for stacking velocity analysis and for all forms of migration velocity analysis.

### 2.1.8   Sensitivity to the interval velocity model

Velocity smoothing is required by Kirchhoff depth migration which relies on ray theory. This is because that ray theory is derived with a high frequency approximation. In order to achieve traveltimes from ray theory that agree with real waves, the medium must be smooth over a distance equal to the wavelength at the dominant frequency. Kirchhoff migration is sensitive to ray traveltimes, which depend on the amount of smoothing applied to the velocity model before the ray-tracing is performed (Gray, 1998). How much should the velocity be smoothed? On the one hand, smoothing the velocity model is inherently undesirable because it removes detail that was introduced for some reasons, perhaps geological. On the other hand, velocity smoothing, though unnecessary for non-ray-based migration, is usually a reasonable thing to do before any depth migra-

tion, since we typically lack precise, detailed knowledge of the velocities inside the Earth (Gray, 1998). Versteeg (1993) pointed out, using the structurally complex Marmousi model, that applying a moderate amount of smoothing to the velocities does not usually cause a wave-equation migrated image to be degraded, and the same is true for Kirchhoff migration. Gray (1998) studied three different velocity models, which included a Canadian Foothills data set, a line from the SEG/EAGE salt model (OBrien and Gray, 1996), and the popular Marmousi data set. These models illustrate a variety of geologic styles, with structural complexity ranging from mild to extreme. The same Kirchhoff migration program was used to migrate all the data sets, using velocity models that were variously smoothed versions of the exact velocities. Gray (1998) concluded from the three model studies that too little (less than one wavelength) smoothing produced a better image than too much (bigger than three wavelengths) smoothing. Too little velocity smoothing, while violating the mathematical assumptions that make ray theory valid, doesn't appreciably change the velocity model.

Too much smoothing changes the velocity model substantially, in the worst case removing all geologic plausibility. We are thus encouraged to apply less, rather than more, smoothing to any velocity model before depth migration (Young et al., 1999).

2.1.9 Addressing the instabilities of pre-stack velocity analysis

Sometimes it is difficult to achieve a high-resolution velocity analysis with the use of seismic traveltime data alone because of intrinsic problems for the velocity analysis: the ambiguity between velocity and reflector depth, artifacts from starting model inaccuracies, and the velocity distortion obtained by using the limited available range of ray angles, among others. These are inherent problems that can only be addressed by incorporating information other than seismic traveltimes into the velocity analysis. Stork and Clayton (1997) demonstrated that numerous methods for constraining the velocity

analysis are effective at resolving some of the problems of velocity analysis. The resolution of reflector depth is improved by incorporating borehole velocities, restricting the location of the velocity variations, and setting a maximum limit on velocity. The vertical smearing from the limited angular ray coverage is reduced by implementing a minimum entropy penalty function, constraining velocity variations to certain depths, and setting limits on the velocity. They also point out that the interpretor's geologic constraints will be useful when sufficient constraints are not immediately apparent for adequately removing the inherent artifacts of generalized pre-stack velocity analysis. As a result, the interpreter should consider a variety of constraints as he/she develops a velocity model that is both geologically reasonable and consistent with the data. While the inversions may repeatedly have significant artifacts, an interpreter may recognize a trend and help guide the process to some likely possibilities. The pre-stack velocity analysis approach with flexible constraints can be thought of as an iterative interpretation process that the explorationist can use to build a model that is both consistent with the pre-stack data and geologically reasonable.

## 2.1.10   Limitations of seismic methods

A key guideline for evaluating the plausibility of the structure presented by the depth image is the time-depth rule. All comparisons between time and depth images should be consistent with a rule that is a principal basis for evaluating depth imaging results. This rule is that the expression of structure should never be more complex in depth than it is in time (Fagin, 1999). This simple rule is very useful to make a good judgment for the rationality of the velocity model. Velocity measurements are always dependent on the moveout contrast created by different interval velocities. Increasing offset and decreasing depth are associated with increasing moveout contrast for a given velocity. Therefore, in principle, resolution increases with increasing offset/depth ratios. (But not always in

| Data Set | Analysis method | Dip | raypath bending | Short-spaced Velocity changes | Anisotropy | Resolution Limits |
|---|---|---|---|---|---|---|
| CIG | Tomography calibrated to wells for anisotropy | | | | | √ |
| CIG | Tomography | | | | √ | √ |
| CIG | One dimensional | | | √ | √ | √ |
| CMP | Model based | | | √ | √ | √ |
| CMP | Dip-corrected stacking velocity | | √ | √ | √ | √ |
| CMP | Stacking velocity | √ | √ | √ | √ | √ |

Table 2.1: Sources of error for seismic velocity estimation methods. Short-spaced velocity changes refer to velocity bodies smaller than a spread length.(Fagin, 1999)

practice, since poor spatial sampling can limit the range of offsets that migration can use). Alternatively, moveout contrast declines with layer thickness. For a fixed spread length this translates into a limitation on the thickness of a velocity layer which is seismically resolvable, typically on the order of 100-300ms. The velocity information obtained from seismic data depends on the data state and the type of analysis performed. Table (2.1) (Fagin, 1999) lists the potential error sources of various data states and data analysis. The velocity methods are designated in the first two columns from stacking velocity to tomography calibrated to wells. The various geological and geophysical phenomenon are dip, raypath bending, short-spaced velocity changes (shorter than a spread length) and anisotropy. The information content from a velocity method is dependent on the data state and the type of analysis method. The Stacking velocities at bottom of the table, which involves Dix transformation, suffers errors from all the listed phenomenon; this is because the Dix equation assumes nearly straight raypaths, flat beds, an absence of CMP smear, and symmetric raypaths (Fagin, 1999). Tomography calibrated to wells at top of the table suffers from only resolution limitations. Dip, raypath-bending, and anisotropy all cause a bias in seismic error. The typical bias is for the seismic velocity estimates to be too high. A resolution limitation should be an unbiased error (Fagin, 1999). Lower-effort methods are affected by structural dip, ray-bending, short-spaced velocity changes, and anisotropy. We notice that only tomography calibrated to wells does not suffer from anisotropy limitations.

## 2.2   General velocity model building procedure for marine data

Many techniques are available for building velocity models for depth imaging, and a virtually unlimited number of velocity models and images can result from them. However, only one technique might be appropriate as a geological solution. In many cases

the layered model building approach gives the best match between the true geological solution, velocity analysis, and imaging results, as in the Canadian Foothills area. On the other hand, in the East coast of Canada and Gulf of Mexico the velocities are mainly depth dependent as a consequence of compaction, rather than represented by geologic layers. Even so, not all units in the Gulf of Mexico have depth - dependent velocity behavior. The water column and salt body formations have distinct and relatively invariant velocities. Therefore, efficient model building in this setting requires a hybrid approach. Grid based techniques are used to represent velocity changes within the sedimentary section. Layer based techniques are used to portray the velocities of water column and salt bodies (Egozi, 1999).

The general velocity model building procedure for typical marine data is as follows:

1) Build the velocity in the water layer. 2) Build the initial sedimentary velocity using vertical update method 3) Update the velocity using tomography 4) Update the velocity in deep section using velocity scans

### 2.2.0.1 Build the velocity in the water layer

Data processed in this thesis were acquired in East Coast of Canada. For marine data, the first step in the flow was to determine velocity in the water layer. The water depth in this area is approximately 2400 to 3100 meters. A range of water velocities from around 1460 m/s to 1520 m/s were tested through water flood migrations and final depth variant water velocity function was chosen based on the flatness of the water bottom events in the common image gathers (CIGs). The water bottom was then interpreted on the water flood migration volume.

### 2.2.0.2 Vertical update for velocity

For the gently dipping sedimentary section, the Dix transformation (Dix, 1955) of stacking velocity to interval velocity is often adequate to obtain a sufficiently accurate

initial velocity model. This method is called vertical update. It is assumed in this procedure that the velocity-depth profile within the sedimentary section varies only slightly over the extent of the seismic line. Therefore, there have not been any attempts at mapping lateral variation in the sedimentary section from Dix interval velocities. The vertical update is one-dimensional in the sense that each gather location is analyzed and updated without consideration of the residual moveout or the existing velocity model in neighboring gather locations. This correction technique is outlined by Deregowski (1990). The key step in the method is a semblance analysis of the depth migrated gathers along predicted curves which are associated with different fractional changes in $v_{rms}$ values. When these semblance clouds are picked, each surface has a new $v_{rms}$ associated with it. New interval velocities, for each layer, can be derived by the use of the Dix formula and a new velocity model can be constructed (Fagin, 1999). Usually these analysis are performed along a horizon. The advantage in working along horizons is that the user can avoid picking high frequency lateral variations. Normal procedures to build horizons is to pick the water bottom horizon first, then duplicate these horizons for different depths ( "phantom horizons"). When the water bottom and subsurface structures are too complicated, water bottom hung horizons can not adequately represent the subsurface geology; therefore, a different horizon approach needs to be found. The one-dimensional technique works well for long wavelength velocity variations. In particular they should not have a significant spatial wavelength shorter than a spread length. One key use for the vertical updated velocity picking stage is to pick the major trend for the velocity model. The weakness for vertical updating is its inability to correctly update the model in the presence of short-wavelength lateral velocity variations in the overburden; thus there is a need for a technique that considers changes in arrival time in association with lateral variations in the overburden. If the width of a velocity variation is less than a spread length, a vertically-updated correction may be in the wrong direction. For example, as shown in

Figure 2.7 the near offset seismic energy might propagate through a low velocity region and the far offset energy through a high velocity region. On a migrated gather, velocity analysis will predict that the velocity is too high, but on the stack it looks like velocity is too low. This dilemma shows the weakness of the vertical updating in one-dimensional velocity analysis. Errors in one-dimensional velocity analysis can make it difficult for the following global tomography to converge.
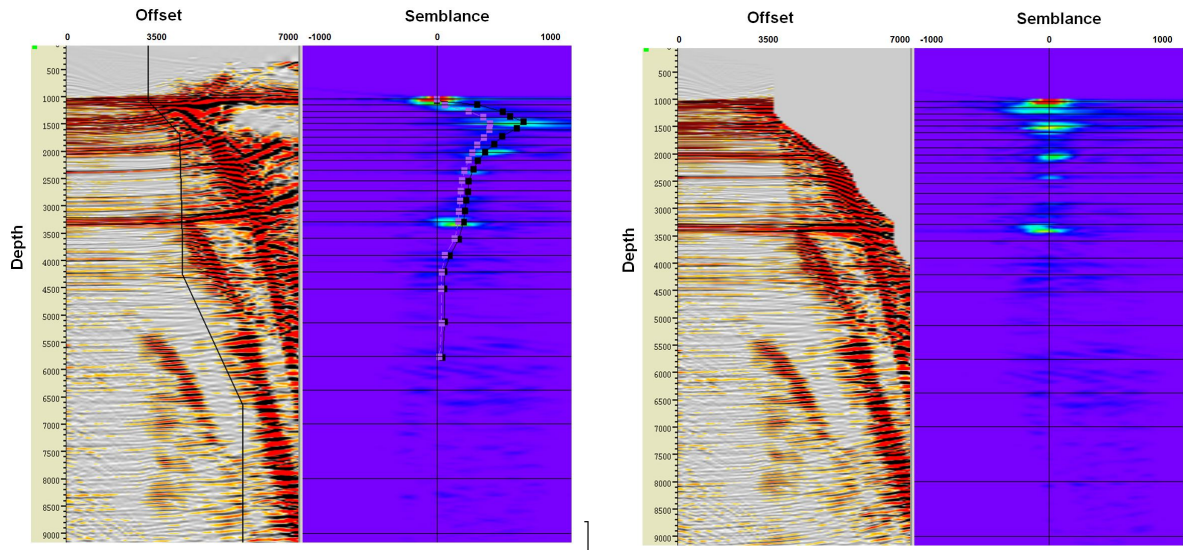


(a) Semblance of CIGs before vertical update      (b) Semblance of CIGs after vertical update

Figure 2.6: Semblance analysis of CIGs for vertical velocity update. (a) shows the NMO corrected CIG with original velocity on the left panel, the right panel is amplitude semblance calculated which are associated with different fractional changes in $v_{rms}$ values (CGG, 2010), it is clear that the maximum semblance amplitude is away from center which means current velocity was not the best. (b) shows that the event on CIG becomes flat with new picked velocity, and maximum semblance amplitude obtained by the new velocity is centered.
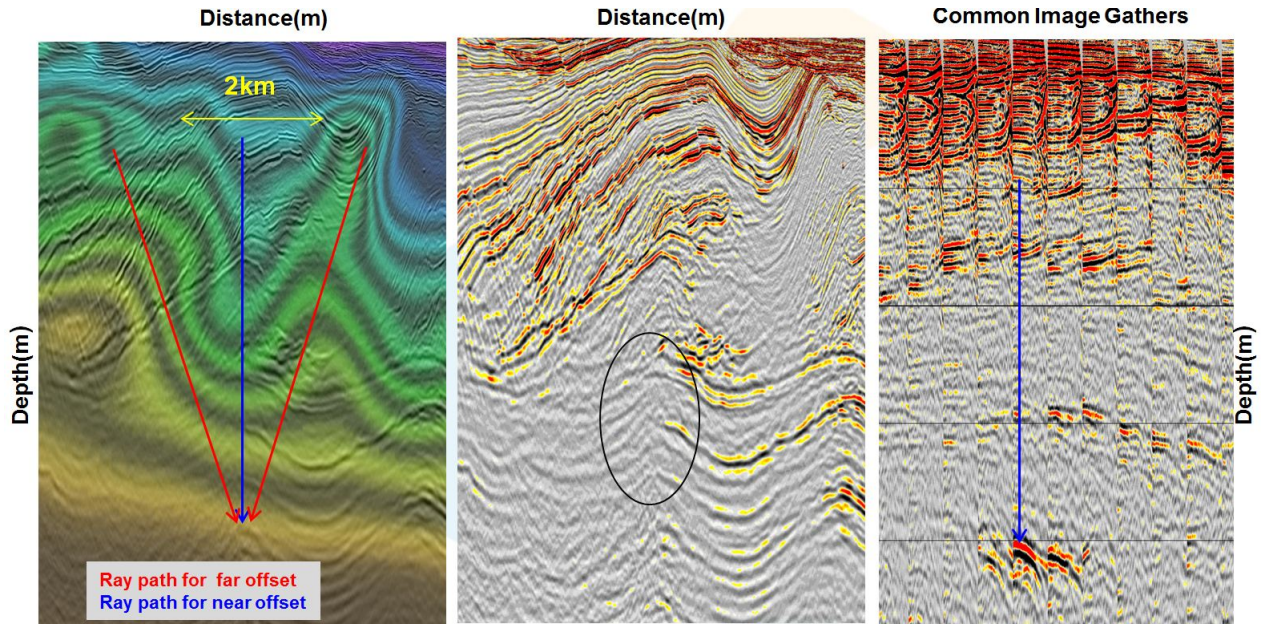
Figure 2.7: Weakness for vertical updating. The left panel shows the velocity superimposed on stack; The middle panel redisplays the stack underneath the velocity model on the left panel; and the right panel is the corresponding CIGs at specified location. At the location indicated by blue arrow, the near offset seismic energy propagate through a low velocity region along the raypath in blue and the far offset energy through a high velocity region along the raypath in red. The width of this velocity variation is 2km, which is less than a spread length of 6km. The suspicious anticline in circled area on the stack indicates the velocity is too low, while the CIGs shows that the velocity is too high (CGGVeritas, 2010).

2.2.0.3   Tomographic velocity analysis

As shown in Figure 2.9, the velocity model built from the vertical update stage reflects the general trend of subsurface velocity . To image the subsurface more accurately, an accurate velocity is required. Tomography analysis serves to provide an accurate velocity model in areas of complex geology, where vertical updating methods fail.

Tomography can fall into two categories: traveltime tomography and depth gather tomography. These two methods are based on the simple rule: when the velocity is correct, there will be no time or depth discrepancy. A satisfactory model will predict traveltimes that agree with observed traveltimes ( traveltime tomography), or it will yield a depth migration sections with no residual moveout on CIG's, which is residual curvature analysis (RCA) (Zhou et al, 2003). The tomography analysis conducted in this thesis is residual curvature analysis ( RCA ).

RCA is applied on depth migrated CIGs. A standard flow for tomography velocity analysis is described in Figure 2.8. Starting from an initial velocity model, RCA uses the depth error picked from CIGs and structural dip picked on migrated stack as input. The first part of RCA will do modeling through ray-tracing to generate a system of linear equations. By using ray tracing to understand and exploit the fact that potential sites of velocity error may exist away from the gather location where the residual moveout is observed, RCA projects the residual depth errors back along the traced raypaths. The second part of RCA will do inversion to derive the updated velocity model by solving the linear equations, and it calculates the velocity updates by minimizing the depth errors in offset domain common image gathers. Guo et al (2002) present an implementation of 3D gridded tomography. In their paper, they present the solution on how to reduce the effects of null space and pick errors, and how to improve the stability and efficiency in the solver.

The high quality residual moveout picks from CIGs are crucial for tomography to

make the inversion stable and convergent. An automatic scheme is used to pick residual curvature on CIGs and the structure dips on migrated stacked volume. Picking criteria such as reflector coherency, minimum spacing between picked events, and average semblance and amplitude level of CIGs are adjusted to ensure that only reliable events are picked.

In production, a hybrid approach of tomography is often used for velocity updating. We perform both global tomography and layer-constrained tomography as the data requires in different areas. The tomography is referred to as " global" because all layers can be evaluated at once. Global tomography can distribute uncertainty in an optimal way through the model. Layer-constrained tomography is used in areas where there is a need to incorporate the geological structures to make the velocity model represent the distinct geological layers better, e.g, for the water layer and some unconformities. Normally several iterations of tomographic velocity analysis need to be performed in order to achieve the objective of yielding flat pre-stack depth migrated CIGs by using the refined interval velocity model.

### 2.2.0.4  Velocity scan

As described in previous section, when offset/depth ratio is less than 1, reflection angles are limited, and velocity-depth ambiguities occur. Velocity scans are conducted in areas where there is insufficient moveout differentiation at different offsets for vertical updating or tomography velocity analysis to work. Starting from 100 percent of velocity picked from the other methods, a different percentage of velocity is generated with an increment of 2 or 5 percent step on each side of central velocity. The best velocity will be the velocity which generates the best images with strong amplitude and better continuity.

In the velocity model building process, a good velocity model should meet the following criteria: 1) acceptable degree of flatness of the common image gathers 2) a well-
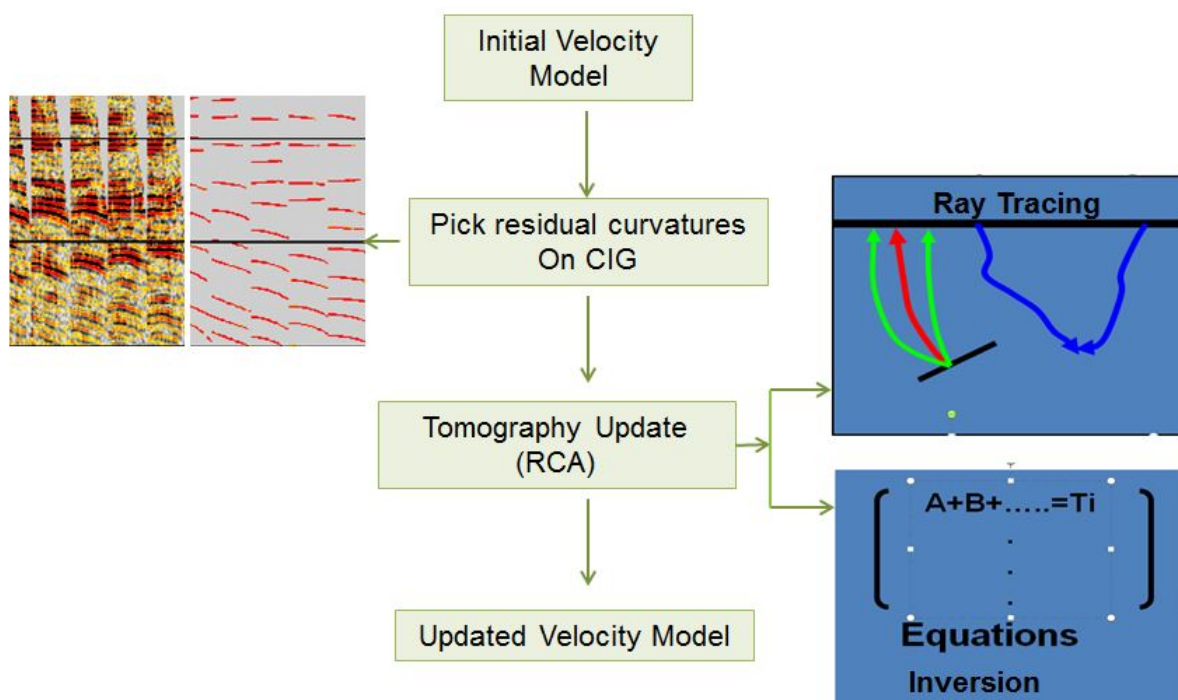
Figure 2.8: Tomography update procedure (CGGVeritas, 2010)
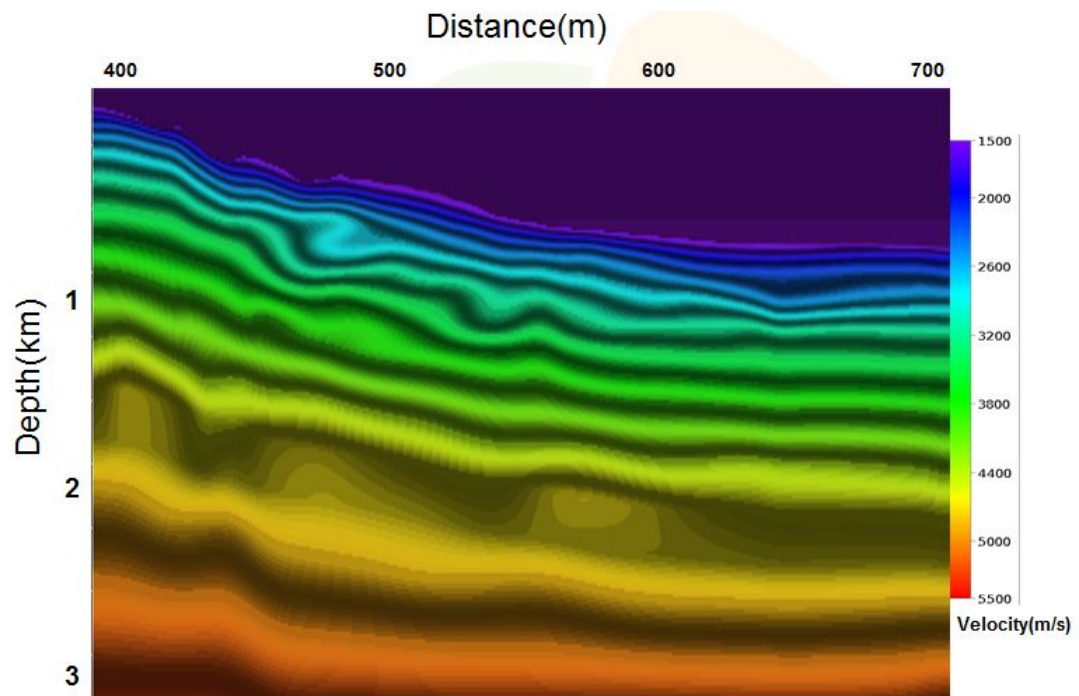
Figure 2.9: A velocity model after vertical update (CGGVeritas, 2010) which resolves the long wavelength trend of subsurface velocity.
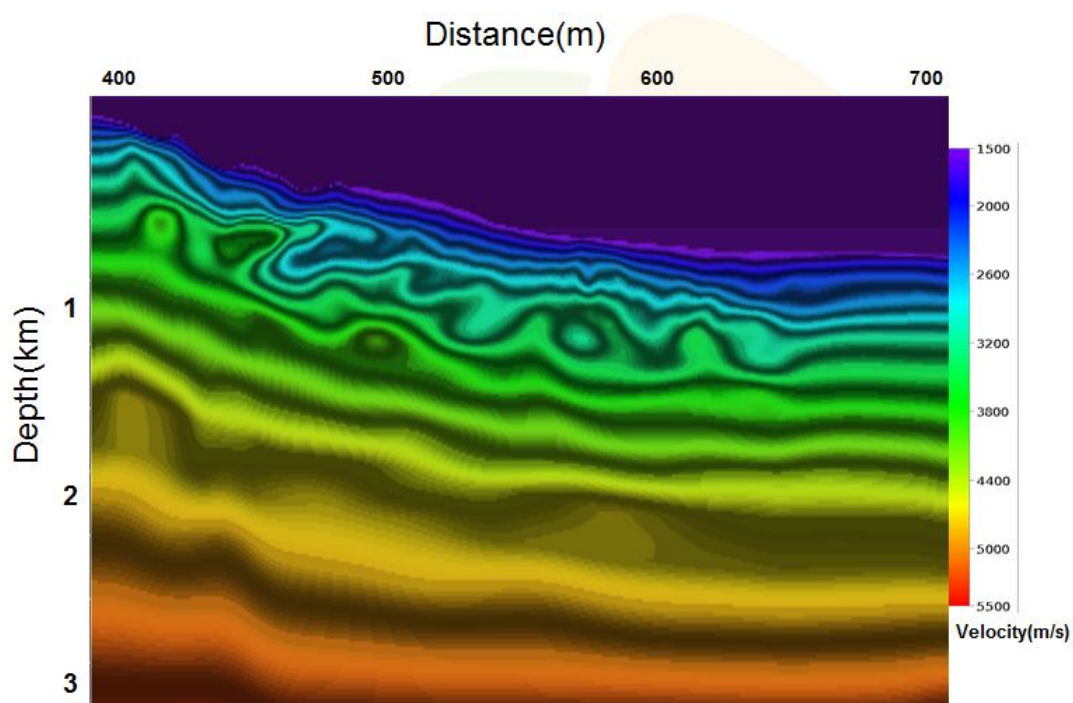
Figure 2.10: A velocity model of Figure 2.9 after global tomography (CGGVeritas, 2010) which adds more short wavelength detail to the velocity model.

focused image 3) geologically plausible structure.

## 2.3  Anisotropy

Anisotropy of a medium refers to the variation in seismic velocity that occurs with the direction of propagation within the medium. There are several possible origins of anisotropy. First, anisotropy exists intrinsically in sedimentary sequences because of preferred orientation of anisotropic mineral grains or the shapes of isotropic minerals; as described in Figure 2.11. Second, thin bedding of isotropic layers on a scale small compared to the wavelength can cause apparent anisotropy (the layers may be horizontal or tilted) as described in Figure 2.12; Third, Figure 2.13 shows that vertical or dipping fractures or micro-cracks can also cause apparent anisotropy (Thomsen, 1986). Anisotropy has a big influence on conventional seismic processing. One of the most common anisotropy-related phenomena is that of misties in time-to-depth conversion. Another complication in conventional processing caused by anisotropy is an increased magnitude of non-hyperbolic moveout. On conventional-length spreads, close to reflector depth, P-wave moveout in unstructured VTI ( Vertical Transverse Isotropy ) media does not usually deviate much from a hyperbola parametrized by the NMO velocity. At larger offsets, however, velocity variation with angle makes the moveout increasingly non-hyperbolic; the magnitude of the non-hyperbolic moveout depends on the value of parameter '$\eta$' described. Furthermore, dipping reflectors are mispositioned laterally, and diffractions are not completely collapsed, leaving diffraction tails at corners.

### 2.3.1  Weak elastic anisotropy

Thomsen (1986) pointed out that in most cases of interest to geophysicists the anisotropy is weak (10-20 percent difference between the velocity in the fast direction and the velocity in the slow direction). The equations governing weak anisotropy are
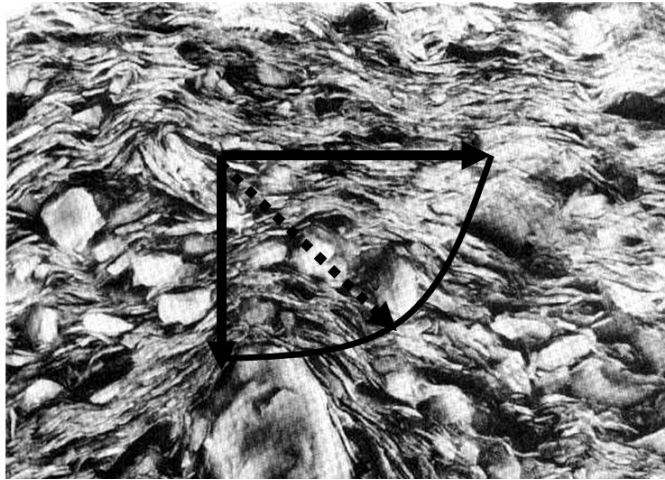
Figure 2.11: Anisotropy exists intrinsically in sedimentary sequences because of preferred orientation of anisotropic mineral grains or the shapes of isotropic minerals, the example image here is a shale sediment. The curved line is wavefront. Velocities vary with different propagating directions as indicated by arrows. The velocity along the vertical arrow is the "slow" velocity, the velocity along the horizontal arrow is the "fast" velocity (Thomsen, 2002).
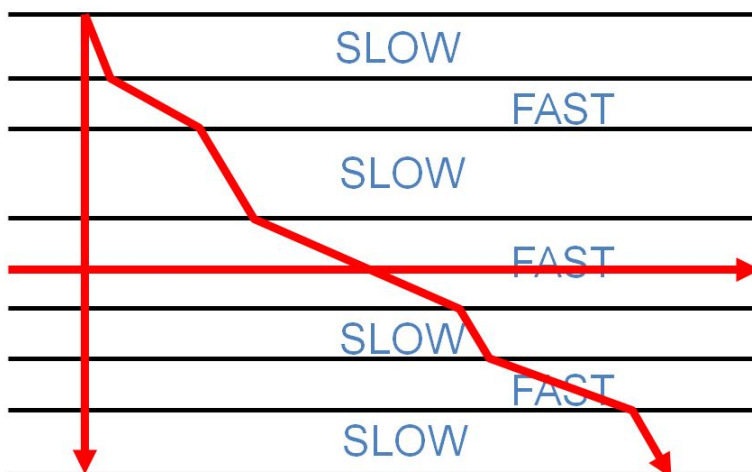
Figure 2.12: Anisotropy is caused by fine layer. The horizontal lines indicate the isotropic layers with alternating "slow" and "fast" velocity in it.The arrows in red represent different wave propagating directions. The velocity along the vertical arrow is the "slow" velocity, the velocity along the horizontal arrow is the "fast" velocity (Thomsen, 2002).
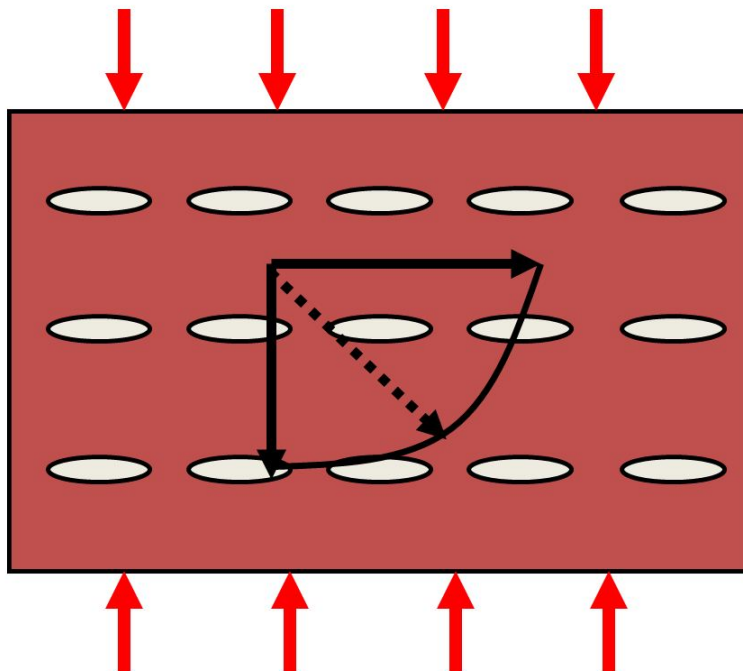
Figure 2.13: Anisotropy is caused by vertical or dipping fracture. The arrows in black represent different wave propagating directions. The velocity along the vertical arrow is the "slow" velocity, the velocity along the horizontal arrow is the "fast" velocity (Thomsen, 2002).

much simpler than those governing strong anisotropy. A brief description of anisotropy will be given here. A linearly elastic material is defined as one in which each component of stress $\sigma_{ij}$ is linearly dependent upon every component of strain $\epsilon_{kl}$ (Nye, 1957). Since each directional index may assume values of 1,2,3 (representing directions x,y,z), there are nine such relations, each involving one component of stress and nine components of strain. The nine equations may be written compactly as

$$\sigma_{ij} = \sum_{k=1}^{3}\sum_{l=1}^{3} C_{ijkl}\epsilon_{kl}, i, j = 1, 2, 3 \tag{2.15}$$

where the 3 x 3 x 3 x 3 elastic modulus tensor $C_{ijkl}$ completely characterizes the elasticity of the medium. Since both stress and strain are symmetric, we can simplify the discussion if we replace the 3 x 3 x 3 x3 tensor $\tilde{\tilde{C}}$ with a 6 x 6 matrix $\tilde{C}$, according to the Voigt scheme: (Thomsen, 1986), each index pair $ij$ was mapped into a single index $\alpha$.

$$\begin{vmatrix} ij & 11 & 22 & 33 & 23 & 13 & 12 \\ \downarrow & \downarrow & \downarrow & \downarrow & \downarrow & \downarrow & \downarrow \\ \alpha & 1 & 2 & 3 & 4 & 5 & 6 \end{vmatrix}$$

The simplest anisotropic case of broad geophysical applicability has one distinct direction (usually, but not always, vertical), while the other two directions are equivalent to each other. This case is called transverse isotropy, or hexagonal symmetry (Thomsen, 1986). The subsequent use of the term "anisotropy"in this thesis refers only to this particular case. The elastic modulus matrix has five independent components among twelve nonzero

components, giving the elastic modulus the form

$$
\begin{bmatrix}
C_{11} & (C_{11} - 2C_{66}) & C_{13} & 0 & 0 & 0 \\
(C_{11} - 2C_{66}) & C_{11} & C_{13} & 0 & 0 & 0 \\
C_{13} & C_{13} & C_{33} & 0 & 0 & 0 \\
0 & 0 & 0 & C_{44} & 0 & 0 \\
0 & 0 & 0 & 0 & C_{44} & 0 \\
0 & 0 & 0 & 0 & 0 & C_{66}
\end{bmatrix}
$$

Thomsen (1986) gave the definition for three important anisotropy parameters, the so called Thomsen's anisotropy parameters $\epsilon$, $\delta$, and $\gamma$. According to Thomsen (1986), these three parameters are appropriate combinations for elastic moduli which (1) simplify the relationships between phase velocity and elastic moduli; (2) are non-dimensional; (3) reduce to zero in the case of isotropy.

$$
\epsilon \equiv \frac{C_{11} - C_{33}}{2C_{33}} \tag{2.16}
$$

$$
\gamma \equiv \frac{C_{66} - C_{44}}{2C_{44}} \tag{2.17}
$$

$$
\delta = \frac{(C_{13} + C_{44})^2 - (C_{33} - C_{44})^2}{2C_{33}(C_{33} - C_{44})} \tag{2.18}
$$

It is interesting to notice that the parameter $\delta$ which controls the near-vertical anisotropy is a different combination of elastic modulii, which does not include $C_{11}$ (i.e., the horizontal velocity) at all.

2.3.2   The velocities of plane waves in weak polar anisotropy

As mentioned in 2.3.1, the anisotropy discussed here refers to "transverse anisotropy", also known as "polar anisotropy". Before considering the velocities of plane waves in weak polar anisotropy, it is important to clarify the distinction between the phase (wave-front) angle $\theta$ and the group (ray) angle $\phi$. Referring to Figure 2.14, the energy travels in
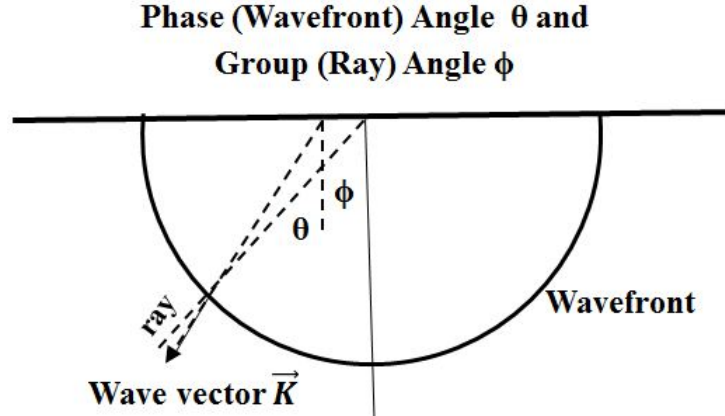
Figure 2.14: This figure graphically indicates the definitions of phase (wave-front) angle and group (ray) angle.(Thomsen, 1986)

straight lines (rays); one is shown at polar angle $\phi_{ray}$. But, it is obvious that the plane waves that make up the wave-front at this position must be traveling in the direction of the wave-front normal, i.e., at angle $\theta_{wavefront}$. So, the wave-front expands along the wave-front normals, but the energy travels along the rays. These are at different angles, so are necessarily at different velocities, but there must be a relationship. Complete textbooks (e.g., Tsvankin, 2000) show that the relationship between the ray velocity and the wave-front velocity is given, for polar anisotropy, by

$$V_{ray}^2 = V_{wavefront}^2 + \frac{\partial(v)}{\partial(\theta)}.$$ (2.19)

The wave-front is locally perpendicular to the propagation vector k, since k points in the direction of maximum rate of increase in phase. The phase velocity $v(\theta)$ is also called the wave-front velocity, since it measures the velocity of advance of the wave-front along $k(\theta)$. Since the wave-front is non-spherical, it is clear that $\theta$ ( also called the wave-front - normal angle) is different form $\phi$, the ray angle from the source point to the wave-front. The velocity we use in the processing refers to the phase velocity.

The P wave phase velocity that is valid for weak anisotropy is (Thomsen, 1986)

$$V_p(\theta) = V_{p0}(1 + \delta \sin^2 \theta \cos^2 \theta + \epsilon \sin^4 \theta), \qquad (2.20)$$

and

$$V_p(\frac{\pi}{2}) = V_{p0}(1 + \epsilon), \qquad (2.21)$$

where $V_{p0}$ is P wave vertical velocity. From equation (2.21), we infer that;

$$\epsilon = \frac{V_p(\frac{\pi}{2}) - V_{p0}}{V_{p0}}. \qquad (2.22)$$

In fact, the fractional difference between vertical and horizontal P velocities is usually referred to as the anisotropy of a rock. Thomsen's equations show that, for weakly anisotropic media and near-vertical P-wave propagation, the $\delta$ contribution completely dominates the $\epsilon$ contribution. Because of this, $\delta$ (rather than $\epsilon$) controls the anisotropic features of most situations in exploration geophysics, including the relationships among ray angles, wave-front angles, and polarization angles, and the moveout velocity for P -waves. Figures 2.15 and 2.16 show P wave-fronts radiating from a point source into two uniform half-spaces, each with positive $\epsilon$ but different values of $\delta$, one positive and one negative. It is clear from the figures that quite complicated wave-fronts may occur. For P waves weak anisotropy, the NMO velocity for short-spread $V_{NMO}$ is (Thomsen, 1986)

$$V_{NMO}(p) = V_{p0}\sqrt{1 + 2\delta}. \qquad (2.23)$$

The normal moveout velocity is independent of $\epsilon$. The value of this velocity is indicated in Figures 2.15 and 2.16 by a short arc below the origin. This line represents a segment of that "wave-front" which would be inferred by an isotropic analysis of a surface reflection experiment.
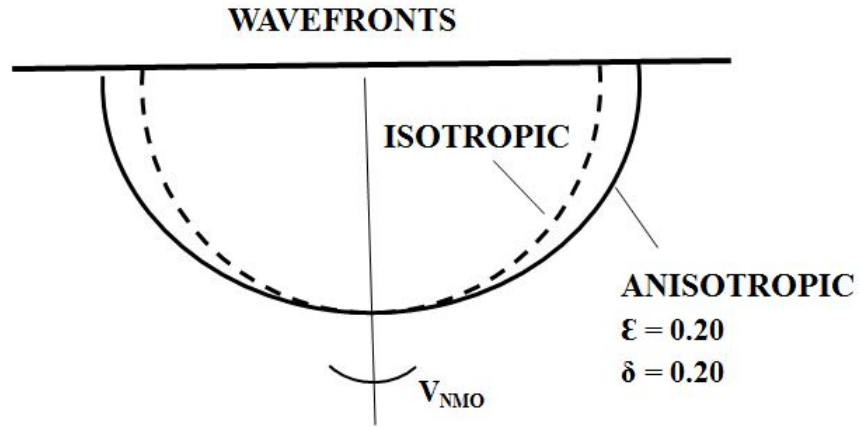
Figure 2.15: This figure indicates an elliptical wave-front ($\delta = \epsilon$). The curve marked $v_{nmo}$ is a segment of the wave-front that would be inferred from isotropic moveout analysis of reflected energy, $v_{nmo} > v_{vert}$ (Thomsen, 1986)
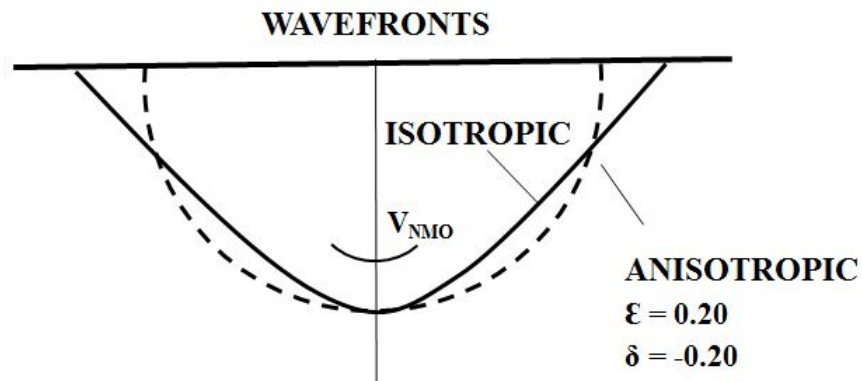


Figure 2.16: This figure indicates a plausible anisotropic wave-front ($\delta = -\epsilon$). The curve marked $v_{nmo}$ is a segment of the wave-front that would be inferred from isotropic moveout analysis of reflected energy. $v_{nmo} < v_{vert}$ since $\delta < 0$(Thomsen, 1986)

### 2.3.3   Anisotropic PSTM

Despite the general understanding of the importance of anisotropic phenomena in reflection seismology, it's more difficult to estimate the anisotropy parameters required by PSTM and PSDM. The most common type of anisotropy in sedimentary basins is (nearly ) vertical transverse isotropy, usually associated with shale formations. Alkhalifah and Tsvankin(1995) showed that all time processing in vertical transverse-anisotropic media (with arbitrary vertical variation, and anisotropy of arbitrary strength) can be accomplished using only the two imaging parameters $v_{pnmo}(0)$ and the anellipticity $\eta$. This is a nontrivial conclusion, since a casual analysis might conclude that four imaging parameters, equivalent to $C_{11}, C_{13}, C_{33}, C_{44}$ would be needed. The inversion for $\eta$ requires either the NMO velocity of a dipping event with a dip of at least 25 degree or long - spread ( non-hyperbolic) moveout:

$$\eta = 0.5(\frac{v_h^2}{v_{nmo}^2} - 1) = \frac{\epsilon - \delta}{1 + 2\delta}. \tag{2.24}$$

where short-spread NMO velocity $v_{nmo}$ for a horizontal reflector is shown in equation (2.5), $v_h$ is the horizontal velocity. Hake et al. (1984) derived a three-term Taylor series expansion for the moveout of reflections from horizontal interfaces in homogeneous VTI media. If one ignores the contribution of the vertical shear-wave velocity $v_{so}$, which is negligible (Tsvankin and Thomsen, 1994; Alkhalifah and Larner, 1994; Tsvankin, 1995), their equation can be simplified, when expressed in terms of $\eta$ and $v_{nmo}$, to

$$t^2(x) = t_0^2 + \frac{x^2}{v_{nmo}^2} - \frac{2\eta x^4}{t_0^2 v_{nmo}^4}. \tag{2.25}$$

Here, t is the total traveltime, $t_0$ is the two-way zero-offset traveltime, and x is the offset. The first two terms on the right correspond to the hyperbolic portion of the moveout, whereas the third term approximates the non-hyperbolic contribution. Note that the third term fourth order in x is proportional to the anisotropy parameter $\eta$, which therefore

controls non-hyperbolic moveout directly. In fact equation (2.25) reduces to the familiar three-term expression given by Taner and Koehler (1969) for isotropic media (equation 2.6). For equation (2.25) , the value of $\eta$ for a given $v_{nmo}$ and $t_0$ directly describes the degree of non-hyperbolic moveout in both anisotropic and isotropic layered media. In most anisotropic media, the non-hyperbolic moveout is relatively larger than that in a typical vertically heterogeneous isotropic media. Therefore, it usually is observable and measurable and thus can be used to invert for medium parameter (Alkhalifah, 1997). If the maximum offset is large enough relative to reflector depth and the resolution of the data is high, it is possible to estimate the degree of non-hyperbolic moveout attributable to anisotropy (Alkhalifah, 1997). The following gives the estimation for $\eta$

$$\eta = \frac{\Delta t^2 v_{nmo}^2 (t_0^2 v_{nmo}^2 + x^2)}{2x^2(x^2 - \Delta t^2 v_{nmo}^2)}.$$ (2.26)

To estimate $\eta$ using equation (2.26), one must first obtain $v_{nmo}$, the short-spread NMO velocity corresponding to a horizontal reflector. This velocity can be obtained using conventional velocity analysis based on a moveout spread that satisfies $x/d < 1$. Assuming that an accurate $v_{nmo}$ is obtained, then $\Delta t^2$ can be measured from the reflection moveout in the seismic data. From equation (2.23), it is clear that $v_{nmo}$ is greater than the true vertical velocity, this will result in all of the pseudo-depths being different from the true depths (Thomsen, 2002). Because anisotropic depth migration will give the correct depth and focusing, it is gradually becoming the routine procedure for seismic imaging.

### 2.3.4 Anisotropic PSDM

As mentioned in section 1.1, the velocity model used to represent anisotropic subsurface media could be VTI, TTI, orthorhombic, triclinic anisotropy. Given the geological structure presented in the 3D survey studied in this thesis, TTI pre-stack depth migration was considered to be good enough to get the best subsurface images. This thesis

will only concentrate on weak polar anisotropy TTI pre-stack depth migration. TTI stand for tilted transverse isotropy as illustrated in Figure 2.18. To better understand TTI, we start with VTI (vertical transverse isotropy). Transverse isotropic materials have physical properties which are symmetric about an axis that is normal to a plane of isotropy. As illustrated in Figure 2.17, the axis of symmetry is vertical. The velocity changes with $\theta$. Vertical velocity together with $\delta$ will control the second order moveout; vertical velocity together with $\epsilon$ will control the fourth order moveout. When sedimentary formations are laid down, this usually results in small-scale structures (thin beds, aligned flat grains) that result in vertical transverse anisotropy (Thomsen, 2002). When these beds are subsequently deformed to a first approximation they carry their symmetry with them, with the symmetry axis being locally bedding-normal, rather than vertical. In normal practice, it is assumed that there are no changes in the elasticity tensor, aside from this rotation. Except that the axis of symmetry has non-zero angle degree to the normal, TTI follows the same rule as VTI; the velocity changes with $\theta$ (Thomsen, 2002).
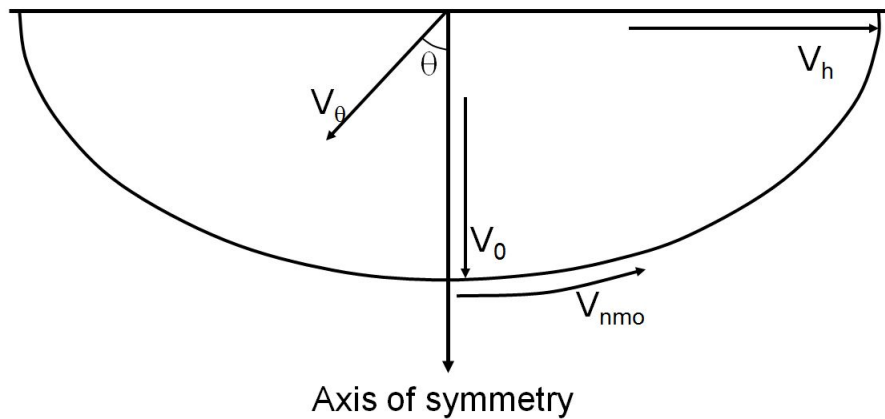


$$v(\theta) \approx v(0)\left(1 + \delta \sin^2 \theta \cos^2 \theta + \varepsilon \sin^4 \theta\right)$$

Figure 2.17: Wave-front with VTI model. VTI has a vertical axis of symmetry
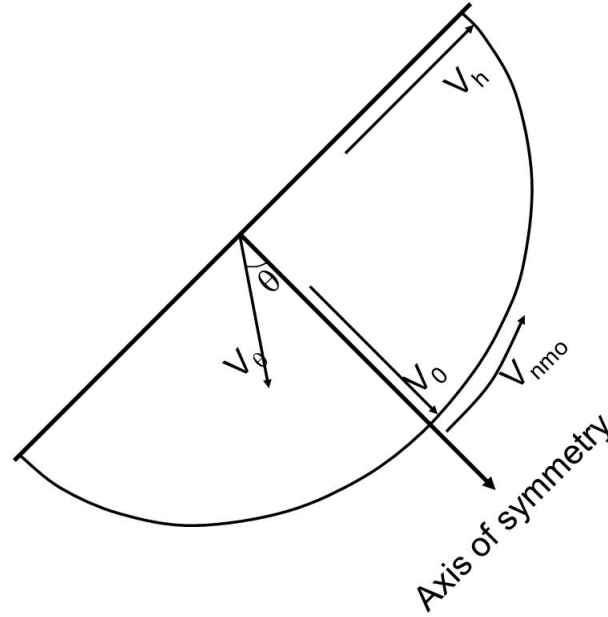
$$v(\theta) \approx v(0)\left(1 + \delta \sin^2 \theta \cos^2 \theta + \varepsilon \sin^4 \theta\right)$$

Figure 2.18: Wave-front with TTI model. TTI has a tilted axis of symmetry

Thomsen (2002) pointed out that polar anisotropy can appear as isotropy, with the unknown depth to the reflector masked inside the moveout velocity. In depth migration, we assign specific velocities to every point in the subsurface, specified in depth. If we use isotropic migration codes on anisotropic data, the velocities that flatten the common image gathers will approximate the moveout velocities discussed in equation (2.23) [i.e., $V_{PNMO(0)}$ for horizontal reflectors], and will misposition the images laterally and vertically. Figure 2.19 shows how a point diffractor would be imaged away from its true location, usually up-dip. In this context, all subsurface features are mispositioned by isotropic algorithms, with or without a reflecting plane, because of the nonspherical wavefront. This effect depends upon the difference between the wavefront angle and the ray angle, and so depends upon the anisotropy parameters. Alternatively, if we have independent information that establishes the true depths, e.g., through borehole data

(see below), then we can establish a vertical velocity function $V_{P0(z)} = z/t_0$ , where $z$ is the depth for reflector, $t_0$ is the one way traveltime from the well. Normally if we run isotropic PSDM on the data using this vertical velocity, this velocity function (which by definition does tie the wells) will not flatten the gathers as shown in Figure 2.20, and hence will produce a fuzzy image (Thomsen, 2002). Therefore, in order to achieve both correct positioning (well-tieing) and focusing, it is mandatory to perform anisotropy depth migration, in which vertical velocity is used to tie the well, anisotropy parameter to flatten the gathers.
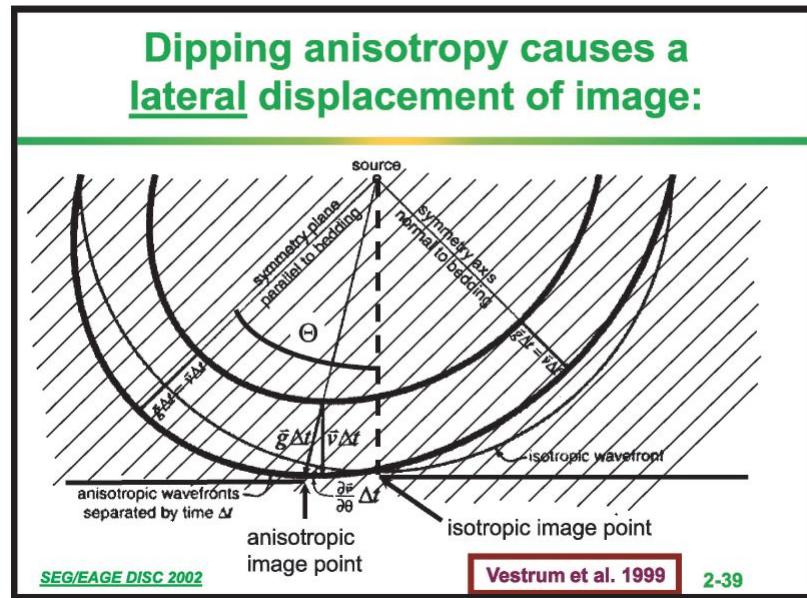


Figure 2.19: Dipping anisotropy causes a lateral displacement of image (Thomsen, 2002).

The key for successful anisotropic imaging is accurate estimation of the anisotropy parameters. One approach is to make educated assumptions based on prior geologic knowledge of the area from which appropriate values for the anisotropy parameters may be assumed. In other cases, which are the most common, the anisotropy parameters are estimated from the well data (VSP, sonic logs) and pre-stack seismic data (Alkhalifah, 1997). The first step is to obtain $V_0$ using well log information at the locations of borehole
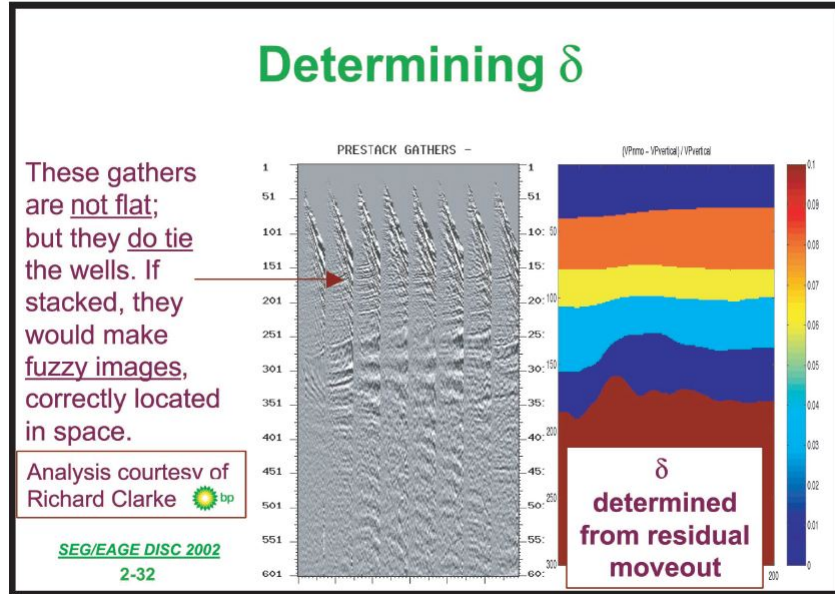
Figure 2.20: Determining $\delta$. The gathers with the correct vertical velocity will tie the well, but the events curved up, so if stacked, they would make fuzzy images. We need to run anisotropy PSDM to flatten the gathers (Thomsen, 2002).

locations, then interpolate the corresponding vertical velocity functions, and extrapolate outside. After the vertical velocity is obtained , we can invert for $\delta$ based on the residual moveout and vertical velocity by the equation below:

$$\delta = \frac{V_{p0}^2}{2V_{resdl}^2}. \tag{2.27}$$

This equation shows that obtaining the correct vertical velocity is important for inverting for correct $\delta$ value. In the case where we have well information, we can calculate from check-shots, but a lot of seismic surveys have no well information available. In this case, we need to establish a practical method to build the anisotropy velocity field. The third chapter will describe in more detail on how to get all following five parameters required by TTI pre-stack depth imaging.

$V_{p0}$    Velocity along the axis of symmetry

$\delta$    Thomsen parameter which controls near vertical velocity

$\epsilon$    Thomsen parameter which is the fractional difference between vertical and horizontal P velocities

$\theta$    Angle of axis of symmetry from vertical direction

$\phi$    Azimuthal of axis of symmetry

### 2.3.5   Summary

This chapter focused on the theory of migration velocity analysis using seismic data. Velocity plays a dual role in seismic imaging: 1) it affects the focusing of the data 2) it determines the positioning of the imaged reflectors. In the presence of complex structure, we need to leverage the power of migration to simplify and focus and simplify the data. This will enable us to reliably measure the kinematics of the reflections and converge toward accurate velocity estimates (Biondi, 2007). Pre-stack depth migration is performed to generate common image gathers (CIG). Most velocity estimation methods are based on measurements of the kinematics of the reflections on CIGs. Observation of move-out, the change in arrival time with offset in CIGs, forms the basis for estimating velocities from seismic data. Inaccurate velocity estimates will cause systematic move-out artifacts such as so-called "smiles and frowns" to appear on depth-migrated CIGs. The elimination of these move-out features by adjusting seismic velocities is the goal of migration velocity analysis; it allows depth migration to be used as a powerful velocity analysis tool. Sometimes it is difficult to achieve a high-resolution velocity analysis with the use of seismic travel-time data alone because of intrinsic problems for the velocity analysis. In addition to using surface seismic data, we can address the problem by inserting information into velocity analysis such as incorporating borehole velocities,

restricting the location of the velocity variations, setting a maximum limit on velocity, and implementing geological constraints.

The main techniques used in marine velocity model building are vertical updating and tomography analysis. The vertical velocity update is one dimensional velocity analysis which assumes no horizontal velocity variations, it is used to generate a smooth velocity model. Tomography analysis is three dimensional velocity analysis. A satisfactory model generated from tomography will predict travel-times that agree with observed travel-times ( travel-time tomography), or it will yield a depth migration sections with minimal residual move-out on CIG's (residual curvature analysis). A good velocity model should meet the following criteria: 1) acceptable degree of flatness of the common image gathers 2) a well focused image 3) geologically plausible structure.

Thomsen (1986) pointed out that in most cases of interest to geophysicists the anisotropy is weak (10-20 percent difference between the velocity in the fast direction and the velocity in the slow direction). The simplest anisotropic case of broad geophysical applicability has one distinct direction (usually, but not always, vertical), while the other two directions are equivalent to each other. This case is called transverse isotropy, or hexagonal symmetry (Thomsen, 1986). In tilted transverse isotropy (TTI), the symmetry axis is locally bedding-normal. Thomsen (1986) gave the definition for three important anisotropy parameters, the so-called Thomsen's anisotropy parameters $\epsilon$, $\delta$, and $\gamma$. The presence of anisotropy causes two principal distortions in reflection moveout. First, inaccurate vertical velocity will cause inaccurate estimations of reflector depths. Second, anisotropy leads to nonhyperbolic moveout, even in a homogeneous layer. If not properly corrected for, nonhyperbolic moveout causes distortions in velocity estimation and deteriorates the image quality. In order to achieve both correct positioning (well-ties) and focusing, it is mandatory to perform anisotropic depth migration, in which vertical velocity is used to tie the well, and anisotropy parameters are used to flatten the gathers.

# Chapter 3

# TTI pre-stack depth migration applied to a marine 3D survey

## 3.1   Introduction

This chapter presents how the migration velocity analysis techniques are applied to real seismic data. In 2011, CGG processed a frontier exploration seismic survey acquired offshore the East Coast of Canada by Statoil Canada Limited. Statoil and Repsol kindly gave the show rights for the data presented in this thesis. Both isotropic pre-stack depth migration (PSDM) and tilted transverse isotropic (TTI ) PSDM were conducted with the goals of good imaging and good velocity estimation.

Estimation of reliable anisotropy parameters is challenging, especially like the survey in this thesis where no well information is available. This paper presents a practical production method for building the five velocity fields needed for TTI PSDM: $V_{p0}$, $\varepsilon$, $\delta$, $\theta$, and $\phi$. These methods include 1D joint inversion (Huang, 2007) to estimate anisotropy parameters and high resolution tomography (Hu, 2011) to obtain accurate velocity models.

The survey in this thesis covers an area of approximately $1700 km^2$ with water depth varying from 2400m to 3100m. This 3D survey provides our client with deep water frontier exploration opportunities. The main objective is to obtain good structural positioning and imaging - focusing particularly on the complex faulting.

It is well known that sedimentary rocks possess velocity anisotropy to different degrees. Essentially all shales are seismically anisotropic. Intrinsic anisotropy is insignificant in reservoir rocks such as carbonates and massive sands. However, tight sands, shaly sands, siltsones, or thin sand-shale sequences may be seismically anisotropic. The

anisotropy may exceed 10 percent in these rocks (Wang, 2001). Seismic data will demonstrate velocity anisotropy by showing increased magnitude non-hyperbolic move-out on far offsets, known as "hockey-sticks". If seismic data from an area of anisotropy are processed using only isotropic velocity fields, images will be mispositioned in both depth and lateral location, leading to serious consequences for well placements (Byun, 1982; Isaac and Lawton, 1999; Vestrum et al., 1999; Lawton et al., 2001).

Figure 3.1 shows common image gathers (CIGs) from a PSDM using an isotropic velocity model, which was used as the initial bedding normal velocity. The CIGs indicate strong anisotropy with non-hyperbolic move-out on the far offsets ("hockey sticks") everywhere. Geological information shows the presence of shale, shaly-sand, and fractures which intrinsically cause the anisotropy. TTI pre-stack depth migration is mandatory for this area for better positioning of subsurface images vertically and laterally.
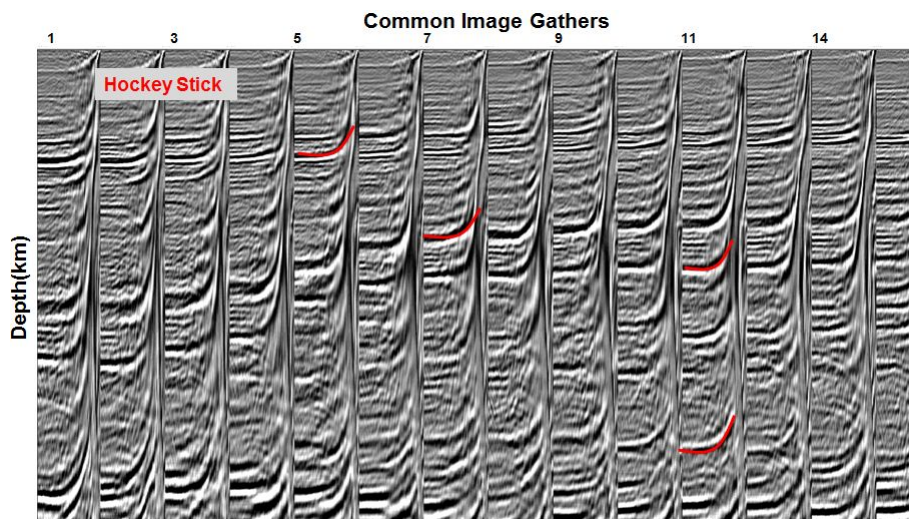


Figure 3.1: non-hyperbolic move-out known as hockey stick was present on far offsets almost for every common image gathers (CIGs).

Media with TTI exhibit polar anisotropy around a symmetry axis. When the symmetry axis is tilted (being locally bedding-normal), the medium is said to have tilted transverse isotropy (TTI). Within the plane orthogonal to the symmetry axis, the medium is

isotropic. Transverse isotropy is often described in terms of the Thomsen parameters ( Thomsen, 1986) $\delta$ and $\epsilon$. Accurately estimating anisotropy parameters is a key element in successful TTI PSDM processing.

Anisotropic (TTI) velocity model building tools and migration techniques have gained industry acceptance during recent years. Considerable research has addressed the questions of how to extract anisotropy parameters from surface seismic data, focusing primarily on the application of non-hyperbolic velocity analysis and travel-time inversion (e.g., Alkhalifah and Tsvankin, 1995; Grechka and Tsvankin, 1999; Grechka, Pech, et al., 2001) or on the analysis of joint P- and converted-wave data (Grechka, Theophanis, and Tsvankin, 1999; Grechka, Pech, and Tsvankin, 2002). Studies conducted by Isaac (Isaac,et al. 2004) and others has shown feasibility of obtaining estimates of anisotropy parameters deterministically from surface P-wave data alone. Huang et al. (2007) have presented a 1D joint inversion method to invert simultaneously for $\delta$ and $\epsilon$ . The work shown in this paper used 1D joint inversion method to estimate $\delta$ and $\epsilon$ parameters.

## 3.2   Building a TTI velocity model

TTI PSDM requires five "velocity" fields: bedding normal velocity $V_{p0}$, Thomsen parameters $\epsilon$, $\delta$, dipping angle $\theta$ of symmetry axis and azimuthal angle $\phi$ of symmetry axis . These five fields are on the same grid. A reliable TTI velocity model is crucial for successful implementation of TTI pre-stack depth migration.

Our work flow to build TTI velocity fields is

1. Start with an isotropic initial velocity.

2. Pre-stack depth migrate the data using isotropy velocity.

3. Choose a number of locations in mini-basin (as indicated by blue arrow in Figure 3.2)or with relatively gentle dip.

4. Perform 1D inversion to get estimates for $\epsilon$ and $\delta$.

5. Build the initial TTI bedding normal velocity.

6. Pick $\theta$ and $\phi$ values along coherent reflectors on migrated volume.

7. Run 3D anisotropic migration to generate CIGs for 3D tomographic velocity updating ( $V_{p0}$ only, with $\delta$ and $\epsilon$ fixed).

8. Update the TTI velocity model several (about four) times by using high resolution global tomography.

9. Conduct velocity scans for the data below the basement horizon.

### 3.2.1  Building an isotropic velocity field

To ensure the best input data possible for migration and velocity model building, we performed deterministic de-convolution, noise attenuation, and 3D surface related multiple elimination.

We started the migration sequence with isotropic PSDM on the preprocessed data. The velocity model was built using a top-down approach. The first step is to determine the water velocity function. This survey is in deep water, with the water bottom ranging from 2400m to 3100m. A range of water velocity functions was tested using v(z) "water flood" migration. The final water velocity function was chosen based on the flatness of water bottom event on migrated CIGs. The typical water velocity profile has a high velocity at very shallow depths caused by high temperature, then lower velocity at intermediate depths as the water temperature decreases, then high velocity again at great depths due to the pressure.

After obtaining the water velocity, we built a sedimentary velocity field down to the deeper section. In the process of building this velocity field, we have several criteria to

follow. First, the reflection events on common image gathers should be acceptably flat. Second, subsurface images should be well focused. Third, the velocity model should be geological plausible. We try to apply those criteria even when determining the isotropic velocity field.

The initial isotropic velocity field was built by using vertical updating. This procedure is one-dimensional in the sense that each gather location is analyzed and updated without consideration of the residual move-out or the existing velocity model at neighboring gather locations. This technique is outlined by Deregowski (1990).

One objective of vertical updating is to pick the long-wavelength trend for the velocity model. The weakness of vertical updating is its inability to update the model correctly in the presence of short-wavelength lateral velocity variations in the overlying layers. Global tomography, which considers changes in arrival time in association with a lateral variation of overlying velocity field, is needed for this.

### 3.2.2 Derive $\epsilon$ and $\delta$ using 1D joint inversion

After we obtained the isotropic velocity field, we moved on to next stage of building a complete TTI velocity field. For P wave imaging, the required anisotropic parameters are $v_0$, $\epsilon$, and $\delta$, plus dip and azimuth parameters $\theta$ and $\phi$. When the input is restricted to P wave surface seismic (no additional information), an ambiguity exists in inverting all three parameters at same time, even in 1D. Obtaining $V_{p0}$ is the first important step; then with knowledge of $V_{p0}$, it is feasible to invert for the anisotropic parameters $\epsilon$, and $\delta$ simultaneously.

When non surface seismic data (e.g., check shots) are available, we can accurately determine $V_{p0}$. However, many exploration surveys have no wells available at the beginning of their exploration period, but still have (possibly regional) evidence for seismic anisotropy. In these cases, we will choose a relatively unstructured area to derive $v_{nmo}$

(normal move out velocity ) using the near to middle offsets. Alkhalifah and Tsvankin (1995) showed that P-wave reflection move-out is largely controlled by a combination of two parameters: the NMO velocity from a horizontal reflector ($v_{nmo}$) responsible for short-spread move-out [equation (2.5)] and the anisotropic coefficient $\eta$, which determines the non hyperbolic portion of the move-out curve. In the most common case, $v_{nmo}$ can be found directly by conventional semblance analysis of horizontal events (Alkhalifah, et al. 1995). As illustrated in Figure 3.2, the CMP locations we chose for estimation of $\epsilon$, and $\delta$ are in mini basins or areas with little structural dip; at these locations, the velocity that flattens the gathers from near to middle offsets is very close to $v_0$.
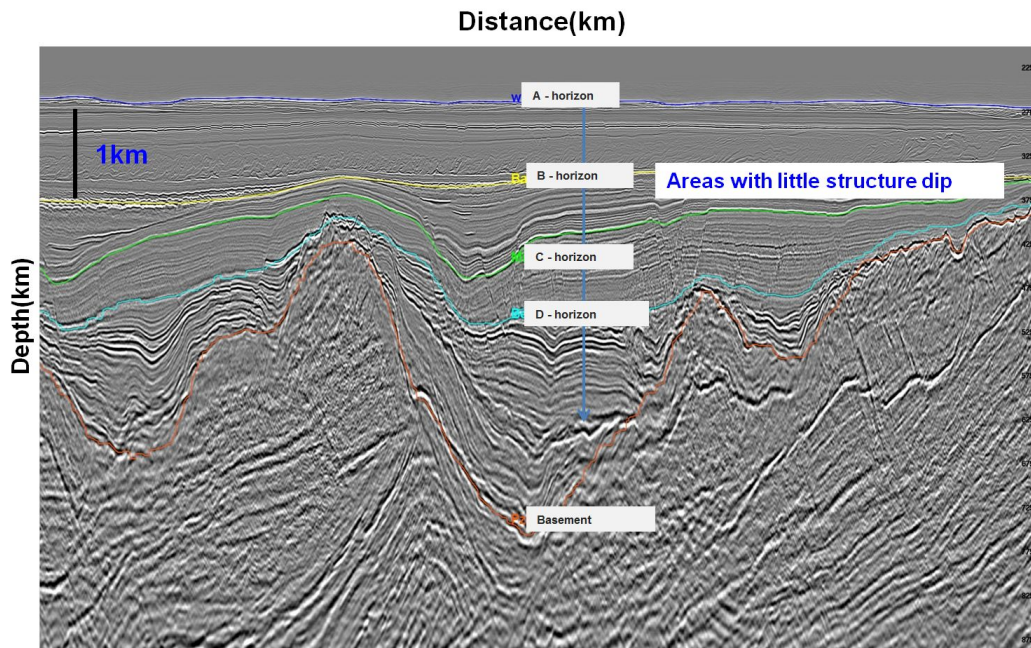


Figure 3.2: CMP locations for estimation of anisotropy parameters was chosen in areas with little structural dip

After fixing $V_{p0}$ , we migrated using Kirchhoff migration, then picked actual curvature in common image gathers(CIGs). Then we use 1D joint tomographic inversion to invert for $\epsilon$ and $\delta$ simultaneously (Huang 2007). The left side of Figure 3.3 shows CIGs that were input to curvature picking. These gathers are reasonably flat at near offsets but

curve up at far offsets ("hockey sticks"). Picking these curvatures to a maximum offset of 8250m allows us to invert reliably for $\epsilon$, and $\delta$. The right side of Figure 3.3 indicates the $\delta$ and $\epsilon$ inverted at this location with the maximum value of $\epsilon$ at 0.18. Huang et al. indicate the group direction of the ray would be:

$$\tan \theta = \frac{dx}{dz} = \frac{p_x(1 + 2\epsilon) - 2(\epsilon - \delta)p_z^2}{p_z(1 - 2(\epsilon - \delta)p_x^2)}. \tag{3.1}$$

where $p_x$ and $p_z$ are the normalized slowness components. For 1D joint tomography inversion, the shot and receiver locations are invariants. The travel time perturbation with respect to anisotropic parameters $\epsilon$, and $\delta$ was derived in a condition of keeping group direction (ray) constant. The derivatives $\left\{ \frac{\partial T}{\partial \epsilon}|_{\theta,\epsilon}, \frac{\partial T}{\partial \delta}|_{\theta,\epsilon} \right\}$ was derived for $\epsilon$ and $\delta$ joint travel time inversion with the eikonal equation and equation (3.1) used.

As illustrated in Figure 3.2, There are six key horizons interpreted by our client. From top to bottom, they are A, B, C, D, basement and bottom horizons. After we inverted $\epsilon$ at selected CMP locations in mini basins or areas with little structural dip, we averaged the values and extrapolated them to the entire survey along the six key horizons.

Finally, Figures 3.4 and 3.5 show portions of the final $\delta$ and $\epsilon$ models for this 3D survey. We use the same color bar for $\delta$ and $\epsilon$ with 0 value in purple and the value of 0.18 in red. The $\delta$ values range from 0 to 0.06. The $\epsilon$ range from 0 to 0.18. The models are overlaid on the stack, which shows consistency with compaction-driven sediments between the major horizons.

Since there is no well information available, there are uncertainties in determining the anisotropy parameters, resulting in a large amount of testing. One test was to check gather flatness and reflector depth for different ratios of $\epsilon$ to $\delta$. These ratios are important factors in our inversions. Used as constraints, they help speed up the convergence of the inversion and stabilize the solution. Figure 3.6 shows three groups of CIGs generated from three migration results with different $\delta$ values. With fixed $\epsilon$ values, Figure 3.6a
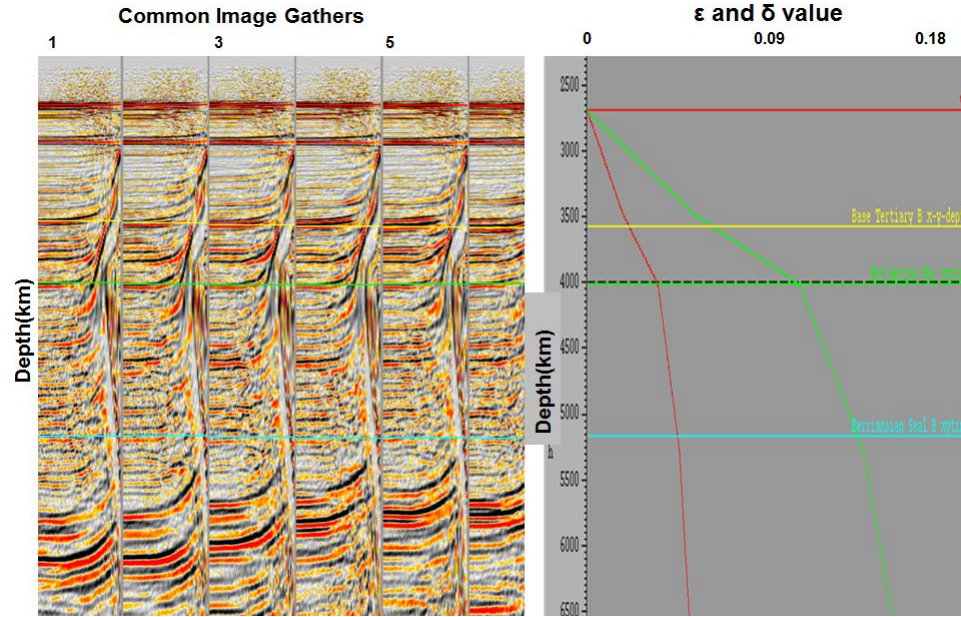
Figure 3.3: 1D joint inversion to estimate $\delta$ and $\epsilon$. The left side of the picture are the CIGs input for curvature picking, which will be used for 1d joint inversion. The right side of the picture shows the inverted $\delta$ and $\epsilon$ values at this location.
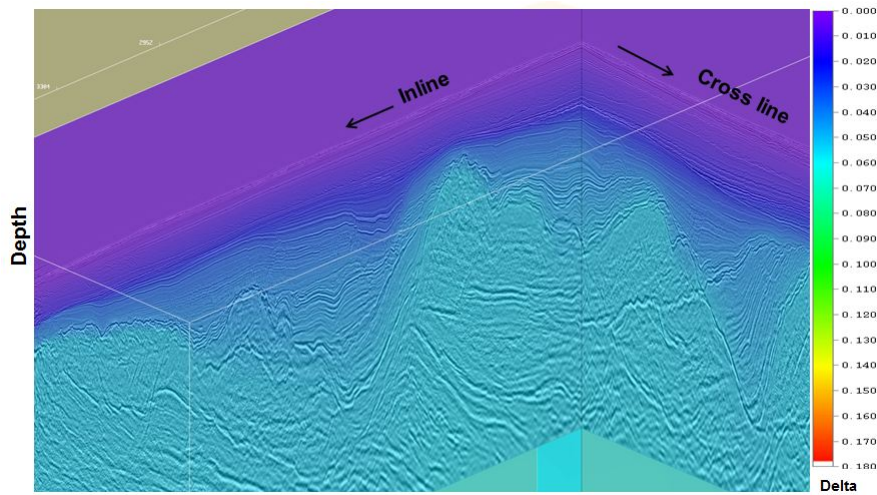


Figure 3.4: TTI $\delta$ model. The $\delta$ model is superimposed on the stack, which shows the delta model is consistent with compaction-driven sediments between the major horizons. The color represent different values of $\delta$ from 0 in purple to 0.18 in red.
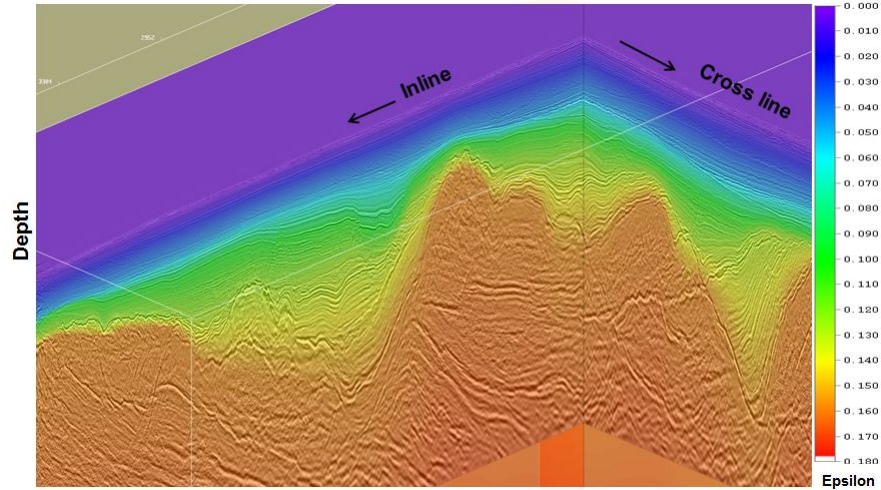
Figure 3.5: TTI $\epsilon$ model. The $\epsilon$ model is superimposed on the stack, which shows the epsilon model is consistent with compaction-driven sediments between the major horizons. The color represent different values of $\epsilon$ from 0 in purple to 0.18 in red.

shows the migration CIGs with $\epsilon / \delta = 2$, Figure 3.6b with $\epsilon / \delta = 2.5$, Figure 3.6c with $\epsilon / \delta = 3$. Based on the tests and the two wells at a nearby survey (100km away), the ratio of $\epsilon$ to $\delta$ was set to 2.5 to 1. Although ambiguity exists between $V_{p0}$ and $\delta$, the set of CIGs with the ratio of $\delta$ to $\epsilon$ as 1 to 2.5 shows the best event continuity and focusing. These figures also show that the migrated reflectors are positioned at different depths, with differences on the order of 10 meters. Given that the vertical position differences between isotropic and anisotropic images are approximately 200 meters, this difference is negligible.

### 3.2.3 Build an initial anisotropic bedding-normal velocity field

The result of our 1D inversion for $\delta$, in combination with our previously obtained isotropic velocity $v_{iso}$ and the expression ( Thomsen, 1986)

$$v_{(p0)} = \frac{v_{iso}}{\sqrt{1 + 2\delta}}. \tag{3.2}$$
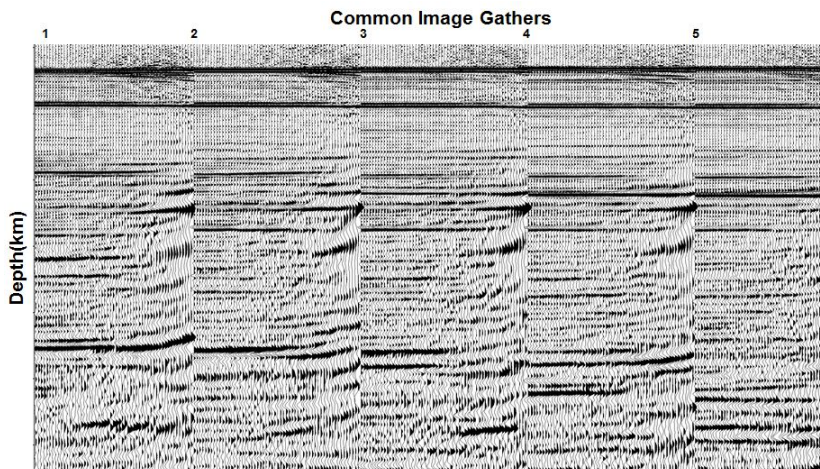
(a) CIGs generated from migration with ratio of $\delta$ to $\epsilon$ as 1 to 2
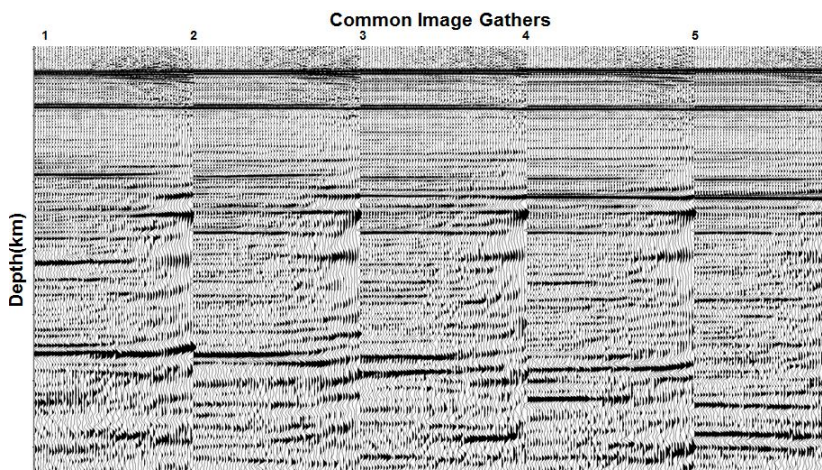


(b) CIGs generated from migration with ratio of $\delta$ to $\epsilon$ as 1 to 2.5
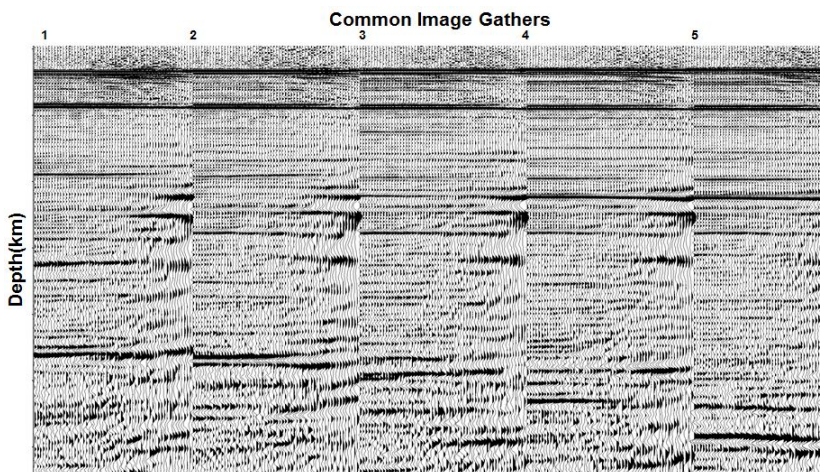


(c) CIGs generated from migration with ratio of $\delta$ to $\epsilon$ as 1 to 3

Figure 3.6: Testing on the ratio of $\epsilon$ to $\delta$

yields the bedding normal velocity model shown in Figure 3.7. In this picture, we see again the velocity superimposed on top of stack which shows velocity being conformable with geology structure. The velocity ranges from water velocity 1500 m/s in purple to 5300 m/s in yellow.
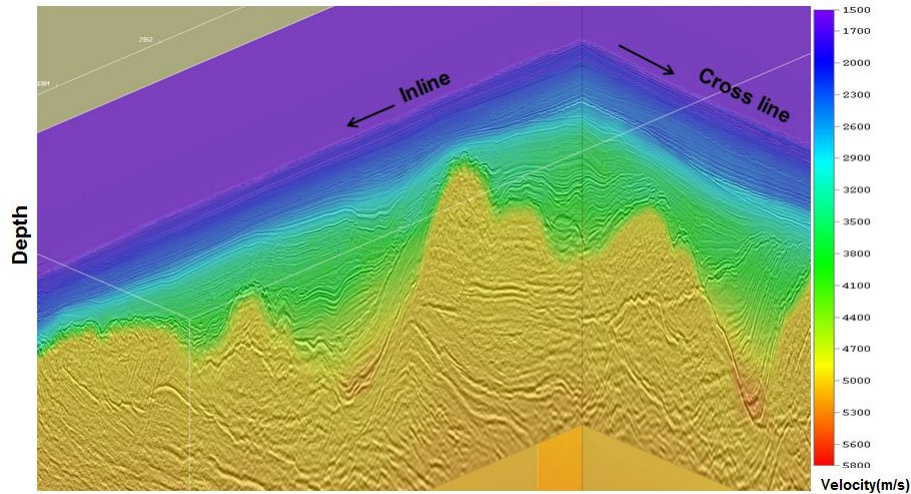


Figure 3.7: TTI bedding normal velocity is the velocity along the symmetric axis. TTI bedding normal velocity model superimposed on the stack which shows velocity being conformable with geology structure. The velocity ranges from water velocity 1500 m/s in purple to 5300 m/s in yellow.

Building $\theta$ and $\phi$

A TTI velocity model requires two axis of symmetry volumes to describe the tilt direction in 3D. These are dip $\theta$ and dip-azimuth $\phi$. The TTI symmetry axis was assumed to be perpendicular to the sedimentary bedding, so the axis is spatially variant with the structure changing from place to place. Any dipping event can be imagine as a vector in a 3D x-y-z coordinate system. $\phi$ is a clockwise rotation from the vector to the positive x-axis, and $\theta$ is an acute angle between the vector and xy plane. First, the dipx and dipy of dipping events were picked on migrated stack volume, then $\theta$ and $\phi$ were calculated

based on the dipping angle along x and y direction.

Audebert, et al. (2006) showed that a tilt model estimated from an isotropic migration is usually a sufficient approximation of the true tilt model. For such structurally conforming TTI ("Structurally conformable TI", or STI) media, the dip model can be determined by means of isotropic or VTI migration, assuming elliptic anisotropy (Audebert, et al., 2006). This often produces an adequate solution to the chicken and egg conundrum of estimating a tilt model for an STI medium.

We therefore picked $\theta$ and $\phi$ on isotropically migrated images, then ran TTI PSDM together with $\epsilon$ and $\delta$ models, and updated $\theta$ and $\phi$ as the velocity model evolved after each iteration.

Figures 3.8 and 3.9 show the $\theta$ and $\phi$ fields calculated from migrated data using this procedure. $\theta$ has values from 0 to 1.57 in radian (0-90 degree). Blue colur in Figure 3.8 indicates flat structure, while red color represents steep dip structure. $\phi$ has values from 0 to 6.28 in radian (0-360 degree). Figure 3.8 indicates relative steep dip in green and red, and flat reflectors in blue. The blue color in Figure 3.9 shows 0 degree azimuth. while purple color shows 360 degree azimuth.

### 3.2.4 Velocity update using high resolution tomography

After the initial TTI PSDM velocity field was built, we applied TTI high resolution global tomography (Hu, 2011). This technology plays an important role in the velocity model building flow for producing an optimal combination of subsurface image quality and geologically plausible velocity model.

We performed global tomography to improve and add detail to the initial bedding normal velocity model. Global tomography has many different versions. We used a version known as residual curvature analysis (RCA) tomography (Zhou et al., 2003). This is a grid based reflection tomography that operates on CIGs (Stork and Clayton, 1997).
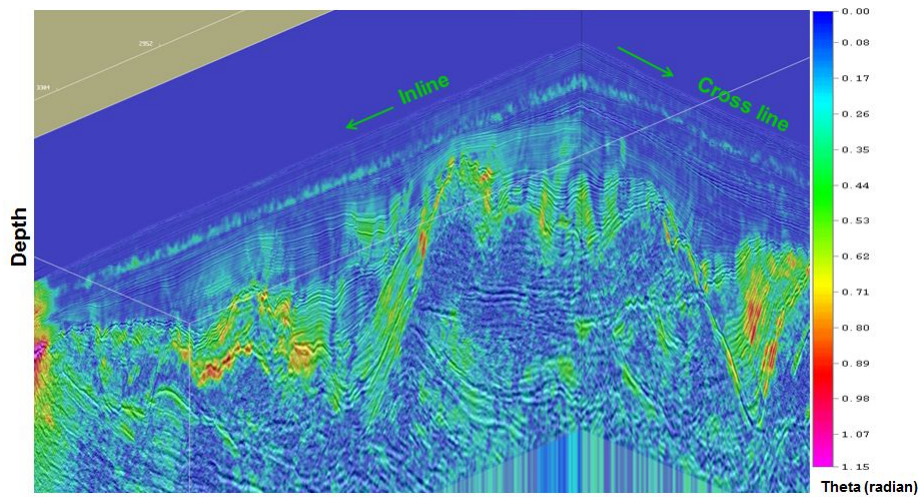
Figure 3.8: TTI $\theta$ model. $\theta$ is the dipping angle of the axis of symmetry. TTI $\theta$ model was overlaid on the stack image. Blue color indicates flat structure, while red color represents steep dip structure. The $\theta$ values follow the geology well.
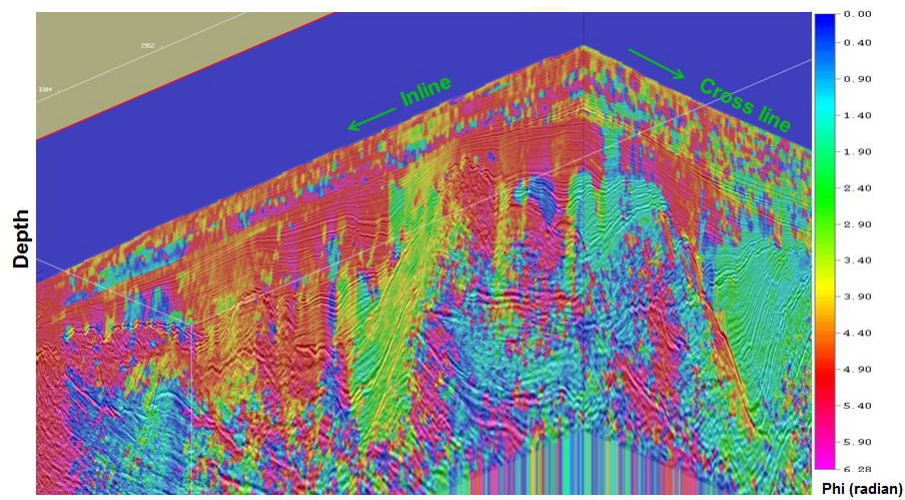


Figure 3.9: TTI $\phi$ model. $\phi$ is the azimuthal angle of the axis of symmetry. TTI $\phi$ model was overlaid on the stack image. Theta values range from 0 to 360 degrees illustrated by blue to purple.

The input to global tomography is residual curvatures (i.e., departures from flatness) picked from common image gathers (CIGs) of the full volume TTI PSDM. Tomography analyzes the residual curvatures and structural dip values, and globally determines the velocity perturbations to be assigned along ray paths through the existing model, so as to reduce the curvatures, making the CIGs flatter when the next migration iteration is performed. It accomplishes this by setting up and solving a large inverse problem. Typically, several iterations are needed before the best focusing and optimal subsurface images was achieved.

There are several factors affecting the resolution of the tomographic inversion. Among them, high-quality event picking is essential for stable and convergent velocity inversion. We achieve the best velocity updates by performing high resolution tomography, which features high-quality dense event picking, fine grid inversion and mild model smoothing.

The following three aspects highlight the difference between conventional tomography and high resolution tomography. First, the density of the event picking in x, y and z directions is finer in high-resolution tomography. In our present production work, the CIG grid used for picking is 75m x 75m, compared with a grid of 225m x 225m used until recently in the conventional tomographic work flow, resulting in a nine-fold increase in the number of CIGs used for event picking. Further, the minimum event separation along depth direction is reduced to 10m from 200m. The denser event picking in all three dimensions (x, y, and z) dramatically increases the number of picks, and thus the size of the matrix in the tomographic inversion. The more high-quality events are picked, the more consistent conditions can be applied to solve the linear system of equations (Zhou et al., 2003). Second, the high-resolution inversion grid is finer than in conventional tomography; in our case, the inversion grid is set to be the same as the velocity grid, i.e. 50m x 50m x 25m. Third, the velocity smoothing size in the tomography is reduced from several wavelengths to a very few wavelengths at dominant frequency, in order to

achieve high resolution in the updated model. This is enabled by the increase in pick density; otherwise the finer smoothing will cause an unstable inversion. Overall, the high resolution tomography scheme features velocity updates at a fine scale which cannot be achieved in a conventional tomography. Our increased computer power make high resolution tomography possible, with more CPUs and bigger memory size provided on each CPU.

We pick residual curvatures on CIGs, so data preconditioning also has a large impact on improving quality of picks. We applied several processing steps on CIGs before starting to pick the residual curvatures. This includes: signal enhancement to improve the signal to noise ratio; high resolution radon demultiple to remove residual multiples; and open mute to eliminate far offset "junk" (usually refraction, not reflection, data).

In addition, we apply several picking criteria such as reflector coherency, average semblance and amplitude level of CIGs to ensure that only reliable events were picked (Liu and Han, 2010).

Compared with isotropic global tomography, TTI global tomography has two extra parameters in ray tracing: $\epsilon$ and $\delta$. Recognizing the trade-off between the bedding normal velocity and anisotropy parameters (Tsvankin and Thomsen, 1995), we hold $\delta$ and $\epsilon$ unchanged in the inversion, and invert only for bedding normal velocity. This also eliminates the possibility of an under-determined inversion, where the number of unknowns exceeds the number of observations.

We performed four iterations of global tomography. Although each application was of global tomography, we proceeded in a roughly top-down fashion. The first iteration targeted the thin layer right beneath the water bottom, which is critical for getting the velocity right for the deep section. The second iteration was run from water bottom to 6 km in depth. The key horizon, base tertiary, has its greatest depth at around 6km. The third iteration was performed from water bottom to basement. A strong velocity

contrast is observed right beneath the basement; We performed velocity scans to obtain the correct velocity beneath this layer. Our fourth RCA update was used to solve any residual velocity error from top to bottom.

Immediately beneath the water bottom there is a high-velocity layer which is about 50m thick. For thin layers with large velocity contrasts, conventional global tomography has very poor resolving power. As shown next, the dense picking grid, small event separation, fine ray tracing grid, small smoothing, and fine velocity grid of high resolution tomography allowed us to solve the thin-layer problem in this case. (Of course, even high-resolution tomography has resolution limits imposed by its parameters.)

Figure 3.10 shows CIGs extracted from the shallow zone. The two events indicated in the circled area in Figure 3.10a reveal a conflict: the top event curves down, indicating that a slower velocity is needed; while the bottom event curves up, indicating that a faster velocity is needed. The separation between these two events is less than 50m. This is a common dilemma seen in velocity model updating. By using conventional tomography, correcting one event often leads to a degradation of the other. With high-resolution tomography, the velocity update is more localized and flexible and can catch this rapid bedding normal velocity change. Figure 3.10b shows CIGs migrated with the velocity obtained by high resolution tomography. CIGs from both events are flatter and better focused, indicating a more accurate velocity model has been obtained. The velocity fields the migration used to generate the CIGs are shown on Figure 3.11. Figure 3.11a shows the initial velocity overlay on seismic sections, and Figure 3.11b shows the updated velocity field after high resolution tomography. The color bar represents the velocity value from slower velocity in blue, to faster velocity in red. We can see that the velocity shown in Figure 3.11a has a very smooth trend and has little detail compared with the structure underneath. It is evident that high resolution tomography has captured the localized high velocity layer very well as shown in Figure 3.11a. For example, the speed-up velocity in

yellow makes the CIGs flat in the circled area shown in Figure 3.10

A second example is from a structured area in the deeper section. I show the gathers in Figure 3.12 and velocity models overlay on the migrated stacks in Figure 3.13. The CIGs shown in Figure 3.12a show gathers curved down in circled area, indicating the velocity is too low. This is due to a bedding normal velocity update performed before tomography. As mentioned earlier, vertical updating can produce smooth velocity models but cannot accurately estimate strong lateral velocity variation, while the gathers after the high resolution tomography are flatter as shown in Figure 3.12b. Figure 3.13 shows a comparison of a Kirchhoff full stacked image, using the initial velocity model (Figure 3.13a) and the high resolution tomography-updated velocity (Figure 3.13b). Figure 3.13b shows that the updated velocity model conforms with the structure very well, and images are much better focused.

### 3.2.5   Verify $\epsilon$ and $\delta$

After bedding normal velocity updating followed by global tomography, we held the bedding normal velocity unchanged, and tried to update $\epsilon$ and $\delta$ by scanning using a range of different values. We observed very subtle difference among the scans, but not enough to justify changing the values obtained earlier.

### 3.2.6   Velocity scans below the basement

Just below the basement is a high velocity layer where vertical updating and global tomography cannot work well because of insufficient move-out differences at the far offsets. To estimate velocity based on geologic plausibility of the images, we conducted velocity scans for the deeper section beneath the basement.

Starting from the reference velocity model, we generated a set of velocity functions by perturbing the reference velocity model from 90 percent to 120 percent with an increment
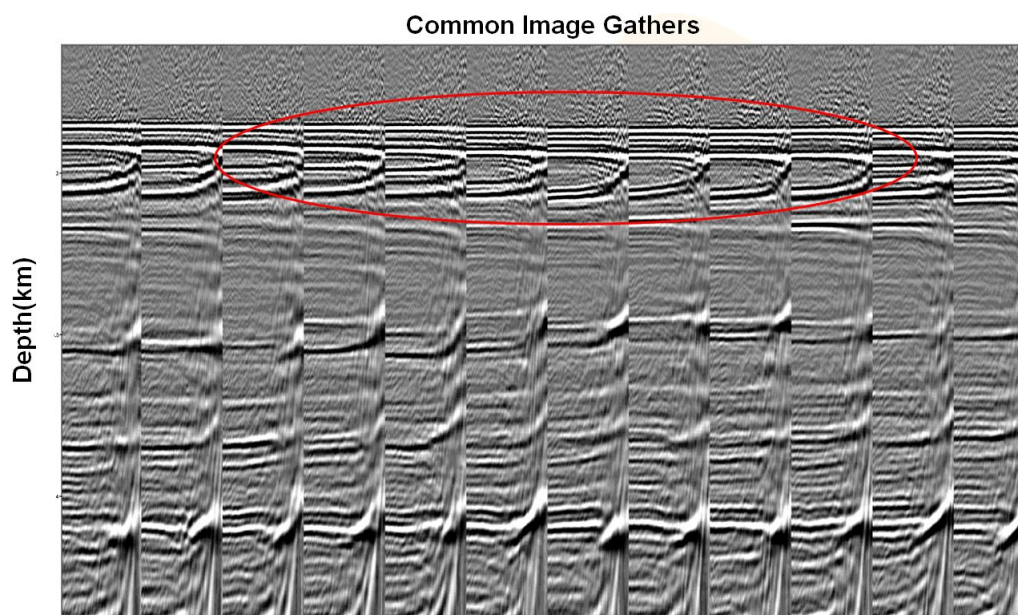
(a) CIGs after initial TTI PSDM.
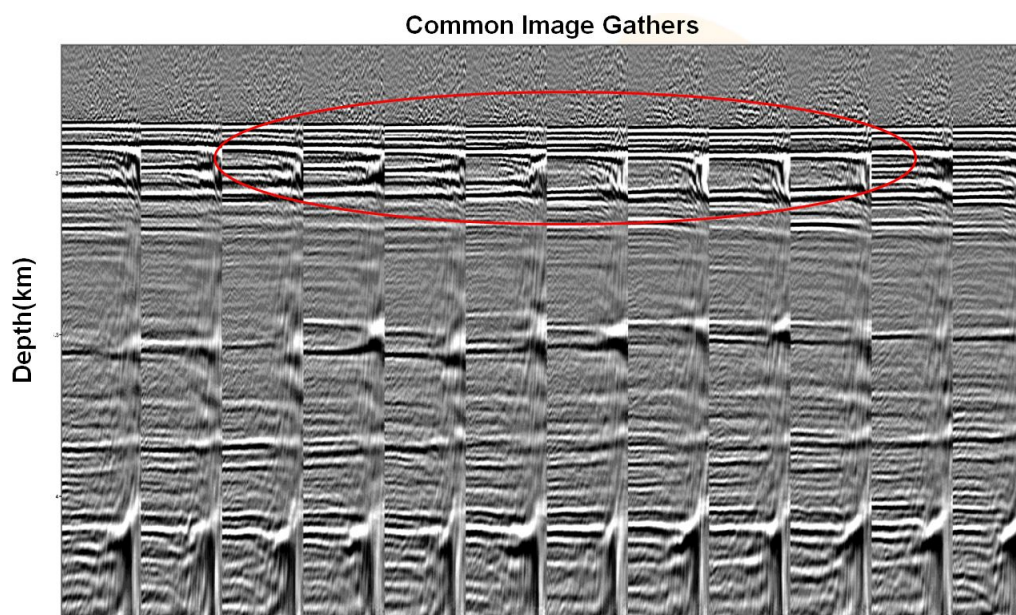


(b) CIGs after TTI global tomography.

Figure 3.10: CIG gathers before and after TTI Tomography. The two events in circled area in (a) reveal a conflict. The top event needs a slower velocity and the bottom event needs a faster velocity. The separation of these two events is less than 50m. Figure (b) shows that high resolution tomography caught this rapid bedding normal velocity change. Both top and bottom events are flattened.
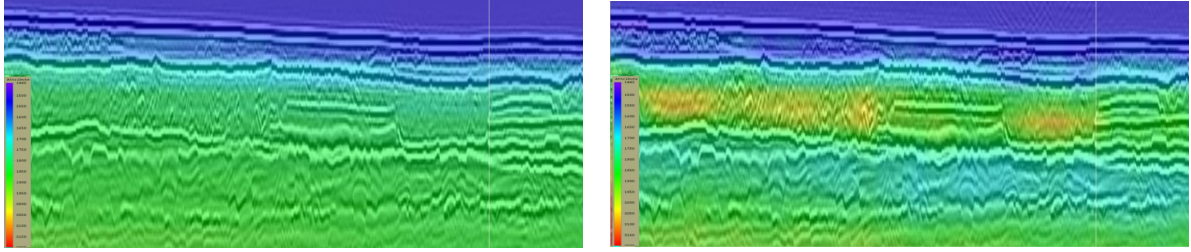
(a) Velocity model before global Tomography     (b) Velocity model after global Tomography

Figure 3.11: Velocity represented by the different color superimposed on the stack. Velocity values range from slow in blue to fast in red. (a) shows very smooth velocity trend and has no detail corresponding the structure underneath, while the velocity in (b) captures the localized speed-up velocity shown in yellow.

of 5 percent. We based our velocity update on the variation in the focusing of the migrated image, caused by the introduction of velocity perturbations.

Velocity beneath basement varies very slightly because velocity field is mainly compaction driven. Velocity scans help us get a good trend of velocity in the deep section, and make the structure simplified and continuous. Figure 3.14 shows the image comparisons before and after velocity scans, showing dramatic improvement on structure definition.

## 3.3  Results and discussion

This chapter presented a practical work flow for building TTI velocity models for PSDM. TTI PSDM needs five velocity fields including the bedding normal velocity in the "slow" direction, Thomsen parameters $\delta$ and $\varepsilon$, the angles describing the symmetry axis of the anisotropy, $\theta$ and $\phi$. We started with an isotropic bedding normal velocity, estimated $\delta$ and $\varepsilon$ using 1D joint inversion in the mini-basin areas, picked $\theta$ and $\phi$ on the migrated volume, and then calculated an initial anisotropic "slow" bedding normal velocity. Finally, we updated velocity using high resolution tomography analysis and
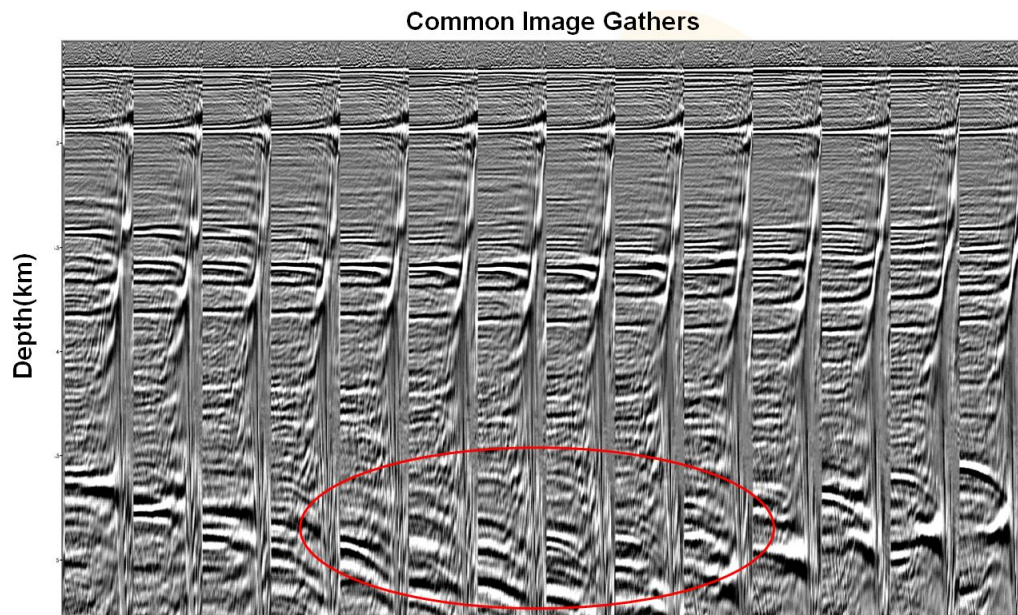
(a) CIGs after initial TTI PSDM
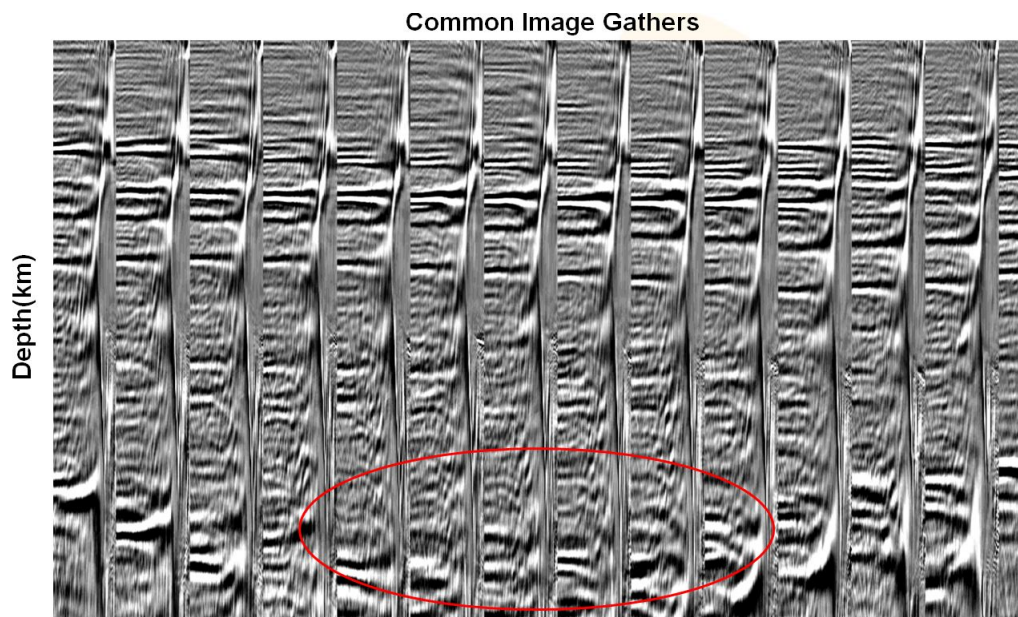


(b) CIGs after TTI global tomography

Figure 3.12: CIGs before and after tomography. The events in circled area in (a) curves down, while in (b), the events are flattened
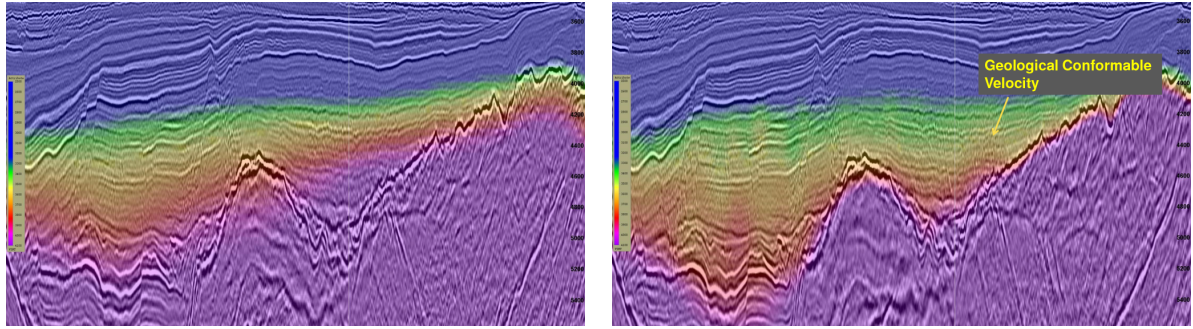
(a) Velocity model before tomography  (b) Velocity model after tomography

Figure 3.13: Velocity model before and after tomography. The velocity superimposed on the stack. The velocity in (a) does not follow the geology; the velocity in (b) conforms with the structure well.

velocity scans in the deeper section.

Figure 3.16 shows an image comparison between isotropic PSDM and TTI PSDM. We observe that the subsurface image from TTI PSDM is the sharper and better focused of the two. Most likely, TTI PSDM has moved the subsurface events to more correct vertical and lateral positions. For this project, TTI images are shallower by 90m to 200m across the entire survey. Comparing the CIGs in Figure 3.15a and Figure 3.15b, the AVO response from anisotropic gathers shows more believable amplitude variation versus offset as well as more information at far offsets. We can see broken events and amplitude dimming at far offset from isotropic gathers and residual hockey sticks, which only the incorporation of TTI in the PSDM can resolve.

We can draw two major conclusions from this case study.

1. Compared with isotropic PSDM, TTI PSDM provides more likely correct lateral and vertical position for subsurface structures, and more reliable CIGs for further AVO analysis. This is because TTI PSDM has resolved move-out discrepancies in the migrated CIGs better than isotropic PSDM has. Correct structural positioning
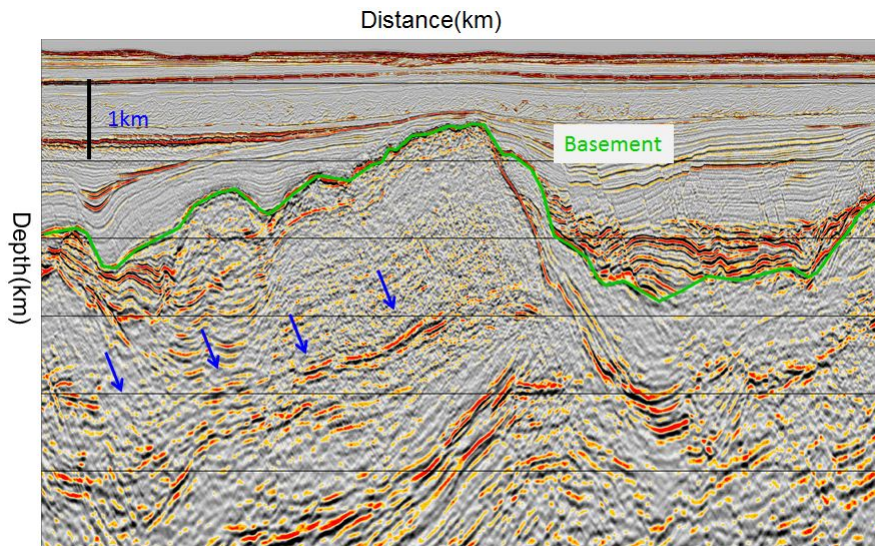
(a) PSDM images before velocity scan
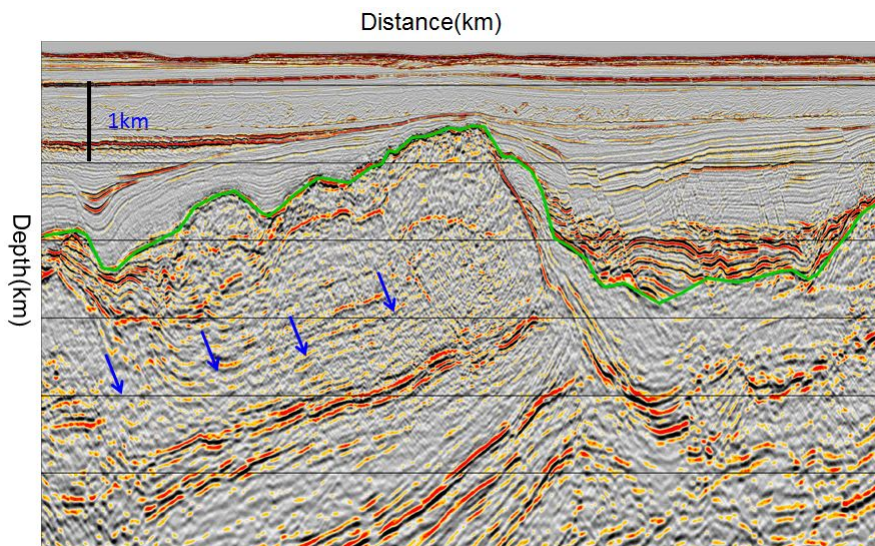


(b) PSDM Images after velocity scan

Figure 3.14: Stack comparison before and after velocity scan.

and more reliable migrated amplitudes from TTI PSDM both reduce exploration risk compared with alternative methods, such as PSTM or isotropic PSDM.

2. High resolution global tomography helps update the velocity in areas of sharp and fine-scale velocity contrast, and can produce geologically plausible velocity models more easily than conventional tomography can. In this case, high-resolution tomography has produced a less ambiguous velocity model than conventional tomography, also leading to a reduction of exploration risk.
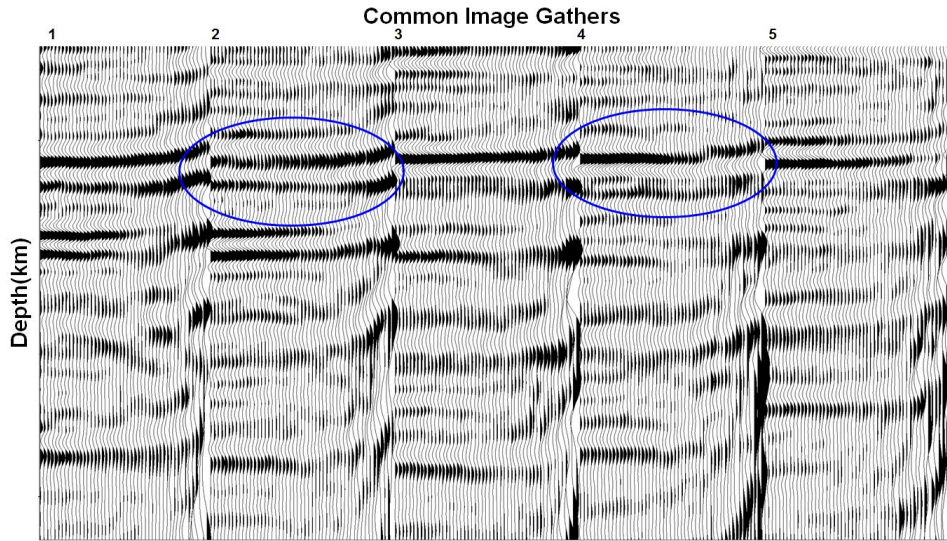
(a) CIG gathers after isotropic PSDM processing
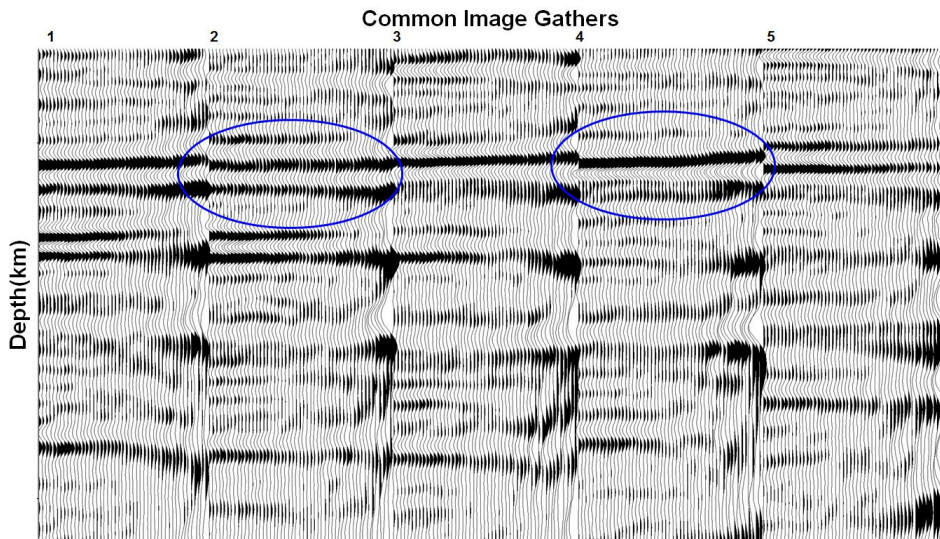


(b) CIG gathers after TTI anisotropic PSDM

Figure 3.15: Gather comparison between isotropic and anisotropic PSDM processing. Gathers from isotropic PSDM in (a) shows the event broken and amplitude dimming at far offset. Gathers from anisotropic PSDM in (b) shows more continuous and more believable amplitude variation versus offset as well as more information at far offsets.
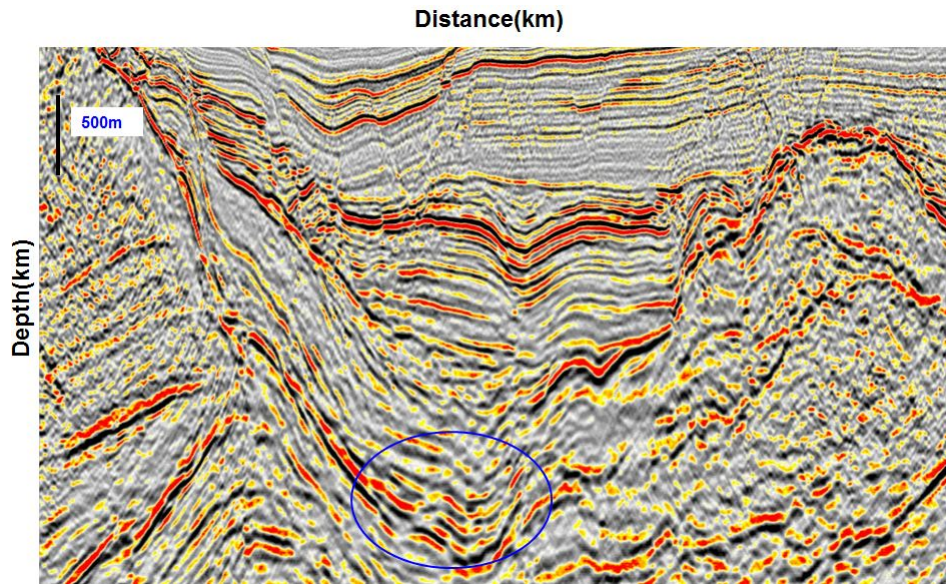
(a) PSDM image after isotropic PSDM processing
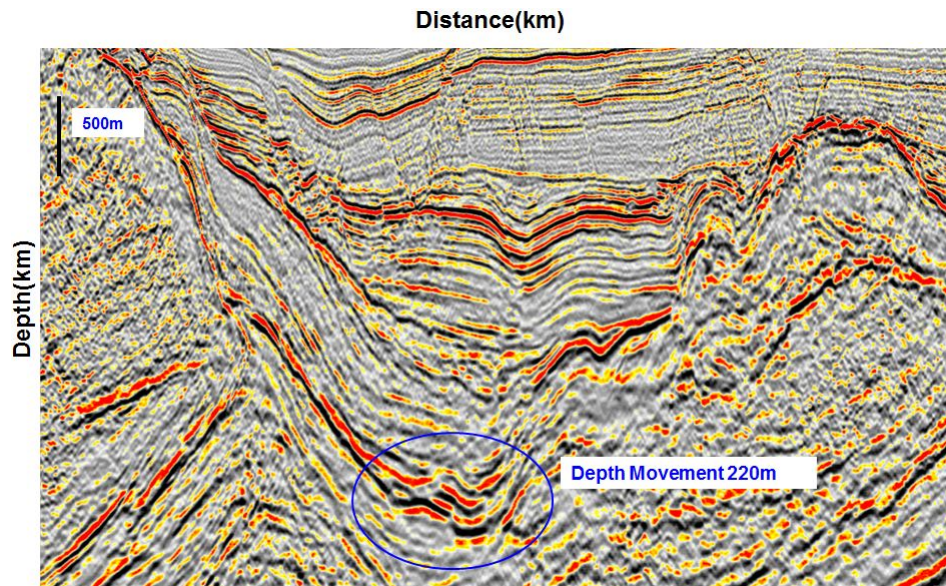


(b) PSDM image after TTI anisotropic processing

Figure 3.16: Image comparison between isotropic and anisotropic PSDM processing. The migration image from anisotropy PSDM processing are more sharper and continuous, provide more likely correct and vertical position for subsurface structures.

# Chapter 4

# Conclusions and future work

## 4.1  Conclusions

1. To achieve the goal of accurately positioning the seismic events in subsurface, the velocity anisotropy should be accounted for. The presence of anisotropy causes two principal distortions in reflection moveout. First, inaccurate vertical velocity will cause inaccurate estimations of reflector depths. Second, anisotropy leads to nonhyperbolic moveout, even in a homogeneous layer. If not properly corrected for, nonhyperbolic moveout causes distortions in velocity estimation and deteriorates the image quality. The case study in this thesis demonstrates that TTI PSDM provides better focusing and more continuous subsurface images and more reliable CIGs compared with isotropic PSDM, and results in more likely correct lateral and vertical positions for subsurface structures.

2. A good velocity model is the key to the success of pre-stack depth migration. A good velocity model of the anisotropy parameters and the P wave vertical velocity should make CIGs flat, produce better focused subsurface images and be geologically plausible. This thesis demonstrates how different velocity models will affect gather flatness and image quality by showing the real data examples.

3. Estimation of reliable anisotropy parameters is challenging, especially for surveys where no well information is available. This thesis showed the effectiveness of using 1D joint inversion (Huang, 2007) to estimate anisotropy parameters $\varepsilon$, $\delta$.

4. High resolution global tomography helps update the velocity in areas of sharp and

fine-scale velocity contrast, and can produce geologically plausible velocity models more easily than conventional tomography. In this case, high-resolution tomography has produced a less ambiguous velocity model than conventional tomography, also leading to a reduction of exploration risk.

## 4.2   Original contributions

1. This thesis presents a practical production work flow for building five parameter fields needed for TTI PSDM: p-wave velocity, Thomsen's anisotropy parameters and the angles describing the symmetry axis of the anisotropy. This method includes 1D joint inversion (Huang, 2007) to initially estimate anisotropy parameters and high resolution tomography (Hu, 2011) to obtain accurate velocity models. Unlike Huang's case in his paper, the data studied in this thesis has no well information available. The bedding normal velocity has to be estimated in the area with no steep dip structure; this bring more difficulties and result in more testing for inverting Thomsen parameters.

2. This thesis documents a complex imaging task that uses leading edge software and concepts.

   The work conducted in this thesis comes from a frontier exploration seismic survey acquired off the East Coast of Canada by Statoil Canada Limited. The main objectives of seismic processing are to provide good structural positioning and imaging focusing particularly on the complex faulting, and at the same time preserve amplitude. The survey covers an area of approximately $1700km^2$. The seismic processing of this 3D survey was performed at CGG Calgary processing center from September 2011 to March 2012. Both isotropic pre-stack depth migration (PSDM) and tilted transverse isotropic (TTI ) PSDM were conducted. The objective for this

project is to provide good structural positioning and imaging, so deriving a good velocity model is very critical for the success of this project. I am the key person for velocity model building which were described in chapter 3 in this thesis; I am also supervising and doing quality control of preprocessing part which prepare the input for velocity model building. CGG processing systems are PC cluster based. Intel 64-bit Nehalem PC Linux clusters with total 1516 CPU cores were used for this project. Many single CPU processing PCs were available for preprocessing. One processing step for this project required a diskspace of 8000 gigabytes; to keep the project running smoothly, total diskspace used was more than 80000 gigabytes.

This thesis documents the detailed history and practices of anisotropic depth imaging. Many research papers on different specific topics are in different places and published at different times. This thesis put the valuable insights in one place and provides a strong statement about the present state-of-the-art. The main techniques used in both pre-processing and migration velocity analysis were presented in detail, both in theory and the application in real production.

3. I presented the notion that seismic processing is an art as well as science. Different surveys will present different problems in seismic processing, and different processors will use different tricks to deal with the problems. The seismic processing involved a lot of careful parametrization. For example, we used a hybrid tomography to pick up the high velocity contrast right beneath the water bottom. To catch the high velocity contrast beneath the basement, we designed the synthetic wells to control the velocity trend based on the velocity values after velocity scan.

## 4.3 Future work

1. The data studied in this thesis is conventional narrow azimuth data. It would be very beneficial if a wide azimuth "broadseis" (broadband) survey can be acquired for future processing in this area. Wide azimuth data can give better illumination from different directions for complex structures and the broadseis data can provide broadband frequency, both in low and high frequencies.

2. The client is going to drill wells on this survey in the very near future. We will check how accurate the lateral and vertical position provided by our processing images are; based on this, further research can be conducted and processing job flow can be adjusted.

3. For all the frontier projects, there are typically no wells available at the beginning of the exploration stage, so we will always encounter the dilemma on how to correctly estimate the vertical velocity and anisotropy parameters $\delta$ and $\varepsilon$ at the same time without any wells available. A good research project can be conducted on optimizing the processing parameters to minimize the depth errors on final migrated images. We can quantify how different processing parameters will affect velocity parameters, and in turn how much depth errors will be on final images. We start with calculating theoretical synthetic data with an assumed vertical velocity, $\delta$ and $\varepsilon$, we can design the following test using a synthetic data set:

   (a) Run isotropic PSDM, quantify how much depth error will be caused by isotropic PSDM.

   (b) Find out what is the best offset range for estimating the vertical velocity. The near to middle offsets will be used to estimate the vertical velocity. Normally a 45 degree angle (incidence angle) mute is applied to get rid of the data at

the far offsets. Different angle mutes should be tested. Different strategies for designing the mute could be tested, for example, mute can be placed at the point where the amplitude increases, or at the turning point of non hyperbolic moveout. This test can help find out what is the optimal mute and quantify how much depth error will be caused by applying different mutes.

(c) Find out what is the best offset range for inverting $\delta$. It is known that $\delta$ should be estimated over short offsets and $\varepsilon$ should be estimated over long offsets. We can start with ideal vertical velocity, then invert the $\delta$ over different near offset, this test can help find out what is the optimal range of offsets to use for inverting $\delta$.

(d) Find out what is the best offset range for inverting $\varepsilon$. We can test to invert only $\varepsilon$ by letting the actual vertical velocity and $\delta$ together take good care of near to middle offsets moveout. After we get the $\varepsilon$ value, we can assume a certain relationship to determine $\delta$, and recalculate the vertical velocity. This test can help quantify how much depth error will be caused by this kind of approximation.

(e) Find out how to make the inversion of anisotropy parameters stable and faster. Normally industry will use some kind of ratio of $\varepsilon$ to $\delta$ to help stabilize and speed up the convergence of final inversion results. But the ratio of $\varepsilon$ to $\delta$ is always empirical. We can design one synthetic model to have fixed $\varepsilon$ to $\delta$ relationship, and an other model which has no fixed relationship to start with. There will be some errors on inverted $\varepsilon$ and $\delta$ if the starting model has no fixed relationship between $\delta$ and $\varepsilon$; however, we can quantify how much depth error will be caused by this approximation, and whether they are within the acceptable bounds.

# Bibliography

[1] Abma, R., Sun, J. and Bernitsas, N., 1999, *Antialiasing methods in Kirchhoff migration*: Geophysics, 64, 1783-1792.

[2] Alkhalifah, T, and Larner, K., 1994, *Migration errors in transversely isotropic media*: Geophysics, 59, 1405-1418.

[3] Alkhalifah, T, and Tsvankin, I., 1995, *velocity analysis for transversely isotropic media*: Geophysics, 60, 1550-1566.

[4] Alkhalifah, T, 1997, *velocity analysis using nonhyperbolic move-out in transversely isotropic media*, Geophysics, 62,P.1839-1854.

[5] Al-Yahya. k., 1987, *velocity analysis by iterative profile migration*: Ph.D. thesis, Standford Univ.

[6] Audebert F., Dirks V., Pettenati A., 2006 *TTI anisotropic depth migration: what tilt estimate should we use?*: SEG Technical Program Expanded Abstracts 2006: 2382-2386.

[7] Bancroft, J., C., 1996, *Natural Anti-aliasing in equivalent offset prestack migration*, SEG Technical Program Expanded Abstracts, 1996.

[8] Bancroft, J., C., 2001, *Prestack considerations for the migration of oblique reflectors*, CREWES Project - University of Calgary.

[9] Bednar, J., Bee, 2005, *A brief history of seismic migration*, 2005, Panorama Technologies.

[10] Biersteker, J., 2001, *MAGIC: shell's surface multiple attenuation technique*, 71st internat. Mtg., Soc, Expl. Geophys., Expanded Abstracts, 1301-1304.

[11] Bleistein, N., Cohen, J. K., and Stockwell, J. W., 1998, *Mathematics of multidimensional seismic inversion*, Lecture Notes, Summer School in Mathematical Geophysics, Stanford University.

[12] Bleistein, N., 1999, *Hagedoorn told us how to do Kirchhoff migration and inversion*, The Leading Edge, August 1999. Vol. 18, No. 8, pp. 918-927.

[13] Bleistein, N., Cohen, J.K., and Stockwell, J. W., 1998, *Mathematics of multidimensional seismic inversion:, Lecture Notes*, Summer School in Mathematical Geophysics, Stanford University.

[14] Bleistein, N., and Gray, S. H., 2001, *From the hagedoorn imaging technique to Kirchhoff migration adn inversion*, Geophys. Prosp., 49, no. 06, 629-643.

[15] Biondi, Biondo L., *Concepts and Applications in 3D Seismic Imaging*, Tulsa: Society of Exploration Geophysics, 2007.

[16] Byun, B. S., 1982, *Seismic parameters for media with elliptical velocity dependencies*, Geophysics, 47, 1621-1626.

[17] Castle, R. J., 1994, *A theory of normal move-out*: Geophysics, 59, 983-999.

[18] Claerbout, J. F., 1970, *Coarse grid calculations of waves in inhomogeneous media with application to delineation of complicated seismic structure*, Geophysics, 35, no. 03, 407-418.

[19] Claerbout, J. F., 1971, *Toward a unified theory of reflector mapping*, Geophysics, 36, no. 03, 467-481.

[20] Claerbout, J. F., 1985, *Imaging the earth's interiour* Blackwell Scientific Publications, Inc.

[21] Dellinger, J., Gray, S. H., Murphy, G. E., and Etgen, J. T., 2000, *Ecient two and one-half dimensional true- amplitude migration*: Geophysics, 63.

[22] Deregowski, S. M., 1990, *Common-offset migrations and velocity analysis*: First Break, 8, 224-234.

[23] Dix, C. H., 1955, *Seismic velocities from surface measurements*: Geophysics, 20, 68-86.

[24] Egozi, U., 1999, *Efficient Development of velocity Models over Gulf of Mexico Salt Structures*, Tulsa: Society of Exploration Geophysics, 1999.

[25] Evans, B. J., 1997*A handbook for seismic data acquisition in exploration*, SEG, geophysical monograph series.

[26] Fagin, S., *Model-Based Depth Imaging*, Tulsa: Society of Exploration Geophysics, 1999.

[27] Faye. J. P., and Jeannot, J. P., 1986, *pre-stack migration velocities from focusing depth analysis*, 56th Ann. INternat. Mtg., Soc. Expl. Geophys., Expanded Abstracts, 438-440.

[28] Gardner, G. H. F., W. S. French, and T. Matzuk, 1974, *Elements of migration and velocity analysis*: Geophysics, 39, 811-825.

[29] Gassmann, F., 1951, *Elastic waves through a packing of spheres*, Geophysics OCt 1951, Vol.16, No. 4, pp 673-685.

[30] Gray, S.H, 2001, *Seismic Imaging*, Geophysics, vol 66.

[31] Gray, S.H, 2009, *An overview of depth imaging in exploration geophysics*, Geophysics, 74, WCA5-WCA17.

[32] Gray, S., 1998, *veloicty smoothing for depth migration: how much is too much*, Geophysics, 63, 1200-1209.

[33] Grechka, V., Pech, A.,Tsvankin, I., and Han, B., 2001, *Velocity analysis for tilted transversely isotropic media: A physical modelling example*, Geophysics, 66, 904-910.

[34] Grechka, V., Pech, A., and Tsvankin, I., 2002, *Multicomponent stacking-velocity tomography for transversely isotropic media*, Geophysics, 67, 1564-1574.

[35] Grechka, V., Theophanis, S., and Tsvankin, I., 1999, *Joint inversion of P- and PS-waves in orthorhombic media*, Geophysics, vol 64, 146-161.

[36] Guo, J, Zhou, H, Young, J and Gary SL., 2002, *Merits and challenges for accurate velocity model building*, SEG Int'l Expostition and 72nd Annual Meeting.

[37] Hagedoorn, J. G., 1954, *A process of seismic reflection interpretation*, Geophysical Prospecting, 06, 449-453.

[38] Hanitzsch, C., 1997, *Comparison of weights in prestack amplitude-preserving Kirchho depth migration*, Geophysics, 62, no. 6, 1812-1816.

[39] Hargreaves, N., Cooper, N., 2001, *High - resolution radon demultiple*, SEG Technical Program Expanded Abstracts, 2001:1325-1328.

[40] Huang, T., Xu, S., Zhang, Y., 2007, *Anisotropy Estimation for Prestack Depth Imaging*, SEG Technical Program Expanded Abstracts 2007, 124-128.

[41] Hu, L., Zhou, J., 2011, *Velocity Update Using High Resolution Tomography in Santos Basin, Brazil*, SEG Technical Program Expanded Abstract, 3974-3978.

[42] Hake, H., Helbig, K., and Mesdag, C. S., 1984, *Three-tenm Taylor series for $t^2$ - $x^2$ curves over layered transversely isotropic ground:*, Geophysics, Prosp., 32, 828-850

[43] Issac, J. H., and Lawton, D. C., 1999,*Image mispositioning due to dipping TI media: A physical seismic modeling study*, Geophysics, 64, 1230-1238.

[44] Issac, J. H., and Lawton, D. C., 2004,*A practical method for estimating effective parameters of anisotropy from reflection seismic data*, Geophysics, 69, No. 3, p. 681-689.

[45] Lawton, D. C., Issac, J. H., Vestrum, R. W., and Leslie, J. M., 2001, *Some practical implications of seismic velocity anisotropy on depth imaging*, The Leading Edge, 20, 70-73.

[46] Lin, D., Young, J., and Huang, Y., 2004, *3D SRME Application in the Gulf of Mexico*, ASEG 17th Geophysical Conference and Exhibition, Syney, Extended Abstracts.

[47] Line, L., Zhu, J. and Gray, S., 1998, *Smiles and Frowns in migration/velocity analysis*, Geophysics, 63, 1200-1209.

[48] Lines, L., 1993, *Ambiguity in analysis of velocity and depth*, Geophysics, 58, 596-597.

[49] Santos, L. T., Tygel M., 2004, *Impedance-type approximations of the P-P elastic reflection coefficient: Modeling and AVO inversion*, Geophysics, 69, 592-598..

[50] Lumley, D., Claerbout, J. and Bevc, D., 1994, *Antialiased Kirchhoff 3-D migration*, Annual Internat. Mtg., Soc. Expl. Geophys., Expanded Abstracts 1282-1285.

[51] Liu, J. and Han W., 2010 *Automatic event picking and tomography on 3D RTM angle gathers*, SEG Expanded Abstracts.

[52] Margrave, G., 2012, *Numerical Methods of Exploration Seismology.*

[53] M.M.N. Kabir and Dirk J. Verschuur, 1994 *Integrated velocity estimation and stacking using parabolic Radon transform*, Delft University of Technology, SEG Technical Program Expanded Abstracts.

[54] Nye. J. F., 1957, *Physical properties of crystals*: Oxford Press.

[55] O'Brien, M., and Gray, S., 1996, *Can we image beneath salt?*: The Leading Edge, 15, 17-22.

[56] Reddy, P. R., 2012,*Historical development of seismic imaging technique - An overview*: Geophysics, Union, vol.16.

[57] Rieber, F., 1936, *A new reflection system with controlled directional sensitivity*, Geophysics, 01, no. 01, 97-106.

[58] Sacchi, M. D., Ulrych, T. J., 1995, *High - resolution velocity gathers and offset space reconstruction*, Geophysics, 60, 4, 1169-1177.

[59] Schneider, W., A., 1978, *Integral Formulation fro migration in two and three dimensions*, Geophysics Feb 1978, Vol. 43, No. 1, pp. 49-76.

[60] Sheriff, R.E., Geldart, L. P., 1995, *Exploration Seismology (2nd ed.)*, Cambridge University Press, P.404-419.

[61] Stork, C. and Clayton, W., 1997, *Using constraints to address the instabilities of automated pre-stack velocity analysis*, Geophysics, 57, P.404-419.

[62] Soubaras, R., *Signal-preserving random noise attenuation by the f-x projection*, 64th Annual International meeting, SEG Expanded Abstrcts, 1576-1579.

[63] Taner, M. T., and F. Koehler, 1969, *velocity spectra – Digital computer derivation and applications of velocity functions*: Geophysics, 34, 859-881

[64] Thierry, P., Lambare, G., Xu, S., 1999 *3D common diffracting angle migration inversion for AVA analysis*, SEG Technical Program Expanded Abstracts 1999: 844-847.

[65] Thomsen, L., 2002, *Understanding Sesimic Anisotropy in Exploration and Exploitation*: Soc. Expl. Geophys.

[66] Thomsen, L., 1986, *Weak elastic anisotropy*, Geophysics, 51, 1954-1966.

[67] Tsvankin, I., 1995, *P-wave signatures and notation for transversely isotropic media: An overview*, Geophysics, 61, 467-483.

[68] Tsvankin, I., and Thomsen, L., 1994, *Nonhyperbolic reflection move-out in anisotropic media*, Geophysics, 59, 1290-1304.

[69] Tsvankin, I., 2000, *Seismic signatures and analysis of reflecion data in anisotropic media*, Pergammon Press.

[70] Versteeg, R., J., 1993, *Sensitivity of pre-stack depth migration to the velocity model*, Geophysics, 58, 8734382.

[71] Vestrum, R. W., Lawton, D. C., and Schmid, R., 1999, *Imaging strctures below dipping TI media* Geophysics, 64, 1239-1246.

[72] Wang, P. and Peng, C., 2012, *Premigration deghosting for marine towed streamer data using a bootstrap approach*, SEG Technical Program Expanded Abstracts 2012.

[73] Wang, Z., 2001, *Seismic anisotropy in sedimentary rocks*, SEG Technical Program Expanded Abstracts 2001: pp. 1740-1743.

[74] Wyllie, M. R. J., Gregory, A. R., Gardner, G. H. F., 1958 *An Experimental investigation of factors affecting elastic wave velocities in porous media*, Geophysics Jul 1958, Vol. 23, No. 3, pp. 459-493.

[75] Whitemore, N. D., and Garing. J. D., 1993 *Interval velocity estimation using iterative pre-stack depth migration in the constant angle domain*, The Leading Edge, 12, 757-762.

[76] Yilmaz, O., 2002, *Seismic Data Processing* Soc. Expl. Geophys, P81-93.

[77] Young, K. T. J., Notfors, C. D., Meng, X. G., and Montecchi, P., 1999, *Subsalt imaging in Walker Ridge, Gulf of Mexico*: 69th Ann. Internat. Mtg., Soc. Expl. Geophys., Expanded Abstracts.

[78] Zhang, Y., Gray, S., Sun, J. and Notfors C., 2001, *Theory of migration anti-aliasing*, Annual Internat. Mtg., Soc. Expl. Geophys.

[79] Zhang, Y., Gray, S., and Young, J., 2000, *Exact and approximate weights for Kirchhof migration*, SEG Technical Program Expanded Abstracts 2000, 1036-1039.

[80] Zhou, H., Gray, S., Young, J., Pham, D., and Zhang, Y., 2003, *Tomographic Residual Curvature Analysis: Process and Its component*, SEG Technical Program Expanded Abtracts 2003, 666-669.